Cross-comparison and uncertainty quantification of aeroacoustic measurements performed in several wind tunnels

Guillem Vergés i Plaza

European Wind Energy Master
Rotor Design - Aerodynamics

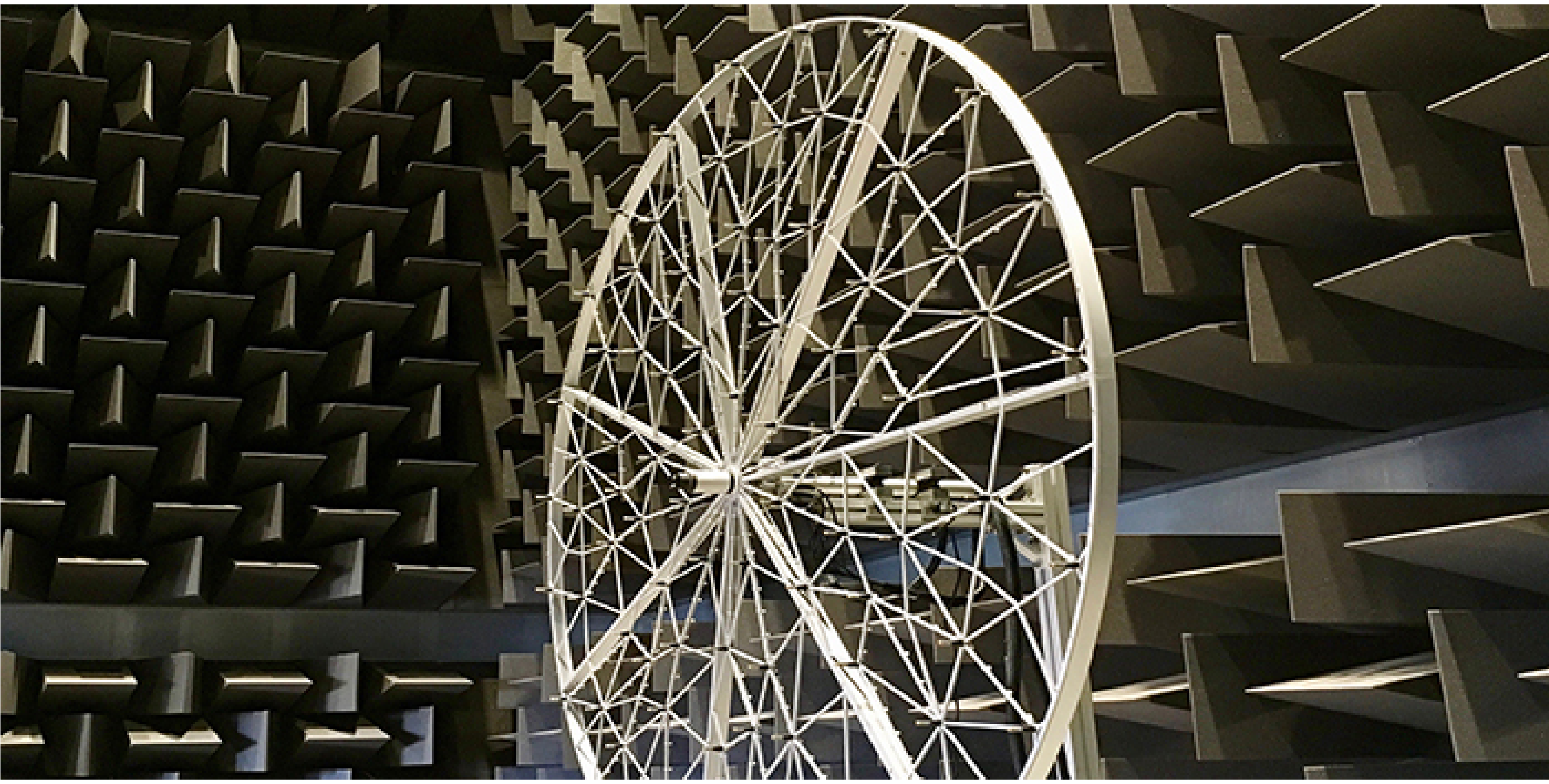

Cross-comparison and uncertainty quantification of aeroacoustic measurements performed in several wind tunnels

by

Guillem Vergés i Plaza

to obtain

the degree of Master of Science in Aerospace Engineering at the Delft University of Technology,

and the degree of Master of Science in Wind Energy at the Technical University of Denmark,

to be defended publicly on Wednesday August 3, 2022 at 13:00.

Student number:	5274281 (TU Delft), s203271 (DTU)	
Project duration:	November 1, 2021 – July 31, 2022	
Thesis committee:	Dr. A. Fischer,	Technical University of Denmark, supervisor
	Dr. D. Ragni,	TU Delft, supervisor
	Dr. S. Luesutthiviboon,	TU Delft, supervisor
	Dr. Ir. W. J. Baars,	TU Delft
	Dr. E. Barlas,	Ørsted
	Ir. W. A. Timmer,	TU Delft

Cover image: Poul La Cour Wind Tunnel microphone array. From `https://windenergy.dtu.dk`.

Acknowledgments

This Thesis is the end of the journey that started two years ago. I have not regretted the choice of joining EWEM for even a single second. I am very thankful for all the people who have made this joyful experience.

Firstly I want to thank my supervisors, Andreas Fischer, Daniele Ragni, and Salil Luesutthiviboon, for their guidance and suggestions throughout the project. I am especially grateful to have had the opportunity to travel to Southampton for the AIAA/CEAS Aeroacoustic Conference. It definitely was an inspiring experience. I am also thankful to Oliver Lylloff, Alexandre Suryadi, and Michaela Herr for their help with the wind tunnel results and the patience with my questions and continuous extra data requests. I have learned a lot from all of you.

I also want to thank my roommates and friends in Copenhagen for making it a lovely place to live. Thanks for listening when I tried to explain results I did not understand. Thanks to my fellow chefs at Vaca for making it an enjoyable place to work and teaching me the greatness of Argentinian cuisine. Thanks to my EWEM colleagues, especially for helping me to survive the online semester at Delft. Thanks to Oca and Gale for their music and visits to Copenhagen. Thanks to all my friends in Barcelona for all the online calls throughout these years.

Last but not least, I am extremely grateful to my parents and family for their support, unfortunately from a distance. And I cannot finish without thanking my girlfriend, Berta Mas Campabadal, for making my life better in every way.

To all of you, gracies!

Guillem Vergés i Plaza
Copenhagen, July 2022

Abstract

Trailing-edge noise can be the dominant noise source of diverse industrial applications, including wind turbines. Noise regulations may limit the power production and installation of new wind farms. There is a need to reduce it. In order to achieve so, we first need to predict it, and to do so we need experimental data to support and validate the new methodologies. A new experimental campaign has been carried out to provide a benchmark of trailing-edge noise applicable to wind turbine noise. It involves a broad range of Reynolds numbers and angles of attack, and covers the noise reduction effect of serrations. This Thesis studies the aforementioned novel data set. The trends of the far-field noise with the forcing of the boundary layer, angle of attack, and Reynolds number have been studied. Furthermore, scaling laws have been applied to compare different test conditions. The collapse quality has been studied, and the differences have been linked to the aerodynamics and possible post-processing effects. The effect of the serrations has also been studied. Additionally, the noise reduction dependence on the aerodynamic loading is discussed. The influence of the microphone locations on the far-field spectra uncertainty is also studied. The Monte-Carlo method has been applied using the Delay-and-Sum and Clean-SC beamformers. The effect of the input uncertainty correlation, wind tunnel velocity, facility, and algorithm are examined.

Contents

List of Figures

Nomenclature

Abbreviations

AWB	Acoustic Wind Tunnel Braunschweig
AWB-EM	AWB data from the Elliptic Mirror
AWB-MA	AWB data from the Microphone Array
BANC	Benchmark problems for Aiframe Noise Computations
BPM	Brooks, Pope and Marcolini model
Clean-SC	Clean based on Spatial Coherence
CLT	Central Limit Theorem
COP	Coherent Output Power
CSM	Cross-Spectral-Matrix
DAS	Delay-and-Sum
DLR	Deutsches Zentrum für Luft- und Raumfahrt (German Aerospace Center)
DTU	Technical University of Denmark
HRM	High-Reynolds Model
HWA	Hot Wire Anemometry
iid	independent and identically distributed
LLN	Law of Large Numbers
LRM	Low-Reynolds Model
LTT	Low-Turbulence Tunnel
NWB	Niedergeschwindigkeits Windkanal Braunschweig (Low-Speed Wind Tunnel Braunschweig)
OSPL	Overall Sound Pressure Level
PIV	Particle Image Velocimetry
PLCT	Poul La Cour Tunnel
PSF	Point Spread Function
SNR	Signal-to-Noise Ratio
SPI	Source Power Integration
SPL	Sound Pressure Level
TE	Trailing Edge
TUD	Delft University of Technology
TUD-A-L	A-Tunnel equipped with the Large nozzle (0.4x0.7 m)

TUD-A-S	A-Tunnel equipped with the Small nozzle (0.4x0.25 m)
UQ	Uncertainty Quantification

Greek letters

α	Angle of attack
β	Compressibility factor
δ_{99}, δ^*	Boundary layer thickness and displacement thickness
γ	Adiabatic index
$\gamma_{x,y}$	Coherence of the signals x and y
Λ	Body shape factor
μ	Dynamic viscosity or mean
ν	Kinematic viscosity
ρ	Air density
σ	Wind tunnel blockage factor in section 2.4. Standard deviation elsewhere.
θ	Angle acousic source-microphone relative to velocity direction (Figure 2.8)
ε_b	Blockage factor $\varepsilon_b = \varepsilon_s + \varepsilon_w$ (model + wake)
φ	Serration flap angle

Latin letters

$\bar{D}$	Directivity factor
$\tilde{a}$	Steering vector
AR	Aspect ratio
B	Number of blocks for the P. Welch algorithm
b	Span length
c	Airfoil chord or sound speed
C_a, C_l, C_d, C_m	Force coefficient (general, lift, drag, moment)
C_p	Pressure coefficient
f	Frequency
G	Cross-Spectral-Matrix
H	Distance source plane - microphone array plane.
h	Tunnel height for closed-section tunnels. Distance TE - shear layer for open-jet.
k	Wavenumber
M	Mach number
N	Number of microphones
q	Dynamic pressure
r	Distance source (or scan plane point) to microphone (or array centre)

Re	Reynolds number
$S_{x,y}$	Cross-power spectral density between signal x and y
St	Strouhal number
t	Airfoil thickness
U	Wind tunnel velocity
u_e	Edge velocity
u_t	Wall friction velocity
v_t	Transpiration velocity throgh Kevlar walls
y	Microphone signal Fourier-transformed

Subscripts and superscripts

$(\cdot)'$	Uncorrected wind tunnel quantity ($U, q, \rho, T, \alpha, C_a, \mu$)
$(\cdot)^H$	Complex conjugate transposed
$(\cdot)_\mu$	Mean (in Monte-Carlo method)
$(\cdot)_\sigma$	Standard deviation (in Monte-Carlo method)
$(\cdot)_{\text{scaled - freestream}}$	SPL scaled using freestream quantities and δ^*_{SS}
$(\cdot)_{\text{scaled - inner scales}}$	SPL scaled using inner boundary layer parameters
$(\cdot)_{\text{scaled - mixed scales}}$	SPL scaled using mixed boundary layer parameters
$(\cdot)_{eff}$	Effective (angle of attack)
$(\cdot)_{loc}$	(Standard deviation) relative to the microphone locations
$(\cdot)_{nb,1/3,1/12}$	Narrow band, one-third octave band, and one-twelfth octave band
$(\cdot)_{nom}$	Nominal (in Monte-Carlo method)
$(\cdot)_{ref}$	Reference quantity for the scaling
$(\cdot)_{SS}$	Suction side

1

Introduction

Trailing-edge noise

Trailing-edge noise is created from the interaction of the turbulent boundary layer, and its associated surface pressure fluctuations, with the trailing edge. It has a broadband spectrum: the different lengths and frequencies of the turbulent boundary layer on the airfoil generate a dispersed response, as opposed to a tonal noise that concentrates the energy content around a very narrow band of frequencies. The review of Howe [1], or the recently published one by Lee et al. [2] provide an excellent overview of this noise source and the current analytical, experimental, and computational tools used in its study.

Relevance and applications

But why do we want to study it in the first place? Trailing-edge noise is an important concern for various industries, primarily aviation and wind energy. New multi-rotor concepts like drones or Urban Air Mobility (UAM) vehicles are increasingly important in aviation. The higher number of propellers used in current configurations increases the broadband noise [3]. This broadband noise will be very important in urban environments because the dominant low-frequency tonal noise from UAM vehicles will probably be masked by the street noise [4]. And the broadband noise is mostly dominated by trailing-edge noise [5]. Even in helicopter noise, it is not a negligible noise source [6].

Trailing-edge noise also plays a key role in the wind turbine industry [7]. It is the main noise source of modern wind turbines, as demonstrated by the field measurements by Oerlemans et al. [8]. They conducted microphone array measurements on a three-bladed 58m diameter wind turbine and found that the main generation occurred at the outer part of the blades. Figure 1.1 shows a beamforming image from that study. The asymmetrical pattern was attributed to the combined effect of the trailing-edge noise directivity and the convective amplification. This is the cause of the so-called "swishing" sound of wind turbines, which can be particularly annoying [9]. The increased perceived annoyance of wind turbine noise [10] is an important industrial concern, since operating wind turbines may have to deviate from the optimal operating settings to meet the noise regulations [11]. The interest of reducing wind turbine noise can be exemplified by the SIlent ROtors by aCoustiC Optimisation (SIROCCO) project [12] or more recently by the Task 39 of the International Energy Agency (IEA) [13]. In this context, the trailing-edge serrations, a noise reduction device initially proposed by Howe [14], are increasingly studied and used for wind turbine blades [15]. Noise reductions of more than 3 dBA (OASPL) have been measured in the field using this mechanism [16]. There is ongoing activity to gain understanding of the flow physics around the serrations [17–20], design optimised geometries [19, 21–23], and improve the prediction models [24, 25].

Benchmarking

To fulfill this interest in reducing the trailing-edge noise, we need tools that allow us to predict it accurately. To predict it, we first need measurements to validate the methods. The literature has plenty of studies that compare new methods to experimental results [24, 26–29]. However, it was continuously reported that the available experimental data was limited and scattered [30–32]. To overcome this, the American Institute of Aeronautics and Astronautics (AIAA) has organized, since 2010, a series of ongoing workshops called Bench-

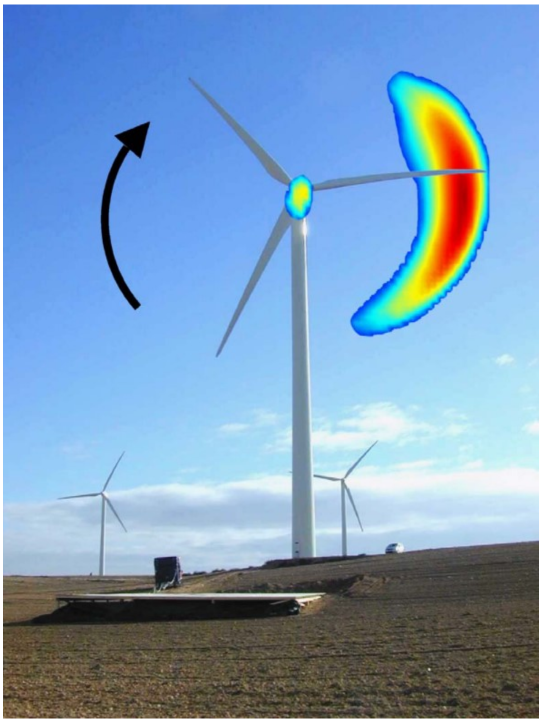

Figure 1.1: Noise sources over a Siemens-Gamesa wind turbine (58m diameter and 0.85 MW). Averaged over several revolutions. From [8].

mark Problems for Airframe Noise Computations (BANC). The aim is to progress in the understanding and prediction of the most critical airframe noise sources. It is divided into different categories, representing each relevant source, and the first category of the workshops is the airfoil trailing-edge noise. The goal is to cross-check available measurement data with different computation methods. It is also expected to define a problem structure that will help future experiments fill the validation data gaps [33]. The results of the initial workshops (BANC-II-1, 2012 [34]) covered five test cases: NACA 0012 at $Re_c = 1.5 \times 10^6$ $@\alpha = 0°, 4°, 6°$, NACA 0012 at $Re_c = 1.0 \times 10^6$ and $\alpha = 0°$, and DU-96-180 at $Re_c = 1.13 \times 10^6$ and $\alpha = 4°$. The first four cases were defined based on the available data on turbulent length scales and transition locations. Different contributors submitted computational predictions for these cases, and trends and deviations in the different approaches were identified. The cross-comparisons allowed to correct methodologies, and further work lead to better collapse in the predictions in the subsequent editions [35]. In the 4th edition two new cases were added: a cambered airfoil with natural transition was introduced. The selected airfoil was the NACA 64-618 at 45 m/s and -0.88 deg and 4.62 deg. As of now[1] the baseline case (#1, NACA 0012 at $\alpha = 0$ deg) predictions lie within the ±3 dB scatter band of the measurements. This is an improvement of the computational agreement since the first edition, but the measurement database used is still the same. The scatter in the experimental data effectively sets the resolution at which comparisons can be made. An improvement on the experimental data collapse could allow for the computations to tackle the remaining small differences. The available data-set is formed of results from different facilities, with distinct models, measurement techniques, and post-processing. Figures 4 to 7 of the BANC-II-1 problem statement [33] show the discrepancies of these measurements.

Current issues and uncertainties

The BANC workshop is a great and important effort to understand trailing-edge noise and cross-validate new methods and measurements. However, it has some limitations for its use in wind turbine applications. The Reynolds number range is an issue since the maximum Re_c is 1.5×10^6. Cases at high lift coefficients are also missing. This is important since the airfoils are heavily loaded in operation, where the effectiveness of noise reduction strategies should be assessed. Regarding noise reduction, it is also a must to include serrations in the database to have a complete benchmark. Additionally, the existing database is composed of different

---

[1] BANC-V-1 is the last edition of the workshop. Unfortunately, no summary papers are available for editions IV and V.

campaigns, where the model, conditions, and processing uncertainties are mixed up. It would be interesting to try to isolate and quantify them so the scatter (±3 dB) between the different campaigns can be better understood. For instance, the use of the same model or post-processing technique could be an improvement in this direction. These gaps were partially tackled in the work of Ferret Gasch et al. [29]. Two Siemens-Gamesa cambered airfoils were tested to a maximum Re_c of 3.7×10^6. These models were much more representative of blade airfoils, and the Reynolds number was much higher than in BANC. The measurements were used to blindly test the accuracy of different prediction codes, similarly to the BANC objectives. Their recommendations insisted again on the need to conduct uncertainty quantification of the measurements and improve the validation database especially at moderate to high Reynolds numbers.

Summary

We have introduced the phenomena of trailing-edge noise and why it is relevant, especially for wind energy applications. If we want to reduce it, the first step is to predict it well. To improve the prediction methods, we need equally good experimental data to validate them. The BANC workshop is the most significant effort in this regard. However, the measurement data used there has still some gaps for its applicability to wind turbine noise. We would like to have data at higher Re_c, C_l, and with serrations installed. Additionally, the current measurements were found to have of an important scatter. Since the data was obtained from different facilities, models, and methods, the source of the differences is not clear.

We want to add new data to fill this gap and have a well defined benchmark for trailing-edge noise. This Thesis deals with new measurements carried out in this regard. The experimental data will be compiled, studied, and characterised. The specific research objectives are given in Chapter 3, after the basic background in experimental acoustic testing is explained in Chapter 2.

Report structure

Chapter 2 covers the background on aeroacoustic wind tunnel testing. The state-of-the-art methods and experimental set-ups are covered, and the main relevant concepts are introduced. Chapter 3 defines the research objectives of this Thesis. Chapter 4 explains the experimental set-up and how the data has been processed and compared. Chapter 5 presents the analysis and further processing of the results. The main characterisation of the data is however presented in a separate conference paper, attached in Appendix B. In the Results section (Chapter 5) we explore more the data, study possible reasons for the differences identified, and start to quantify its uncertainty. Finally, the conclusions and recommendations are given in Chapter 6.

2

Background on aeroacoustic wind tunnel testing

2.1. Wind tunnel types

The ideal aeroacoustic wind tunnel can faithfully replicate the aerodynamics of the device or flow configuration of interest and can measure the far-field sound it produces with the least amount of background noise. Reynolds numbers that realistically represent the application of interest and minimal and predictable interference corrections are required for accuracy in aerodynamics. Low turbulence and very uniform free stream is demanded. The closed test section is the typical wind tunnel setup for aerodynamic experiments. Rigid parallel walls direct the flow over the model. We will first discuss the use of such tunnels for aeroacoustic applications.

Hard-walls closed-section wind tunnel

Microphones can be installed on the wind tunnel walls or placed in the flow utilizing aerodynamic mounts and nose cones. Closed test section wind tunnel's walls may be coated to lessen acoustic reflections and reverberation. By protecting it from the flow to reduce pressure fluctuations caused by turbulence that might overwhelm the acoustic pressure signal, the performance of microphones in a closed test section facility can be considerably enhanced. A microphone array is often placed in a shallow hole in one of the test section walls, which is then sealed off with an acoustically transparent membrane. There are particular conditions that make it easier to conduct useful acoustic measurements in closed test section wind tunnels. For instance, large facilities where the acoustic far field may be reached within the test section, or in the analysis of louder sources that are not overshadowed by reverberation or background facility noise. The wind turbine fan, turning vanes, and wall roughness noise from both upstream and downstream of the test area are often the main sources of background noise. Such parasitic sources may be directly captured by microphones positioned in the flow or on the test section walls. [36].

The dominant correction in closed wall wind tunnels is for blockage. Compared to the incoming flow's actual speed, this is defined as a change in the effective free stream velocity. Additionally, blocking results in a small angle of attack inaccuracy. The corrections are very well understood and everyone applies the same ones, which makes the results in different facilities more comparable [37].

An example of such facility is the NASA Glenn 9x15 foot Low Speed Wind Tunnel (Figure 2.1), which has been widely used for model turbofans and propellers [38].

Open-jet wind tunnel

The open-jet test section is a far better arrangement from an acoustic standpoint. In this case, the free stream is projected as a jet through an anechoic chamber, and the test section walls are partially or entirely removed. The model is then positioned in the jet so that the sound it generates travels through the jet shear layer into the microphone instrumentation, located outside the influence of the flow field. Smaller wind tunnels are thought to be a good fit for open-jet anechoic wind tunnels because an adequately sized anechoic chamber

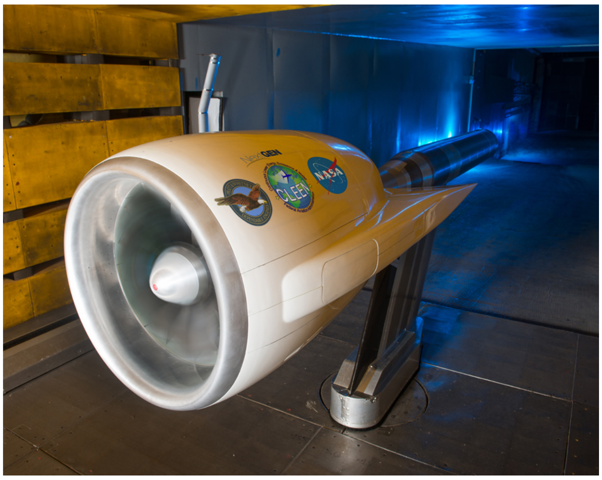

Figure 2.1: Test section of the NASA Gleen 9x15 foot Low Speed Wind Tunnel. Retrieved from https://www.nasa.gov/specials/9x15360/.

makes it relatively simple to position a microphone array in the far-field. However, there is a chance that the flow's interaction with the contraction nozzle or the collector would produce unwanted noise [36].

While the open-jet test section structure can offer a good solution to the acoustic objectives of a wind tunnel test, depending on the model size compared to the test section, this configuration can suffer from significant aerodynamic interference effects. In order to adequately describe both aerodynamic and acoustic performance, it may be necessary to conduct separate test runs in various wind tunnels or test sections due to potential limitations on the accuracy of the aerodynamic data acquired. The deflection of the jet during airfoil testing is principally responsible for the aerodynamic interference. This reduces the angle of attack experienced by the airfoil from the geometrical one [39]. Apart from this necessary aerodynamic corrections, the acoustic measurement is also complicated since the pressure waves have to travel through a free shear layer. This leads to refraction [40] and also to unsteady amplitude and phase distortions due to the jet's turbulence [41, 42]. These phenomena change the effective distance traveled by the sound waves, the phase and amplitude of them, and hence may diminish their correlation.

Examples of this facility type include the A-Tunnel at TU Delft (Figure 2.2) [43] or the DNW-NWB at DLR [44].

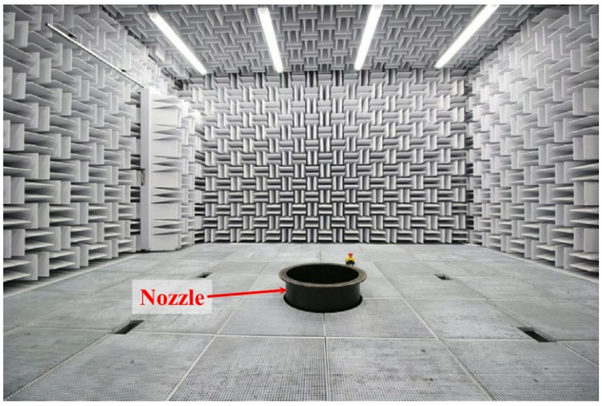

Figure 2.2: Anechoic chamber and nozzle of the A-Tunnel at TU Delft. Retrieved from [43].

Hybrid-anechoic wind tunnel

The hybrid anechoic tunnel is a third design utilized in aeroacoustic testing. Here, the closed test section's hard walls are exchanged out for acoustically transparent walls (also known as acoustic windows), which are often constructed of Kevlar fabric. Acoustic instrumentation is installed in an anechoic chamber external to the test section. The hybrid configuration's main goal is to combine the best aspects of closed and free-jet test sections for aeroacoustic testing. Enclosing the jet in Kevlar walls decreases corrections to closed-test section levels from an aerodynamic viewpoint. However, the flexibility and porosity of the acoustic windows should also be taken into account to modify the existent corrections. A hybrid test section's acoustic windows eliminate the requirement for a jet collector (and any noise it could produce) and allow for a significantly longer test section proportional to its width. Additionally, compared to an open jet, acoustic instrumentation can be positioned much closer to the flow and, consequently, to the sources of interest. These acoustic advantages are compared against the need to account for acoustic losses for sound transmission through the window and the existence of some parasitic noise at frequencies higher than around 15 kHz created by the flow over the acoustic window material [36].

The Virginia Tech Stability Wind Tunnel [45] or the Poul La Cour Tunnel (PLCT) at DTU (Figure 2.3) [46] are state-of-the-art hybrid-anechoic wind tunnels.

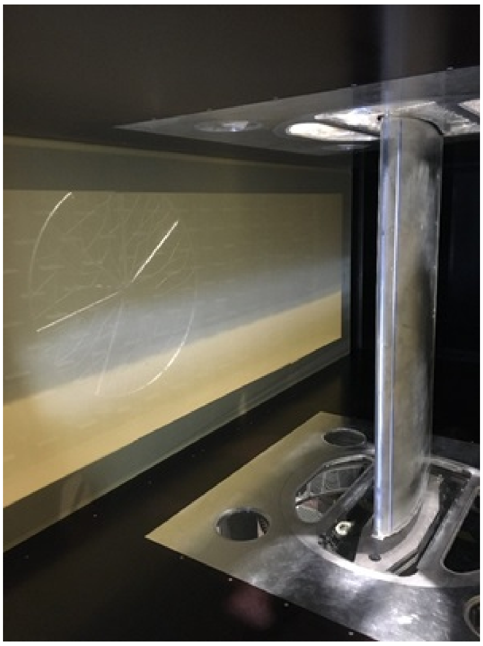

Figure 2.3: Test section of the PLCT at DTU. The microphone array can be seen behind the Kevlar wall. Retrieved from `https://www.plct.dk/`.

2.2. Measurement techniques

After introducing the different wind tunnel types, we can now discuss about how the acoustic measurements are taken. Different approaches of increasing complexity and accuracy are presented in this Section.

Single microphone

The main building block for all the acquisition techniques is the microphone. Condenser microphones are the type commonly used for aeroacoustic applications. This type of microphone uses the change in capacitance between a membrane and a backing plate to measure the acoustic pressure. In reaction to sound, the membrane vibrates, and as the distance between the membrane and the backing plate varies over time, the capacitance also fluctuates. A cheaper alternative would be the electret microphones (present in e.g. cell phones). The diaphragm or the fixed plate is built with a ferroelectric pre-polarized material, eliminating the need to provide power to the microphones. However, the characteristics of these microphones are usually not as well defined as the scientific-grade condenser microphones. Meticulous calibration should be performed if electret microphones are to be used. With condenser microphones, calibration is also necessary, but their response is usually flat with frequency and can be calibrated by checking just one frequency. Electret microphones have a more frequency-dependent amplitude and phase response; thus, the calibration is more complicated. Either way, calibrations can be conducted using a pistonphone. This device produces acoustic pressure fluctuations of a determined amplitude by the motion of an oscillating piston at a given frequency

[36, 47].

The sizes of instrumentation microphones range widely. Because acoustic pressure is integrated over a greater diaphragm area, larger diameter microphones are more sensitive to those fluctuations. A good signal-to-noise ratio is required when detecting especially quiet sources. The larger diaphragm also has more inertia, which limits the frequency response. Smaller diameter microphones may have greater ranges (in frequency and level) despite having worse sensitivity. For trailing-edge noise, it makes sense to have a limited frequency range at high frequencies in order to achieve better sensitivity at low frequencies. Another phenomenon to pay attention to is when the size of the diaphragm is comparable to the sound wavelength. The angle of the incident pressure waves may affect the amplitude response of the microphone at these (high) frequencies [36].

The positioning of the microphone (or microphones) is a compromise. On one hand, we would like to place it as close as possible to the source of interest to maximize the signal-to-noise ratio. On the other hand, it is better to locate them in the acoustic far-field in order to simplify the understanding of the readings and avoid e contamination from aerodynamic pressure fluctuations. Another concern is the orientation: we want to point them to the source so that the wavefronts are parallel to the diaphragm and the microphone response is optimal. Additionally, microphones are often positioned at least a quarter wavelength away from the walls to take full advantage of the anechoic chamber's best properties [36, 47].

Using a single microphone does not directly allow us to distinguish between the sources of interest and background noise. A part from the inability to localize the source, it could be that the source of interest is completely masked by extraneous noise. More advanced techniques that can help to tackle this issue are described below.

Elliptic mirror

The first approach to increase the signal-to-noise ratio is to use directional microphones to enhance the signal measured from the model. This method gained popularity after the work of Grosche in 1977 [48], and it was initially developed for jet noise applications [49]. The acoustic waves generated by a small volume of the source distribution are focused upon the microphone by a large concave mirror. The working principle is illustrated in Figure 2.4. The mirror and the microphone are located in the acoustic far-field, which minimises the near-field effects or the measurement of aerodynamic pressure fluctuations. By traversing the whole system (mirror and microphone), different focal points can be measured. This allows to measure separately the acoustic intensity from different flow regions [48].

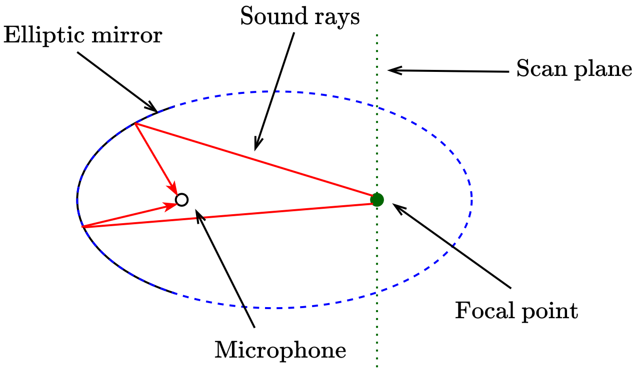

Figure 2.4: Principle of elliptic mirror. Reproduced from [50].

An advantage of this method, besides the location capabilities, is the high mechanical gain of the system. Gain here is defined as the ratio between the measured acoustic pressure and the acoustic pressure that would be measured in the free-field by a single microphone. Since the total signal measured by the microphone is the sum of the waves traveling from different points of the mirror, the effect of the (constructive or destructive) interferences between waves has a big effect. Effective gains up to 30 dB can be achieved [48]. However, the gain and resolution of the system are frequency and velocity dependent. [51] Therefore, extensive corrections need to be applied if we want to extract the absolute source levels. Additionally, measurements take a long time since the mirror needs to be physically moved for each scan point. This makes them expensive, and particularly unsuitable for large wind tunnels [50].

The measurements by Herr [52] are an example of how all the required corrections are applied for the AWB at DLR. The measurements are corrected for extraneous noise sources, sound wave convection, spatial resolution of the mirror, system's gain, and shear layer refraction.

Coherent Output Power (COP)

This technique was firstly introduced by Piersol in 1978 [53] and used widely in the trailing-edge noise studies of Brooks in the eighties [26, 54]. It has still been used in more modern measurements such as the work of Herr in 2010 [31].

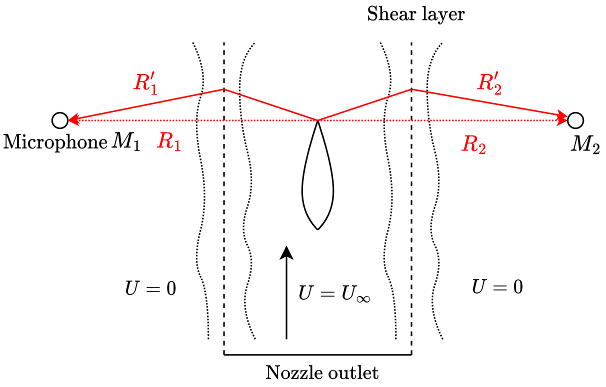

Figure 2.5: (Exaggerated) sketch of shear layer refraction and acoustic ray transmittion paths. Reproduced from [26].

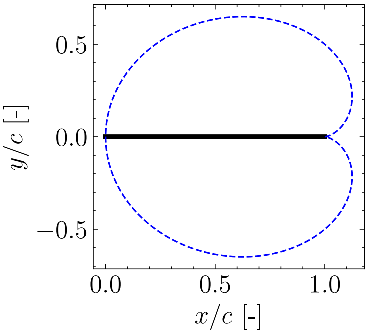

Figure 2.6: Trailing-edge noise directivity for an observer in a plane parallel to the trailing edge. Black solid lines shows the flat plate with trailing-edge at (0,1). Blue dashed line shows the directivy in polar coordinates centered at (0,1), given by $D = \sin(\theta/2)^2$.

This technique is based on the previous knowledge that trailing-edge noise is coherent and anti-symmetric in both sides of the airfoil [55]. A visual representation of the directivity for an observer in a plane parallel to the trailing edge is shown in Figure 2.6. Note that this cardioid directivity directs most of the sound radiation upstream (to the leading edge), and that the contributions to the normal direction of the airfoil are symmetrical. With that in mind, we can now have a look at the microphone positions of Figure 2.5 and define the following equations for the auto-spectrum of the microphones M_1, M_2 [26]:

$$S_{M_1,M_1} = S_{u,u} + S_{n,n}, \qquad S_{M_2,M_2} = S_{v,v} + S_{m,m} \tag{2.1}$$

Where $S_{u,u}$ and $S_{v,v}$ are the contributions of the trailing-edge noise perceived at M_1 and M_2 respectively. $S_{n,n}$ and $S_{m,m}$ are the background noise contributions (shear layer, nozzle lips, etc.) measured at the microphones. The cross-spectrum between both microphones is:

$$S_{M_1,M_2} = S_{u,v} + S_{u,m} + S_{n,v} + S_{n,m} \tag{2.2}$$

Trailing-edge noise depends on the boundary layer state in the vicinity on the trailing edge. The possible correlated source erasing from the wake may be neglected given the rapid decay of the transient turbulent statistics [26]. Hence we can discard $S_{u,m}$ and $S_{n,v}$. Therefore, if $S_{n,m}$ is small compared to $S_{u,v}$ then the cross-spectrum of M_1 and M_2 is essentially measuring the trailing-edge noise. Note that it is only required that $S_{n,n}$ and $S_{m,m}$ are mutually incoherent. No assumptions about their auto-spectrum are required. Considering the distances from the trailing edge to the microphones R_1 and R_2, we can write:

$$S_{M_1,M_2} = S_{TE}(f)\exp\left(i[\pm\pi + k(R_1 - R_2)]\right) \tag{2.3}$$

Where $k = 2\pi f/c$ is the wavenumber, and the $(\pm)$ operand accounts for the anti-symmetry of the pressure fluctuations. The exponential corrects for the phase difference if $R_1 \neq R_2$. S_{TE} is the trailing-edge noise spectrum that would be measured in the absence of background noise. Note, as shown in Figure 2.5, that the distance traveled by the sound waves R_1', R_2' is not equal to the geometrical one R_1, R_2 due to shear layer refraction. In Equation (2.3) the corrected distances should be used. Shear layer refraction corrections will be treated in Section 2.4.

Apart from identifying trailing-edge noise, cross-correlation between microphone pairs can also be used to separate other sources such as the leading-edge noise. This was used in the measurements carried out by Brooks, Pope, and Marcolini [54]. Section 4 and Appendix A of their report shows how trailing-edge, leading-edge, and background noise could be separated by extending the reasoning described here.

Microphone array

While the COP technique works to quantify trailing-edge noise, it is built on the specific trailing-edge noise directivity pattern and thus lacks generality for all aeroacoustics applications. The elliptic mirror approach provided a good general way to localize sources, but the measurements took a long time and therefore were expensive. Alternatively, since the seventies the studies have been more centered on the development of the acoustic array [56]. A microphone array is a collection of microphones whose signals are mixed in a certain way that amplifies sound coming from a certain scan point while attenuating sound coming from other directions. The different microphone signals are delayed and summed to create this signal combination according to the system's geometry. This combination (electronic steering) is accomplished by introducing microphone-dependent phase shifts in the frequency domain. This is why it is also called "phased array". The benefit of this method over acoustic mirrors is that only a brief measuring period is required because the scanning process is carried out later [50].

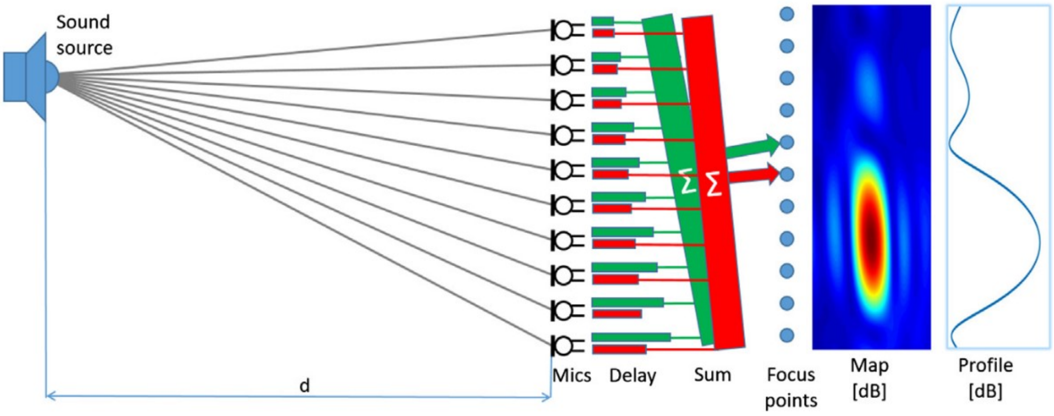

Figure 2.7: Microphone array sketch. Retrieved from [57].

The technique to apply this signal combination and locate sources is called beamforming. Many algorithms are available, and they were developed for other applications such as astronomy (e.g. [58]). Even within acoustics, microphone arrays and beamforming are common techniques not necessarily restricted to aeroacoustics.

2.3. Beamforming

The review of Chiariotti et al. [57] gives an overview of general acoustic beamforming techniques and possible applications. The review of Merino-Martinez et al. [59] describes the beamforming methods specifically used for aeroacoustic measurements. In this Section we will explore the basics of beamforming for aeroacoustics and the methods that will be used later in this Thesis.

The process starts with the calculation of the Cross-Spectral-Matrix (CSM). It is a matrix of size $N \times N$ for each frequency of interest, where N is the number of microphones. It represents the cross-power-spectral-density between each microphone pair. The Peter Welch algorithm is commonly used [60]. Say the data has been recorded at sampling frequency f_s during an acquisition time T_{acq}. The signal can be then divided into blocks of length H. These blocks may be overlapped with a percentage ν. A window function can also be applied. Next, the cross-power spectral density (CSD) is calculated between each microphone pair for each block, given by:

$$S_{xy}(f) = \int_{-\infty}^{\infty} \left[\lim_{T\to\infty} \frac{1}{T} \int_{-\infty}^{\infty} x_T^*(t-\tau) y_T(t) dt \right] e^{-i2\pi f\tau} d\tau \tag{2.4}$$

The CSD is the Fourier transform of the cross-correlation function of the two signals $x(t)$ and $y(t)$. This is usually calculated resolving the discrete Fourier transform by means of the fast Fourier transform algorithm (FFT) to improve the computational cost. The CSD between each microphone pair composes the CSM. Note that it contains the relative phase information between them. The power spectral density (PSD) of each microphone forms the diagonal. This is calculated for each block, and then averaged to reduce the variance of individual segments. In short, the Cross-Spectral-Matrix G for a determined frequency is given by:

$$G = \frac{2}{\omega_0 B} \sum_{b=1}^{B} y(b) y^H(b) \tag{2.5}$$

Where B is the number of blocks, ω_0 is a correction factor to account for the overlapping, and $y(b)$ is the microphone signal of each block Fourier-transformed. The operand $(\cdot)^H$ denotes complex conjugate transpose. The use of the single-sided spectrum imposes the factor of 2. Note again that the diagonal of the CSM corresponds to the auto-powers of each microphone. When the microphones are under the influence of the aerodynamic pressure fluctuations, the background noise is too high, or the coherence loss dominates, these auto-powers may have much larger levels than the off-diagonal terms. For instance, if the array can feel the influence of a boundary layer (or shear layer), it is likely that the aerodynamic pressure fluctuations are much higher than the acoustic pressure fluctuations. These larger signals will only appear in the diagonal because the off-diagonal terms will not be coherent (unless the microphones are very close to each other). Therefore, the diagonal is often removed from the CSM to avoid the introduction of such phenomena [50].

Delay-And-Sum

The Delay-And-Sum (DAS), or Conventional Frequency-Domain Beamforming (CFDBF) method is based on summing delayed and weighted versions of each microphone signal. The delays and weights are determined such that the array is "electronically steered" towards the source of interest. They are calculated according to the relative distances between the source and microphones. This is done for each frequency of interest, and the subsequent equations correspond to a determined narrow-band frequency f. If we consider L monopole sources, the DAS estimate for each of them ($l = 1,...,L$) is defined as:

$$s_l(b) = \frac{1}{N} \tilde{a}_l^H y(b) \tag{2.6}$$

Where N is the number of microphones and $\tilde{a}_l$ is the steering vector for the l-th source. Both $\tilde{a}_l$ and $y(b)$ are complex vectors of size N. The steering vector is a known vector that accounts for the mentioned delays and weights and corrects for the different propagation for each microphone. There are different steering vector formulations available in the literature [61]. We can consider the following one, which aims to compensate for the amplitude and phase:

$$\tilde{a}_l = \frac{1}{r_{l,0}} \left[r_{l,1} \mathrm{e}^{-\mathrm{j}k r_{l,1}}, r_{l,2} \mathrm{e}^{-\mathrm{j}k r_{l,2}}, \ldots, r_{l,N} \mathrm{e}^{-\mathrm{j}k r_{l,N}} \right]^{\mathrm{T}} \tag{2.7}$$

The distances $r_{l,n}$ correspond to the distance between the source l and the microphone n. $k = 2\pi f/c$ is the wavenumber of the pressure waves, and c is the sound speed. The distance $r_{l,0}$ is the distance between the source l and the center of the microphone array, and it is just a normalization factor. Then, the estimated power level of the l-th source is:

$$P_l = \frac{2}{\omega_0 B} \sum_{b=1}^{B} |\tilde{s}_l(b)|^2 \tag{2.8}$$

Instead of working directly with the pressure data, it is more convenient to make use of the previously defined CSM (Equation (2.5)):

$$P_l = \frac{1}{N^2} \tilde{a}_l^H G \tilde{a}_l \tag{2.9}$$

In practice, the location and number of the sources l are unknown, so a scan grid is defined. These equations are solved for every point within the scan grid, and the level is retrieved. This allows us to identify noise sources but also to quantify them. Once the whole scan grid is resolved, the obtained beamforming image can be used to integrate the levels around the region of interest. To do that, Source Power Integration (SPI) is used.

Source Power Integration

The use of DAS rarely leads to the correct absolute source powers. The source map obtained is the addition of the array response for each source. The signal perceived had been convoluted with the Point Spread Function (PSF). This is, the array response or beam pattern to a point source. The absolute levels can then be extracted directly only if the sources are point sources with uniform directivity (in the array direction), the resolution is high enough and there is no coherence loss. These are not fulfilled in aeroacoustic testing. To overcome this, the Source Power Integration is used [50, 62], which aims to limit the influence of the array response in the actual levels. It sums all the source power estimates in the desired integration region. Then the result is normalized such that the exact power is obtained for a simulated point source in the centre of the integration region. The response of this simulated point source is calculated using the PSF. Stated mathematically, the integrated power P_I in the integration region L is:

$$P_I = \frac{\sum_{l=1}^{L} P_l}{\sum_{l=1}^{L} \mathrm{PSF}(\tilde{a}_l, \tilde{a}_s)} \tag{2.10}$$

Where $\mathrm{PSF}(\tilde{a}_l)$ is the response of the simulated point source at the scan grid point l (and thus with corresponding steering vector $\tilde{a}_l$). $\tilde{a}_s$ is the steering vector of the point source, located at position s.

$$\mathrm{PSF}(\tilde{a}_l, \tilde{a}_s) = \tilde{a}_l^H \left(\tilde{a}_s \tilde{a}_s^H\right) \tilde{a}_l \tag{2.11}$$

Clean-SC

A more advanced beamforming technique is Clean [58]. It was designed by astronomical researchers to eliminate side lobes of very bright stars. It is actually a post-processing treatment of the DAS results. It starts by searching for the location of the maximum source power in the beamforming image. Then, the theoretical beam pattern (PSF) of that source (including side lobes) is subtracted from the image. The "dirty" pattern is replaced by a "clean" one which only includes the main lobe. This procedure is done in an iterative manner for multiple sources.

The drawback of this procedure is the assumption that the source beam patterns are based on PSFs. It is assumed that the problem may be characterised by a finite number of point sources, and that there is uniform source directivity and no coherence loss. This is not the case in most of the aeroacoustic tests. Sijtsma [63] proposed an extension to this method and named it Clean-SC (Clean based on spatial Source Coherence). The idea and the iterative procedure is exactly the same as in the original. The essential difference lies in how the "dirty" sources are removed. In the Clean algorithm the PSF is used, whereas in Clean-SC computations the map is created solely based on the CSM retrieved from the source(s) of question. A "degraded" CSM is iteratively built as:

$$G = \varphi \sum_{i=1}^{I} P_l^{(i-1)} h^{(i)} h^{H(i)} + D^{(I)} \tag{2.12}$$

Where D is the degraded CSM and h is calculated from the maximum source of the degraded map assuming incoherent sources. φ is just a relaxation factor. The "undegraded" part of the CSM ($\varphi \sum_{i=1}^{I} P_l^{(i-1)} h^{(i)} h^{H(i)}$) contains the essential information of the most important sources.

2.4. Wind tunnel corrections

When the wind tunnel types were introduced we saw that all the set-ups proposed required aerodynamic and acoustic corrections. These are summarized in this Section.

Aerodynamic corrections for hard-walls closed-section wind tunnels

We will start from the basic and more common case: a relatively thin airfoil with attached flow in a hard-walls close-section wind tunnel. This is a century-old problem, studied since the work of Lock in 1929 [64]. The presence of the model changes the flow field that would develop without it. The airfoil blocks part of the available cross-sectional area, leading to an increase of velocity. The wake also contributes to this effect and it additionaly induces a pressure gradient in the flow direction. Moreover, the streamline curvature induced by the airfoil loading is altered by the tunnel walls. The corrections commonly used to account for those effect are given since the works of Allen and Vincenti [37] and Garner et al. [65].

Let us tackle **blockage** in the first place. This is the increase of the perceived velocity by the model due to the combined presence of the model and its wake:

$$U = (1+\varepsilon_b)U' \tag{2.13}$$

ε_b is the total blockage factor, U' is the uncorrected velocity and U is the corrected one. We can put it in terms of the dynamic pressure:

$$\frac{q}{q'} = \frac{\rho}{\rho'}\left(\frac{U}{U'}\right)^2 \tag{2.14}$$

The quantities with a prime will be always the uncorrected version of the parameter. The true density is found from the isentropic relation:

$$\frac{\rho}{\rho'} = \left(1 - \frac{\gamma-1}{2}M'^2\left[\left(\frac{U}{U'}\right)^2 - 1\right]\right)^{\frac{1}{\gamma-1}} \tag{2.15}$$

Using Equation (2.14) we can correct for a given force coefficient by applying:

$$C_a = C'_a\left(\frac{q}{q'}\right) \tag{2.16}$$

Additionally, we should correct the Reynolds and Mach number similarly:

$$Re = Re'\left(\frac{\rho}{\rho'}\right)\left(\frac{\mu'}{\mu}\right)\left(\frac{U}{U'}\right) \qquad M = M'\left(\frac{U}{U'}\right)\sqrt{\frac{T'}{T}} \tag{2.17}$$

The correction for viscosity and temperature are given by Equation 30 of Allen and Vincenti [37] and are again based on isentropic flow relations. We know now how we should correct all the environmental conditions of the test, but we have still to determine what is the blockage factor ε_b. To do so, let's separate the model and the wake contribution:

$$\varepsilon_b = \varepsilon_s + \varepsilon_w \tag{2.18}$$

ε_s and ε_w are the solid (from the model) and the wake blockage respectively. The solid blockage is analytically calculated using potential flow theory. According to Allen and Vincenti [37]:

$$\varepsilon_s = \frac{\Lambda\sigma}{\beta^3} \tag{2.19}$$

Where Λ depends on the shape of the base profile and σ depends on the size of the airfoil relative to the tunnel height:

$$\Lambda = \frac{16}{\pi}\int_0^1 \frac{y}{c}\sqrt{(1-C_p)\left(1+\left(\frac{dy}{dx}\right)^2\right)}\,d\frac{x}{c} \tag{2.20}$$

$$\sigma = \frac{\pi^2}{48}\left(\frac{c}{h}\right)^2 \tag{2.21}$$

Where h is the tunnel height, c is the airfoil chord, C_p is the base profile pressure coefficient at chord position x, and y is the normal coordinate. Alternatively, in [65] another expression is proposed:

$$\varepsilon_s = \frac{\pi}{6}\left(1+1.2\beta\frac{t}{c}\right)\frac{A}{\beta^3 h^2} \tag{2.22}$$

A is the airfoil cross-sectional area, $\beta = \sqrt{1-M'^2}$ is the compressibility correction factor and t is the airfoil thickness. The difference in the results from Equations (2.19) and (2.22) is low [66]. Up to now, we have not considered the effect of the lift. Equation 5.15 of [65] provides a way to account for the angle of attack α (in radians):

$$\varepsilon_s(\alpha) = \varepsilon_s\left(1 + 1.1\beta\frac{c}{t}\alpha^2\right) \tag{2.23}$$

Now we are only missing the contribution of the wake. It can be analytically related to the measured drag coefficient using conservation laws, and it is given by [65] as:

$$\varepsilon_w = \frac{1}{4}\left(\frac{c}{h}\right)\frac{1 + 0.4M'^2}{\beta^2}C'_d \tag{2.24}$$

Besides the blockage, the model wake also creates a pressure gradient in the flow direction. It is also called **wake buoyancy**, and it should be taken into account for the drag calculation if it is measured using a balance or the model pressure distribution [37]:

$$C_d = C'_d\left[1 - \frac{1 + 0.4M'^2}{\beta^3}\Lambda\sigma - \left(2 - M'^2\right)\varepsilon_b\right] \tag{2.25}$$

Now we need to address wall effect on the curvature of the streamlines, or **lift interference**. Since the streamlines along the wall must be straight this affects the development of the whole flow field. Using vorticity-based methods, Allen and Vincenti wrote: [37]

$$\alpha = \alpha' + \Delta\alpha \tag{2.26}$$

$$C_l = \left(C'_l + \Delta C_l\right)\frac{q'}{q} \tag{2.27}$$

$$C_m = \left(C'_m + \Delta C_m\right)\frac{q'}{q} \tag{2.28}$$

The moment coefficient C_m is based at $x/c = 1/4$. The increments $\Delta\alpha, \Delta C_l, \Delta C_m$ quantify the effect of the lift interference, and are given by:

$$\Delta\alpha = \frac{\sigma}{2\pi\beta}\left(C'_l + 4C'_m\right) \tag{2.29}$$

$$\Delta C_l = -C'_l\frac{\sigma}{\beta^2} \tag{2.30}$$

$$\Delta C_m = C'_l\frac{\sigma}{4\beta^2} \tag{2.31}$$

These corrections are truncated at $(c/h)^2$. They can only be applied up to $c < 0.4\beta h$ [65]. Section 2.2.2. of Garner et al. [65] extends them to the order $(c/h)^4$.

All these corrections should also be present in the pressure distribution measurements. This can be done, in the same logic as the previous derivations, following Equation 74 of [37]. Figure 2 of [66] provides a practical example of how well the wind tunnel data at different c/h matches after the corrections are applied. The same reference outlines correction schemes to be applied beyond the attached regime. When the angle of attack is too large, the corrections pointed here cannot be applied. A different methodology should be then used.

Aerodynamic corrections for open-jet wind tunnels

The use of open-jet wind tunnels suppresses the need to correct for blockage and wake buoyancy, because the wake is free to expand. Nonetheless, it brings other effects that should be corrected for. Those are the down-wash due to the airfoil finite span, and the streamline curvature induced by the airfoil loading. The former is given by the 3D effects created at the model tips: since the pressure difference must go to zero, two vortices are created which reduce the angle of attack perceived by the model. This can be reduced to a very large extent by the use of side-plates, which help with the 2D flow approximation. In that case, Mangler [67] proposed:

$$\alpha = \alpha' - \kappa \frac{1}{2\pi AR} C_l' \tag{2.32}$$

$$C_d = C_d' - \kappa \frac{1}{2\pi AR} C_l'^2 \tag{2.33}$$

The angle of attack correction is in rad, $AR = b/c$ is the aspect ratio and κ depends on the side-plate geometry.

This down-wash correction is a second order correction provided that side-plates are used. The streamline or jet curvature is usually more relevant. If the upper and lower boundaries are free, the lift of the airfoil induces a deflection of the incoming jet. This deflection will generate, in turn, an effective angle of attack change and will increase the measured drag. Generally, the corrections for open-jet are larger than in the closed test-section case and also introduce more uncertainty [65]. Garner et al. [65] describe an analytical correction based on the method of images which replaces the airfoil with a single vortex:

$$\alpha = \alpha' - \frac{1}{2\pi}\left(\frac{L_0}{L} - 1\right) C_l' \tag{2.34}$$

$$C_d = C_d' - \frac{1}{2\pi}\left(\frac{L_0}{L} - 1\right) C_l'^2 \tag{2.35}$$

Where L_0/L is the ratio of 2D lift to total lift, which is a function of the chord-to-height ratio c/h and the aspect ratio b/c (Figure 2.10 of [65]). Brooks and Marcolini [39] have a higher order method. Instead of representing the airfoil with a single vortex, they distributed vortices along the airfoil chord. The corrections are then:

$$\alpha = \alpha' - \frac{\sqrt{3\sigma}}{\pi} C_l' - \frac{2\sigma}{\pi} C_l' - \frac{\sigma}{\pi}(4C_m') \tag{2.36}$$

$$C_d = C_d' + \left(-\frac{\sqrt{3\sigma}}{\pi} C_l'\right) C_l' \tag{2.37}$$

And σ is again the value given by Equation (2.21). The comparison of Fuglsang et al. [68] shown that both methods lead to very similar results. For symmetrical airfoils, the latter correction for the effective angle of attack can be simplified:

$$\alpha = \frac{\alpha'}{\eta} \qquad \eta = (1 + 2\sigma)^2 + \sqrt{12\sigma} \tag{2.38}$$

Note that this equations only depends on the system geometry (c/h), which makes it immediate to apply. This becomes very useful because we can define in advance the effective angles of attack of interest, instead of correcting afterwards.

In practice, sometimes the angle of attack correction is applied by comparing the measured pressure distributions at α' (measured) to the predicted C_p at α (effective). The predicted C_p is obtained either by using CFD or panel methods (e.g., XFOIL). The drawback of this method is that the measured data is forced to match with the predicted one, and the results are heavily correlated with the computations.

Aerodynamic corrections for hybrid-anechoic wind tunnels

If aerodynamic measurements are to be taken with Kevlar walls, additional considerations should be taken into account. The airfoil loading creates a pressure difference in the Kevlar membranes, which induce some flow transpiration and hence a velocity normal to the stream-wise direction [45]. The classical corrections outlined before must then be modified to account for this new velocity component. Appendix A of K. Brown Ph.D. Thesis provides the modified corrections [69].

Different approaches may be used to calculate the transpiration velocity. Fischer et al. [70] shows a comparison of different methodologies to do so for two different wind tunnels (Poul La Cour Tunnel at DTU and the Stability Wind Tunnel at Virginia Tech). Both facilities used potential flow methods to get the velocity and pressure difference on the membrane. The same formulation as for the hard-wall case is used but now source terms are introduced in the walls to represent the transpiration. In the DTU case, the velocity is calculated from the pressure difference using the Bernoulli equation corrected for the porosity of the membrane [70]:

$$v_t = \sqrt{2\Delta p / \left(\rho \left(1/(r_c r_o)^2 - 1\right)\right)} \tag{2.39}$$

In the Virginia Tech methodology, an empirical fit is used instead:

$$v_t = k_c \Delta p^{0.5} \left(\frac{\Delta p}{\Delta p + k_p}\right)^{0.073} \tag{2.40}$$

k_c, k_p, r_c and r_o depend on the membrane characteristics. Another difference between both methodologies is that Virginia Tech accounts for the membrane deformation in the potential flow calculations. Despite the slightly different corrections, the comparison of the corrected results from both facilities lead to the usual scatter present in hard-wall wind tunnels. This suggested that hybrid-anechoic wind tunnels can be reliably used for aerodynamic measurements [70].

Shear layer corrections

Up to this point we have studied the aerodynamic corrections, namely the angle of attack, force coefficients, and dynamic pressure corrections. Now we will move on to the acoustic ones, starting by the shear layer correction. We will here summarize the correction proposed by Amiet [40]. Consider the geometry of Figure 2.8.

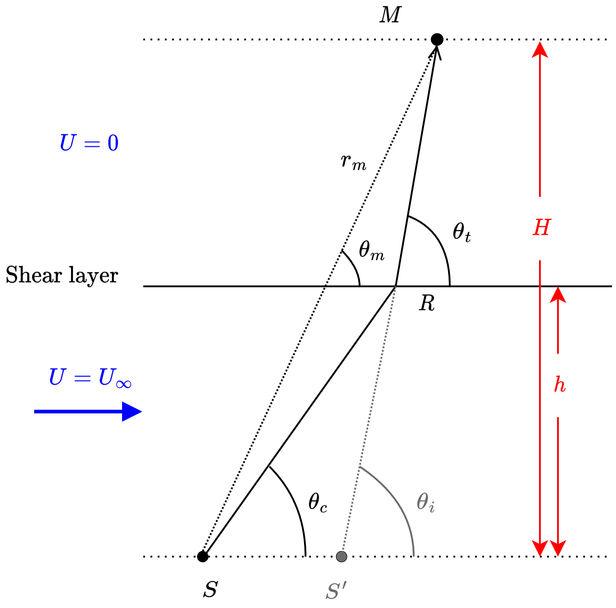

Figure 2.8: Shear layer refraction sketch. Reproduced from [40].

A source at position S is emitting acoustic waves within a flow field at velocity U_∞. A distance h separates the source to the shear layer. A microphone is placed at position M, located at geometrical distance r_m with an angle θ_m. However, the sound waves arrive at the microphone through the point R due to refraction. We want to know what is the true propagation angle θ_c to know the corrected observer distance and propagation time. We can start by working out the geometrical relations in the sketch:

$$H \cot\theta_m = h \cot\theta_c + (H - h)\cot\theta_t \tag{2.41}$$

We can get rid of θ_t by using Snell's law:

$$\frac{1}{\cos\theta_t} = \frac{1}{\cos\theta_i} + M \tag{2.42}$$

θ_i is the incident angle of the sound wave at point R. We can relate it to θ_c by considering the propagation of the acoustic wave. Point S' shows the apparent center of the spherical wave that has arrived at point R.

This wave has taken $h/(c\sin\theta_i)$ to propagate from S to R. In this time the wave center has been convected downstream a distance $hM/\sin\theta_i$. With this distance we can write:

$$h\cot\theta_c - h\cot\theta_i = hM/\sin\theta_i \tag{2.43}$$

We now have three equations (Equations (2.41) to (2.43)) with three unknowns $(\theta_i, \theta_t, \theta_c)$. These can be solved iteratively. Note the dependence on M and H/h. The magnitude of the correction as a function of these parameters may be clearly seen in Figure 10.18 of [36]. Increasing M and H/h leads to higher differences between θ_m and θ_c.

Besides the distance correction, we should also take into account the amplitude change induced by the shear layer. Two effects play a role: the loss of acoustic pressure due to the transmission, and the difference in the geometrical spreading of the waves. The same paper by Amiet [40] describes it, and the derivation is a bit more cumbersome due to the more difficult geometrical relationships. Ray-tubes should be considered to account for this geometrical spreading. The final equations for the correction are again dependent on H/h, M, and θ_m. Very small corrections should be applied for $\theta_m \approx 90$ deg and low Mach numbers. However, if the geometrical angle deviates a lot from this value (say, 45 deg), corrections up to ±5 dB should be applied. This is because the internal reflection of the acoustic waves plays a big role. Additionally, increasing the Mach number would also demand for larger corrections. This can be clearly seen in Fig 10.21 of [36].

In all these derivations an infinitely thin shear layer was considered. Amiet's paper [40] also describes the corrections for infinite thickness, and shows that they lead to similar values provided that no extreme θ_m angles are used. The curvature of the shear layer (for e.g. a circular open-jet) is also considered to expand the correction.

Kevlar walls transmission loss

The presence of the Kevlar walls in the transmission path creates an additional attenuation of the acoustic pressure. This transmission loss depends on the membrane characteristics and the flow conditions. Usually, this is corrected empirically by placing a speaker on one side of the test section (outside) and recording the measurements using a microphone in the other side, so the sound waves travel through two Kevlar walls. The sound measured by the microphone is then compared to the free-field case to give an empirical correction. Curve fits in the form described by Devenport [36, 71] are then applied. These have the following form for a given fabric characteristics:

$$\Delta_{\text{Kevlar}} = 0.0059\left(\frac{f}{1000\text{ Hz}}\right)^2 + 0.0145\left(\frac{f}{1000\text{ Hz}}\right) \tag{2.44}$$

$$\Delta_{\text{Flow}} = \left[1 - e^{-1.057(f/1000\text{ Hz})}\right]\left(5.4316M + 88.95M^2\right) \tag{2.45}$$

Where the first represents the loss without flow and the second the additional effect of the velocity. Equations are given in dB. The total correction increases with M and f.

Instead of relying in this empirical correction applied to the final spectra, a more physics-based correction was recently developed by Fischer et al. [72]. The acoustic ray procedure was employed (similarly as Amiet's correction [40]) to update the amplitude and distance corrections taking into account the Kevlar walls effect. The resulting corrections can then be applied in the calculation of the steering vectors when using beamforming (Section 2.3).

Turbulence decorrelation

The sound that we are measuring travels through a shear layer before it is measured by the multiple microphones of the array. The coherence of the signal recorded by the microphones is reduced in this process. The turbulence of the shear layer induces a variation in the time delay from the source to each microphone that depends on time and microphone position [41]. The random turbulent structures create random time delays that cannot be predicted with the acoustic ray technique used in the infinite shear layer theory [40]. The magnitude of the coherence loss increases with microphone distance, frequency, and turbulence level. This phenomena results in a reduction of the beamforming image resolution, and yields lower integrated levels

[73].

Ernst et al. [74] provided a methodology to predict this coherence loss due to the turbulent shear layer of an open-jet tunnel. They estimated the influence of the coherence loss on the measured peak levels and the effect on the resolution array. Then a coherence function was then modeled to be able to predict these losses. However, the modelling requires a lot of information on the shear layer characteristics, such as its thickness and its mean turbulent velocity, which limits its applicability without carrying out additional and expensive measurements. More recently, C. Bahr [75] used a similar methodology to integrate decorrelation effects into microphone array measurements. It still relies on a modeled coherence function that needs experimental shear layer data.

2.5. Uncertainties and limitations

Despite acoustic array methods being the state-of-the-art technique, the uncertainty of the measurements is rarely presented. Castellini and Martarelli [76] explored the effect of uncertainties in the sound speed, microphone sensitivities, microphone positions, and scan grid position. The DAS beamformer was used. However, their analysis was restricted to a 2D setup where the sources were defined with an angle instead of 3D coordinates. Moreover, it was a general acoustics study and not directly meant for aeroacoustics applications. Yardibi et al. [77] extended their study to define a general uncertainty quantification methodology for aeroacoustic beamforming. It was also based on the DAS beamformer. First-order Taylor series expansion and the Monte-Carlo method were used for the uncertainty propagation. The uncertainties of the CSM, the array calibration, the microphone location, and the room temperature were considered. The uncertainty introduced (and avoided) during the calibration procedure was also studied. The final uncertainty mostly depended on the microphone position uncertainty and the array broadband distance. Nonetheless, the study was mainly limited to simulated monopole sources and only applied to the DAS beamformer.

Even if UQ is performed for a given beamforming or deconvolution algorithm, there is some uncertainty inherent to the algorithm choice. This is more difficult to systematically quantify. Differences greater than 10 dB have been previously found depending on the choice of algorithm [78, 79]. These papers also showed that distinct implementations of the same algorithm could yield different results. There is no obvious algorithm that should be used for all the cases. In general, if the source is dominant, all of them can do the work. When that is not the case, looking at the beamforming maps may help to identify which one is working. The study of Bahr et al. [78] compares several methods and summarizes how they behave for leading and trailing-edge noise. O. Lylloff Ph.D. [46] compares three different beamformers for trailing-edge noise. Merino-Martinez et al. [43] also studied different algorithms for various sources including trailing-edge noise. There is not a consensus between these studies on which beamformer should be used for trailing-edge noise.

The modeling uncertainty introduced by the acoustic corrections is also challenging to assess. For all the corrections listed before (shear layer refraction, Kevlar walls transmission loss, and turbulence decorrelation), some assumptions are violated in actual tests (e.g. infinitely thin shear layer for [40, 72], or no background noise [75]). However, for the shear layer correction (the most important one and generally applied), the assumptions are proven to give good results [80]. All these corrections affect especially at high frequencies, since they mainly correct for the phase lag in each microphone, and thus may introduce more uncertainty in that region.

At high frequencies, trailing-edge noise measurements are sometimes also jeopardized by the low signal-to-noise ratio. Defining an adequate signal-to-noise ratio is difficult because the tunnel background noise is not the same when the model is installed as when running empty. Therefore both acoustic measurements cannot be directly compared. A possible method is to integrate the beamforming image separately for the source (trailing-edge) and the likely extraneous noise (model corners) [81]. This may provide an estimate of the SNR at high frequencies, where the resolution is good, but it is less applicable at low frequencies, where the array resolution is limited, and the sources are difficult to discern. This is a problem because usually, the peak frequency of trailing-edge noise is at relatively low frequencies (≤ 2) kHz. The use of deconvolution techniques such as Clean-SC or DAMAS may help to retrieve more accurately the level [46]. However, in the presence of another relevant source (e.g., the leading edge), all the located sources may lie outside the integration region [82].

All these possible effects and uncertainties could lead to the previously mentioned differences in the current trailing-edge noise data-sets (Chapter 1). In the following Section we will define the research objectives that hopefully will help to understand more the differences in the experimental data and ultimately improve the existing trailing-edge noise data.

3

Research objectives

The preceding sections have explained the current methodologies for trailing-edge noise measurements, as well as the limitations in the existing approaches and experimental data. Two objectives are formulated below aiming to fill some of the gaps by (1) improving the available data and (2) gaining insights on the measurement uncertainty.

1. **Study and characterisation of new measurements taken for wind tubine trailing-edge noise**.

   Given the problems with the current BANC database for trailing-edge noise, and considering the lack of applicability for wind turbine purposes, a new experimental campaign was commenced. An airfoil representative of wind turbine blades was measured in different aeroacoustic facilities under a wide range of test conditions. The details are covered in the Methodology Section. The first objective of the Thesis is to compile all the resulting data and study it. We can define a list of features to examine:

   (a) Check that the qualitative trends in each facility are the same. Study the effect of the Re_c, M, α_{eff}, forcing of the boundary layer, serration geometry, and flap angle.
   (b) Scale comparable results to the same conditions and quantify the scatter. Study collapse quality in different scenarios (e.g., different α_{eff} or serration type).
   (c) Study different scaling methods and the collapse they produce. Check if the measurement uncertainty can explain the scatter in the scaling.
   (d) Link the differences in the acoustics to the aerodynamic behavior.
   (e) Assess possible facility and processing effects.

   The ultimate goal is to establish this data set as a trailing-edge noise benchmark once the data is fully analysed and understood.

2. **Microphone location uncertainty quantification using the DAS and Clean-SC beamformers**.

   The preceding dataset will be also used to expand the knowledge on the uncertainty dependencies during the beamforming processing. A parametric study on how the microphone location uncertainty propagates will be conducted. The following will be investigated:

   (a) Beamforming algorithm effect, by comparing DAS and Clean-SC uncertainties. Do they propagate the uncertainty differently?
   (b) Velocity effect. Does the uncertainty increase with the flow speed?
   (c) Facility effect, by comparing different wind tunnels. How does the tunnel size affect the uncertainty?
   (d) Perturbation direction and correlation effect. Which errors in the microphone location should we especially avoid?

4

Methodology

In this Chapter we will explain how the data that will be presented in the Results was obtained. Firstly, the description of the experimental campaign performed by the different institutions involved is given in Section 4.1. Then, an overview of the scaling applied to the data is presented in Section 4.2. Finally, the approach used for the uncertainty quantification is described in Section 4.3.

4.1. Experimental set-up and post-processing

This Section highlights the key characteristics and differences of the models tested, the experimental set-ups, and the post-processing. A more complete description is presented in Sections II and III of Appendix B.

Model description

The airfoil under study is the NACA 63_3-018. This airfoil has been selected because it is the uncambered version of the 6 digit NACA 63 series, used in wind turbine blades [83]. It has the desired characteristics for wind turbine use such as not so high maximum lift coefficient, soft stall behavior, and low roughness sensitivity. It is symmetric, which allows to set a good baseline where the questions introduced by the loading correction do not apply. At the same time, it has similar pressure distributions to typical wind turbine airfoils when loaded [84].

Data from two different NACA 63_3-018 models have been used in this study. They have been built with different chord lengths to increase the Reynolds number range of the measurements. The small model had a chord length of 0.2 m and will be called Low Reynolds number Model (LRM). The large model (High Reynolds number Model, HRM) had a chord of 0.9m. The span of both models was modular to be able to fit and adapt to the different wind tunnels. More details about their manufacturing and characteristics may be found in [70, 81].

Both models are instrumented with surface pressure tabs. They are primarily distributed in the chord-wise direction to obtain the C_p data but also in the span-wise direction to check the two-dimensionality of the flow. The measurements have been conducted with both natural and forced boundary layer transition. The forced transition has been achieved with zig-zag strips at 5% chord from the leading edge on both sides of the model. This case allows to have a better comparability and reproducibility of the measurements.

Two serration geometries have been tested. The conventional sawtooth serrations and the so-called iron serrations [21]. The serration peak amplitude ($0.1c$) was twice the wavelength ($0.05c$). The effect of the flap angle φ (the angle between the airfoil's chordline and the the serration's chordline) was also assessed by testing the HRM at $\varphi = 4$ deg and the LRM at $\varphi = 8$ deg. Nonetheless, significant uncertainty was detected in the real value of the flap angle. Detailed measurements at DTU showed that instead of the nominal $\varphi = 0$ deg case the serrations were actually installed at a mean angle of 4.16 deg and 4.43 deg for the iron and sawtooth serrations respectively. Spanwise differences up to 3.8 deg were also measured.

Facilities description

The HRM has been tested in the Poul La Cour Tunnel (PLCT) at the Denmark Technical University (DTU), and the LRM has been studied in both the A-Tunnel at TU Delft, and the Acoustic Wind Tunnel Braunschweig (AWB) in the German Aerospace Center (DLR). The aerodynamics of the HRM have also been measured in the low-speed Wind-Tunnel Braunschweig (NWB) of the German-Dutch Wind Tunnels Foundation (DNW) and in the Low-Turbulence Tunnel (LTT) of TU Delft. A short description of each facility is now given here, emphasizing on the different aspect ratio, Re_c range, and measurement technique of each facility. More complete information is available in Section III of Appendix B. A general overview is also shown in Table 1 of Appendix B.

The Poul La Cour Wind Tunnel at DTU is a closed loop wind tunnel. It can be used in hard-wall configuration to focus on the aerodynamics, or with Kevlar walls to measure acoustics simultaneously. The acoustic data is acquired with a phased array of 84 microphones, separated 2.785 m from the model and 1.2 m from the Kevlar walls. The data was post-processed using Clean-SC and DAS. More information about the set-up and the post-processing is available in O. Lylloff's Ph.D. [46]. The HRM was tested in this facility in a Re_c range of 2 to 4 million. The aspect ratio of the model was 2.22. Boundary layer data was also acquired at $Re_c = 3 \times 10^6$ using Hot Wire Anemometry (HWA).

The A-Tunnel at TU Delft is an closed-loop open-jet anechoic vertical wind tunnel. A description of the tunnel may be found in [43], and the complete set-up of this project and the analysis of the results is available in [81]. Two outlet nozzles with different contraction ratios were used to measure with different velocities. The acoustic data was recorded with a phased array of 64 microphones. It was post-processed using DAS and integrated with the SPI method. No diagonal removal was applied. The LRM was tested in this tunnel in a Re_c range of 0.18 to 1 million. The aspect ratio of the model was 2 in this tunnel. HWA was employed to acquire boundary layer data.

The LTT at TU Delft is a closed-circuit tunnel originally used for aerodynamics. It has been recently refurbished for acoustic measurements [81], but only aerodynamic data from this tunnel has been used in this project. The HRM was tested here at $Re_c = 1 - 3 \times 10^6$. The aspect ratio of the model was 1.39 in this tunnel. Boundary layer information was extracted using Particle Image Velocimetry (PIV).

The AWB at DLR is an anechoic open-jet, closed-circuit wind tunnel. Two different measurement techniques were used for he acoustic data. A directional microphone in a 1.4 m outer diameter elliptic mirror was used simultaneously with a phased array of 96 microphones. The measurements of the latter were processed using Clean-SC. The model's aspect ratio was 4, and the Re_c range of the tests was 0.38 to 0.77 million.

The NWB at DLR is a closed-circuit wind tunnel that can be used in closed-walls or open-jet configuration. For the results presented here, only aerodynamic data from this tunnel was available. The HRM was measured at $Re_c = 1.9 - 4.8 \times 10^6$ with an aspect ratio of 3.11.

Available dataset

A summary of the test cases for the acoustic measurements is shown in Figure 4.1. The AWB and the A-Tunnel, which cover the lower part of the Reynolds number range, used the LRM, whereas the HRM was tested at DTU. The gap between models is filled in the aerodynamic measurements with the LTT data, but unfortunately there is a Re_c jump in the acoustics. There are many overlapping points in the LRM which allow direct comparison between facilities. The geometrical angles of attack were chosen such that their effective ones were equivalent (see Section 2.4, wind tunnel corrections).

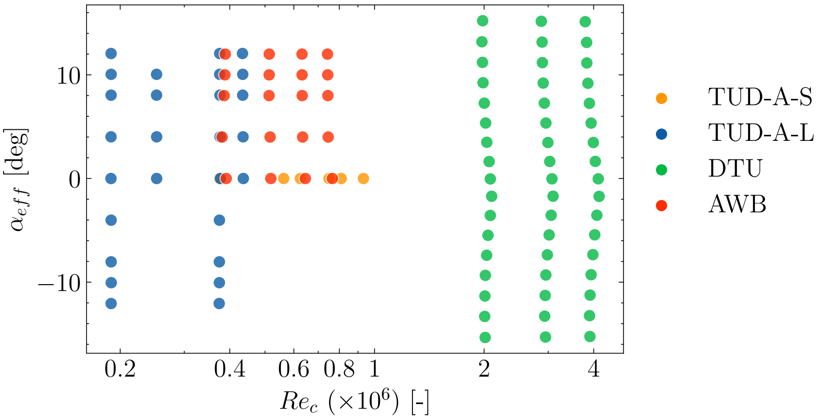

Figure 4.1: Summary of the acoustic data (straight trailing edge and tripped bounary layer).

This Thesis' author did not participate in the experimental campaigns. When the Thesis started, the results were (mostly) available. They have been compiled and put in the same format. The data has been cleaned and completed (e.g., missing environmental properties, frequency representations, and boundary layer parameters). The resulting data-set has been prepared into a convenient Python Pandas data frame that can be easily shared, compared, and analysed. After the first analysis carried out in this Thesis, the idea is to continue exploring this data and publish it as a reference database for trailing-edge within the efforts of BANC.

4.2. Scaling

The preceding Section has shown a large matrix of measurement conditions. To enable comparability between them, check trends, and be sure that we are measuring trailing edge, the measured spectra should be scaled to the same reference conditions. Finding a scaling formulation that works is very useful because it allows us to understand how noise is generated, identify key parameters, and get hints on what could be changed to lower it. The traditional way to scale trailing-edge noise comes from the analysis of Ffows Williams and Hall [55]. This is the theoretical result of turbulence convecting above a large flat plate and past the TE, and can be written as:

$$< p^2 > \propto \rho^2 v'^2 \frac{U_c^3}{c} \left(\frac{b\mathscr{L}}{r^2} \right) \bar{D} \tag{4.1}$$

$< p^2 >$ corresponds to the mean-square sound pressure measured at a distance r from the TE. ρ is the air density, v'^2 the mean-square turbulence velocity, U_c^3 is the turbulence convection velocity,and c is the speed of sound. b is the span length and $\mathscr{L}$ is a turbulence length scale. $\bar{D}$ corresponds to the directivity factor. It is then assumed that $v' \propto U_c \propto U$ and $\mathscr{L} \propto \delta$ or δ^*, which are, respectively, the boundary layer thickness and the boundary layer displacement thickness. Therefore, one can calculate the scaled spectrum using these parameters as:

$$\begin{aligned} SPL_{1/3,\text{scaled - freestream}} = & SPL - 50\log_{10}(M_U/M_{ref}) - 10\log_{10}(\delta^*_{SS}/\delta_{ref}) \\ & - 10\log_{10}(b/b_{ref}) - 20\log_{10}(r_{ref}/r) \end{aligned} \tag{4.2}$$

$$St_{\delta^*} = f\delta^*_{SS}/U \tag{4.3}$$

This is also the scaling formulation used in the BPM model [54], and it is widely used to compare acoustic results. However, as they point out in the same BPM report, a perfect collapse is not expected. The peak location is predicted to be Mach-dependent, following $St_{\delta^*,\text{peak}} = 0.02M^{-0.6}$.

The classical two-layer boundary layer theory says that an incompressible boundary layer at equilibrium is dependent on two sets of scales: inner and outer boundary layer scales [85]. When scaling the surface pressure fluctuations, two different scaling formulations are commonly used for different parts of the spectrum [31]. The outer boundary layer scales provide a better collapse in the low frequency region, and the inner boundary layer scales work better at high frequencies. Similarly, the far-field noise may be scaled using an equivalent set of parameters. The scaling formulation used in the work of Herr [31] will also be also explored here. A scaling is defined using the so-called "mixed boundary layer scales":

$$\begin{aligned} SPL_{1/3,\text{scaled - mixed scales}} = & SPL - 20\log_{10}(M_{u_e}/M_{ref}) - 30\log_{10}(M_{u_\tau}/M_{ref}) \\ & - 10\log_{10}(\delta_{99}/\delta_{ref}) - 10\log_{10}(b/b_{ref}) - 20\log_{10}(r_{ref}/r) \end{aligned} \tag{4.4}$$

$$St_{\text{mixed scales}} = f\delta_{99}/u_e \tag{4.5}$$

Where M_{u_e} is the Mach number based on the edge velocity, and M_{u_τ} is based on the wall friction velocity $u_\tau = \sqrt{\tau_w/\rho}$. The Mach number based on the eddy convection velocity M_V should be used instead of M_{u_e} (see Equation (4.1)). However, this value is not experimentally available. When not available, previous studies in the literature have taken a factor of the freestream velocity or the edge velocity [31, 86]. However, it is known that the eddy convection velocity is frequency dependent [87]. This dependency is neglected and the full edge velocity is taken instead to represent M_V. This scaling formulation is more directly related to the FWH result, and better collapse is expected especially at low frequencies due to the chosen length and velocity scales. Similarly, a scaling based on inner boundary layer scales may be formulated:

$$\begin{aligned} SPL_{1/3,\text{scaled - inner scales}} = & SPL - 20\log_{10}(M_{u_e}/M_{ref}) - 20\log_{10}(M_{u_\tau}/M_{ref}) \\ & - 10\log_{10}(\delta_{99}/\delta_{ref}) - 10\log_{10}(b/b_{ref}) - 20\log_{10}(r_{ref}/r) \end{aligned} \tag{4.6}$$

$$St_{\text{inner scales}} = f\nu/u_\tau^2 \tag{4.7}$$

The Strouhal number is now based on the viscous sublayer length and velocity scales, which should represent more accurately the boundary layer at high frequencies.

Boundary layer parameters

To be able to apply these scalings to the data, we need to obtain the necessary boundary layer parameters. The HWA measurements can be used to obtain them. The procedure is the following. Firstly, the measured velocity profiles at the TE are fitted to the logarithmic layer to obtain u_τ and the corrected wall distance from the first measurement point [88]. Using those, δ_{99} and the corresponding u_e are calculated from the region where the velocity fluctuations are constant, and then the displacement thickness is integrated [85]. This fitting method may be controversial because it involves matching the data to pre-existing results. Moreover, the fitting may be badly conditioned if not enough points are measured near the wall, which could be possible for the thin boundary layers in the LRM measurements. To check results and be confident about them, the "diagnostic plot method" [89] was also used to extract the boundary layer parameters, and very similar results were obtained.

The issue with using the measured boundary layer parameters for the scaling is that we do not have data for all the cases. To overcome this, XFOIL has been used to get quick predictions for all the conditions. The transition has been specified at the tripping position for the forced boundary layer cases. In the natural transition cases, the transition location occurs where the amplitude of the most amplified Tollmien-Schlichting wave reaches the specified n_{crit} [90]. The resultant C_p is very sensible on the transition location criteria specified. To select the appropriate value, the measured C_p distributions have been compared with XFOIl predictions at different n_{crit}. Figure 4.2 shows this comparison for the LRM measurements at $\alpha_{eff} = 0$ deg. It is observed how the selected $n_{crit} = 9$ captures well the extent of the laminar separation bubble for all the cases. This will be then the value used then for the XFOIL calculations. The same procedure has been followed to determine the n_{crit} for the HRM cases, although the higher Re_c range makes the results much less sensitive to this parameter.

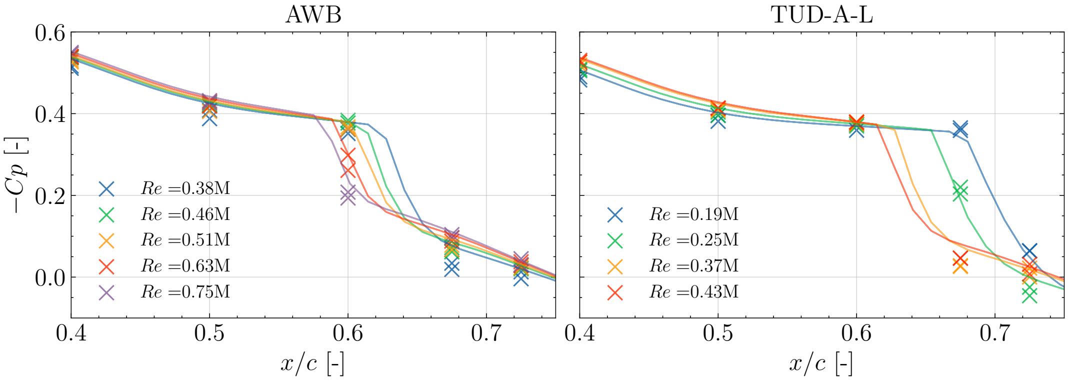

Figure 4.2: C_p measurements compared to XFOIL predictions for the LRM at $\alpha_{eff} = 0$ deg. Markers show measurements, and lines of the same color show the corresponding XFOIL prediction at $n_{crit} = 9$. Natural transition.

Since XFOIL does not provide predictions of δ_{99}, the empirical results have been used to fit the generic solution of the turbulent boundary layer thickness growth [85], given by:

$$\delta_{99,\text{ turb.}} = K_{\delta_{99}}\left\{0.29\frac{(c-x_{\text{tr.}})^{5/4}}{\left[\left(\frac{c-x_{\text{tr}}}{c}\right)\text{Re}_c\right]^{1/4}} + \delta_{99,\text{ lam.}}^{5/4}\right\}^{4/5} \tag{4.8}$$

Where $\delta_{99,\text{ lam.}} = 5x_{\text{tr}}/\sqrt{Re_{x_{\text{tr}}}}$ is the Blasius solution for the laminar boundary layer, x_{tr} is transition location measured from the leading edge, and $K_{\delta_{99}}$ is an empirical factor to account for the pressure gradient. It is different in the natural and forced transition cases, and has been determined by fitting the measured δ_{99} to these expressions. This is analogous to the methodology in [81].

4.3. Uncertainty quantification

The NACA 63_3-018 data-set has been used to get more insights about the effect of microphone location uncertainty. The procedure proposed by Yardibi et al. [77] has been followed. In their study, two different methodologies were used. Linear Taylor-series expansion and the Monte-Carlo method. The latter is more flexible and it can be directly applied to different beamforming algorithms. The former is not, since the Jacobian matrix of, say, the power estimated by the Clean-SC algorithm cannot be determined analytically. Since the analysis will be applied also to Clean-SC, Monte-Carlo method will be used. A theoretical introduction of the method is given in Appendix A. Despite its low convergence rate, it does not suffer from the "curse of dimensionality", which makes it suitable for this application because the number of inputs will be considerably large.

The assumed input probability distribution will be normal distributions centered at the nominal location of the microphones. Two cases will be considered. On one hand, the *uncorrelated* case will mean that the perturbations have been generated individually for each microphone and each direction. On the other hand, the *correlated* case will refer to the global perturbation of the array. In the latter case, the three directions will still be independent. From these input probability distributions, samples will be drawn, the beamforming process will be carried out with the perturbed locations, and the probability distribution of the outputs will be analised.

To propagate the uncertainty, the beamforming process will be applied taking into account the perturbed microphone locations. This means that new steering vectors will be calculated for each sample according to the new distances between the microphones and the scan grid. The CSM will be kept the same. Alternatively, we could modify the phases of the CSM according to the perturbed distances and keep the same steering vectors. However, the first procedure will be followed to avoid the re-calculation of the CSM and be aligned with Yardibi's methodology. When the DAS beamformer is used, the final source power will be integrated using SPI. In that case, the PSF for the scaling of the power will also be calculated using the perturbed microphone locations.

For the beamforming computations, the library AeroAcoustics.jl[1] was used. This is the same code the DTU data was initially post-processed with. Since we will study also the A-Tunnel data, a previous comparison of beamforming codes was carried out. The A-Tunnel measurements were adapted to this new format until both codes lead to the same output (<0.4 dB error).

The number of samples to use in the calculation depends on the acceptable error of the results. A study has been carried out using the data from the A-Tunnel at 45 m/s. The microphone locations have been perturbed in the three directions with i.i.d. normal distributions with $\sigma_{loc} = 10$ mm. Different number of (uncorrelated) samples have been used, and the convergence of the integrated SPL is assessed. In Figure 4.3 the difference between i and $i+1$ samples is shown. As the number of samples increases, the difference gets progressively lower, which indicates a converging result. For the purposes of this study, differences within 0.1 dB can be assumed to be converged. Therefore, $N = 256$ is selected for the subsequent sections. Note that the Figure presented was not the only convergence case tested. Every time this is run the perturbations are different and the plots are slightly changed. In general, the trend showed acceptable agreement with the expected $1/\sqrt{N}$. Overall, it was found that $N = 256$ was constantly sufficient to meet the mentioned criteria for both the mean and the standard deviation.

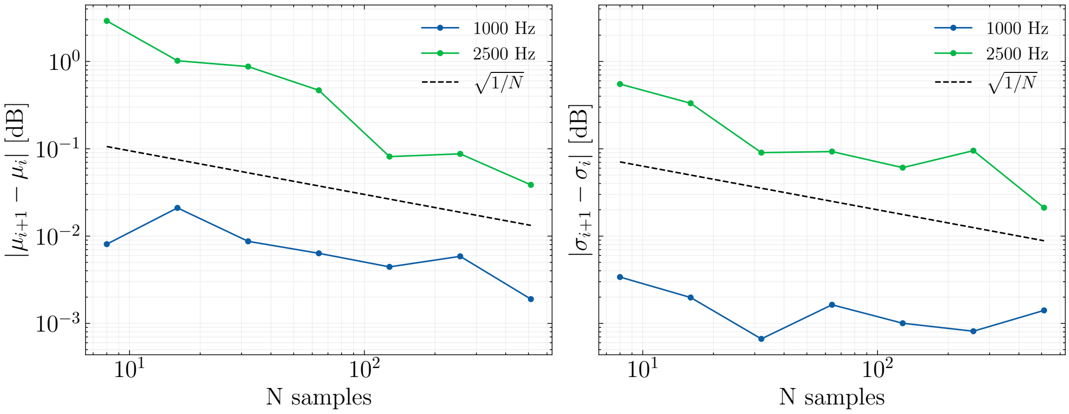

Figure 4.3: Monte-Carlo convergence study. The difference between consecutive number of samples is presented for both the mean and the standard deviation. Tested from $N = 8$ to $N = 1024$ in power of two intervals.

It is also interesting to check the probability distribution of the output. The distribution at two different frequencies is shown in Figure 4.4. The A-Tunnel data at 45 m/s has been used again with an uncorrelated input uncertainty of $\sigma_{loc} = 10$ mm. It is considered that the fitted normal distribution is a good representation of the histogram, and matches well with the kernel density estimate (KDE) of the data. Therefore, the output of the process will be characterised in the results by using the statistical moments μ and σ. For a more accurate characterisation, however, we could also use a higher-order PDF that included the skewness (slightly visible in the right plot of Figure 4.3).

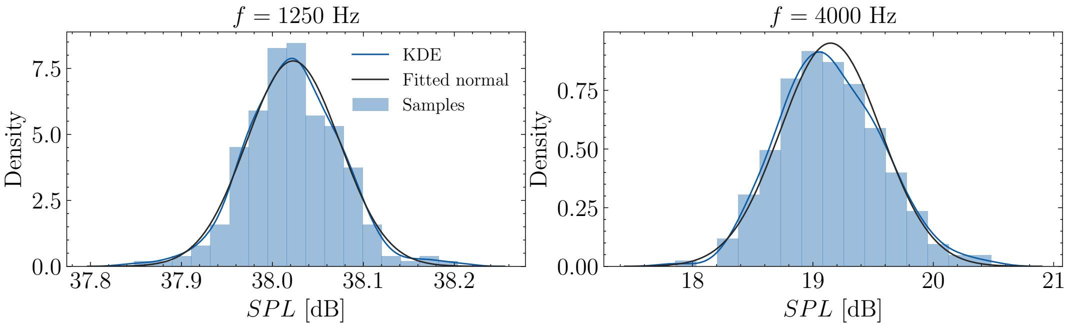

Figure 4.4: SPL output distribution after Monte-Carlo propagation. 256 samples have been used to propagate an uncorrelated input uncertainty of $\sigma_{loc} = 10$ mm. A-Tunnel data has been used at 45 m/s, and DAS with SPI have been applied.

---

[1] `https://github.com/1oly/AeroAcoustics.jl`, written in Julia and maintained by Oliver Lylloff (DTU).

5

Results and discussion

In this Chapter the measurements from the different wind tunnels are studied. Section 5.1 presents the cross-facility comparison of the NACA 63_3-018 results. The aerodynamics and acoustics are compared. The trends are identified, the differences between facilities are explained when possible, and results that need further investigation are highlighted. A grade of disagreement is observed in the A-Tunnel results, and this is tackled in Section 5.2, where the possible effects of the post-processing are investigated. Finally, the uncertainty introduced by the microphones locations is explored in detail in Section 5.3. The dependencies with the position error correlation, flow velocity, and beamforming method are studied.

5.1. Benchmark testing results

This Section provides an overview of the cross-facility measurements carried out for the NACA 63_3-018. The aerodynamic and aeroacoustic characterisation are detailed in Appendix B. A summary of the main take-aways is given here, and the information from the paper is extended with more analyses that further help to understand the data. A recommendation to the reader is to go first trough the paper and then come back to this Section to expand on the exploration of the data.

5.1.1. Aerodynamic results

The aerodynamics are firstly compared looking at the polar curves. Figure 8 of Appendix B shows the lift coefficient for each facility at different Re_c for both natural and forced transition. The drag coefficient is compared in Figure 9. Tripping the boundary layer leads to lower $C_{l,max}$, higher C_d and lower Re_c sensitivity in the separation region. Good agreement between facilities is observed, and differences are attributed to the distinct aspect ratio of the tunnels. After checking that the baseline aerodynamic results are consistent and according to the expectations, the effect of the different wind tunnel set-ups is assessed in Figure 10. The LTT and the DTU aerodynamic results with Kevlar walls and hard walls are presented, and good agreement is found.

Apart from comparing the lift curves, it is also useful to check if there are differences in the C_p, and whether the airfoil behaves as expected. It is interesting to note that laminar separation bubbles were found in the natural transition case for the LRM. Figures 5.1 to 5.3, show the C_p for the A-Tunnel and the AWB at α_{eff} = 0, 4, and 8 deg respectively. The data is presented at $Re_c = 0.38 \times 10^6$. Comparing both facilities we see good agreement in most of the pressure probes, with a bit of mismatch in the tripping location. But the key are the natural transition results. At $\alpha_{eff} = 0$ deg, a separation bubble is observed from $x/c \approx 0.45$ to $x/c \approx 0.65$. When increasing the angle of attack to 4 deg, the bubble in the suction side moves towards the leading edge, and the bubble in the pressure side approaches the trailing edge. At 8 deg this is even more pronounced, and the laminar separation bubble of the pressure side is located at $x/c = 0.8$. However, the resolution of the pressure probes is not enough near the TE due to the small size of the model, and the separation bubble is only visible in the XFOIL results. The observation of the laminar separation bubble is relevant because it will influence the acoustic results: it enables the presence of laminar boundary layer - feedback loop tonal noise. When the boundary layer transition is forced, this phenomena is completely removed.

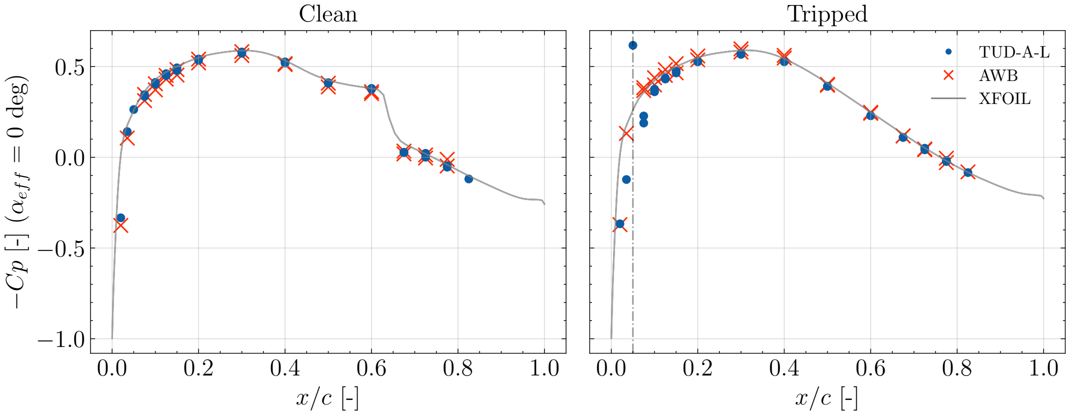

Figure 5.1: Pressure coefficients for the LRM at $\alpha_{eff} = 0$ deg. $Re_c = 0.38 \times 10^6$ and straight trailing edge.

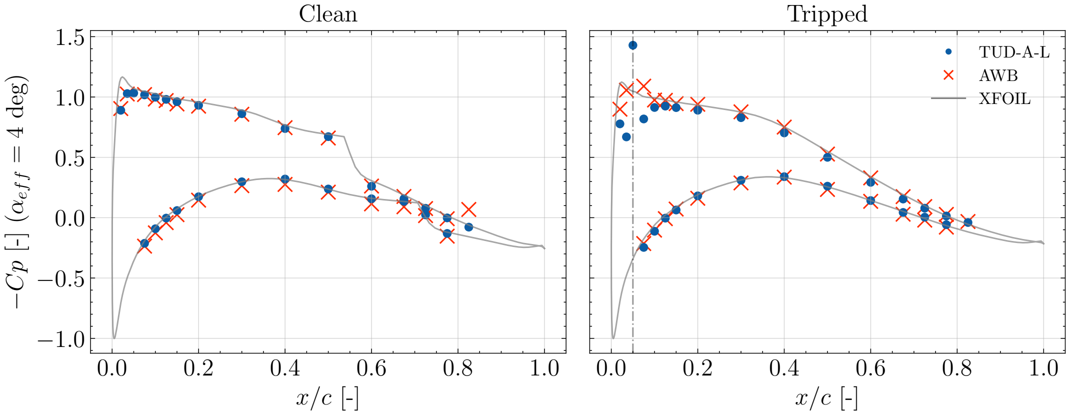

Figure 5.2: Pressure coefficients for the LRM at $\alpha_{eff} = 4$ deg. $Re_c = 0.38 \times 10^6$ and straight trailing edge.

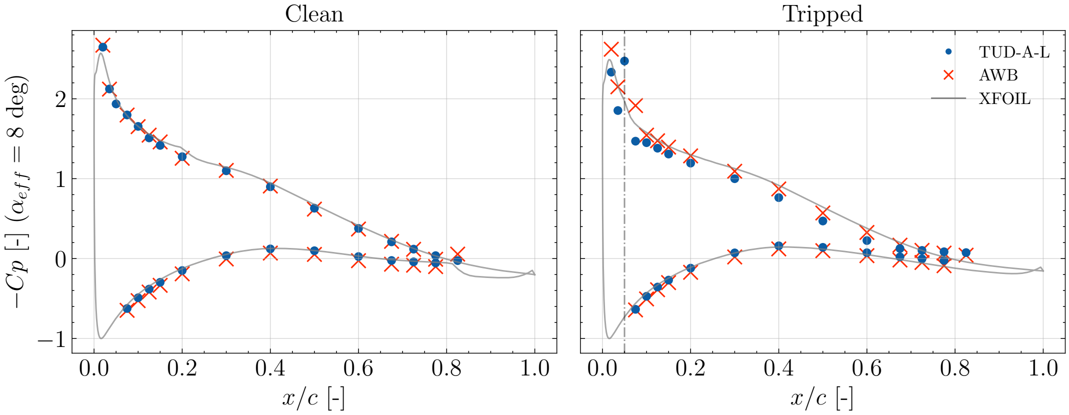

Figure 5.3: Pressure coefficients for the LRM at $\alpha_{eff} = 8$ deg. $Re_c = 0.38 \times 10^6$ and straight trailing edge.

So far everything is consistent with the expectations and shows reliable results between facilities. Next step is to introduce the serrations and check how the lift coefficient varies. This is shown in Figure 11 of Appendix B. Since the lift is calculated based on the same chord length, but the serrations are increasing it, the C_l with serrations is higher. Comparing the two serration geometries (sawtooth and iron), the increase in lift appears to be higher for the iron ones. This is associated to a larger surface area. The effect of the flap angle is also visible: DTU measurements were conducted at a flap angle higher than the nominal (around 4 deg instead of 0 deg). This creates an additional chamber that increases ΔC_l about 0.08 to 0.12 with respect to the straight serrations. The different slope in the iron and sawtooth geometries is also observed in the flapped case.

Besides checking the forces on the airfoil, it is necessary to study the velocity profiles in the vicinity of the trailing edge. This is especially important for the calculation of the displacement thickness δ^*, since it will be widely used for scaling the acoustic results (Section 4.2). It is the parameter used to represent the different turbulent length scales of the measurements. The measured δ^* are presented in Figure 12 of Appendix B and compared with XFOIL predictions. Good agreement is found at the high end of the Reynolds range. However, discrepancies are found in the LRM results. Those are attributed to lower measurement resolution due to a very thin boundary layer. XFOIL captures well the general trends with respect to Re_c and tripping. To elaborate a bit more on the results, the uncertainty of the measurements was calculated and is presented in Figure 5.4. The uncertainty was calculated using Monte-Carlo propagation and perturbing the velocity profiles with the calibration error. The uncertainty of the results is not enough to justify the deviations from XFOIL or the scatter between the two points at $Re_c = 0.4 \times 10^6$. The next hypothesis is that the difference is due to the lack of resolution in the thin boundary layer. Not enough points make for a bad fitting to find the distance between the first probe position and the wall. Additionally, the measurements may be contaminated by the heat transfer at the positions closer to the wall.

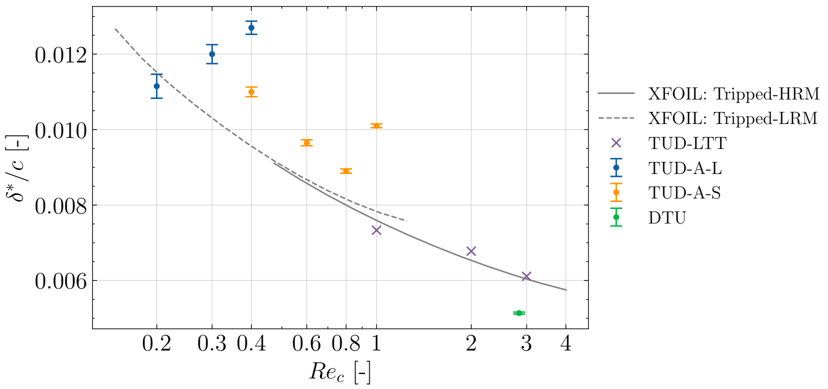

Figure 5.4: δ^* measurements including the HWA uncertainty.

5.1.2. Aeroacoustic results with straight trailing edge

After comparing the aerodynamic results, the next task is to analyze the acoustic measurements. Firstly, the far-field spectra for each facility is presented in Figure 14 of Appendix B for different Re_c and both the tripped and clean cases. The same trends are found: forcing the transition creates a thicker boundary layer (as seen in the δ^* plot), which changes the noise spectrum increasing the level at low frequencies. Increasing the velocity leads to more extent of the spectrum being affected by this increase. The velocity also increases the ΔSPL with respect to the clean measurements. Besides the normal trailing-edge noise characteristics, a high-frequency hump is also observed in some cases (AWB with elliptic mirror and DTU at Re_c = 2M and 3M). It corresponds to vortex shedding due to the trailing-edge bluntness, and it is only found in the measurements that have covered sufficiently high $St_{t_{TE}}$. We can confirm that it corresponds to vortex shedding because the peaks collapse to the same $St_{t_{TE}}$.

The effect of the angle of attack is also very related to the boundary layer thickness. Figure 17 of Appendix B shows the far-field spectra for each facility at different angles of attack. Increasing α_{eff} leads to a thicker boundary layer on the suction side and a thinner boundary layer on the pressure side. In the acoustic results, this is translated to higher levels at low frequencies (due to the suction side effect) and higher levels at very high frequencies (due to the pressure side effect). The level increase is directly related to the part of the spectrum where the turbulent boundary layer contains more energy. Another effect of the angle of attack is the presence of tones at low frequencies in the clean cases. The results in the paper's Figure 17 are presented in 1/3 octave bands, which is not the best representation because the nature of those peaks is tonal. They can better be seen in Figure 19, where the far-field noise PSD is compared between the A-Tunnel and the AWB at $\alpha_{eff} = 8$ deg. Good agreement in the location and magnitude of the peaks is observed. The small deviations may be attributed to differences in the dynamic pressure (tones may follow a ladder-type dependence on U [91]), the different aspect ratio (trough the different transition development enhanced by 3D effects), or the effective angle of attack (at high loading the correction uncertainty may increase).

We have seen that the acoustic results follow the expected trends with the angle of attack, the wind tunnel velocity, and the tripping. This gives us confidence that we are actually measuring trailing-edge noise and not something else. We can now compare all the results together and check whether they follow the expected scaling trends. We will now apply the scaling formulation described in Section 4.2. Let's start with the classic BPM scaling. The baseline scenario for the comparison is the case with tripped boundary layer (to ensure the same transition location and a turbulent boundary layer at the trailing-edge) at $\alpha_{eff} = 0$ deg (to avoid correction uncertainties). The comparison of the scaled results for this case is presented in Figure 20 of Appendix B. Good agreement is found between AWB and DTU despite deviations in the spectral slope. The A-Tunnel measurements agree in the levels with the other facilities but show a very pronounced pattern in the $St_{\delta^*_{SS}}$ axis: the curves move to the left as U increases. The reason for the mismatch should be investigated further. In Section 5.2 the processing of the A-Tunnel is analysed to rule out possible sources of deviations. Figure 21 and 22 of Appendix B show the scaling at $\alpha_{eff} = 3-4$ deg and 7-8 deg respectively. The same observations can be drawn for the $\alpha_{eff} = 3-4$ deg case: good agreement in the peak level and location, deviations in the slope, and the A-Tunnel showing a pronounced dependence on U. For the cases at $\alpha_{eff} = 7-8$ deg, there is a clear mismatch between the HRM and the LRM. The aerodynamics were already different at this angle of attack, so this difference was expected.

The preceding comparisons were conducted by using the classical BPM scaling. In Section 4.2 we saw that other scaling formulations may provide better agreement in certain frequency ranges. Figure 5.5 shows the comparison of the results scaled using Equations (4.4) and (4.5). The agreement in the peak levels is slightly better, but the A-Tunnel still exhibits a very pronounced trend with M_U. Still, it shows that this set of parameters may be a better representation of the physics at low frequencies. It could still be improved by using a frequency-dependent eddy convection Mach number M_V instead of the constant M_{u_e}. The scaling based on inner boundary layer scales is tested in Figure 5.6. We expected better collapse at high frequencies, but this is not observed. It is possible that the range of frequencies corresponding to these scales was not measured. In the study of Herr [31], where this scaling worked at high $f\nu/u_\tau^2$ values, all measurements were taken up to 20 kHz.

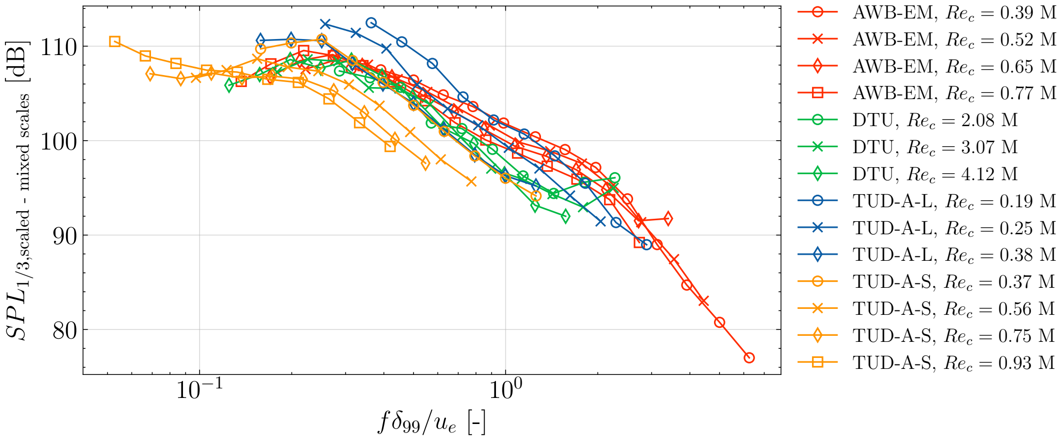

Figure 5.5: Comparison of the acoustic measurements using mixed boundary layer scales for the scaling. Forced boundary layer and $\alpha_{eff} = 0$ deg.

We have assessed the collapse quality of different scaling formulations. However, XFOIL has still been used to get the boundary layer parameters used to compute those. We needed to use XFOIL because the boundary layer profiles have not been measured for all the acoustic cases. But we can still check whether using the measured boundary layer parameters instead of the XFOIL ones leads to a better collapse quality. This is shown in Figure 5.7, where the scaling with free-stream quantities (Equations (4.2) and (4.3)) is presented using the measured δ^*. The measurement uncertainties of δ^* and U have been included in the scaling. We assess whether the uncertainty of the parameters used for the scaling may explain the scatter in the spectra. It is clear that it is not the case, and the differences are caused by something else. The collapse quality is very similar to that found using the XFOIL quantities (Figure 20 of Appendix B). The deviations seen in the

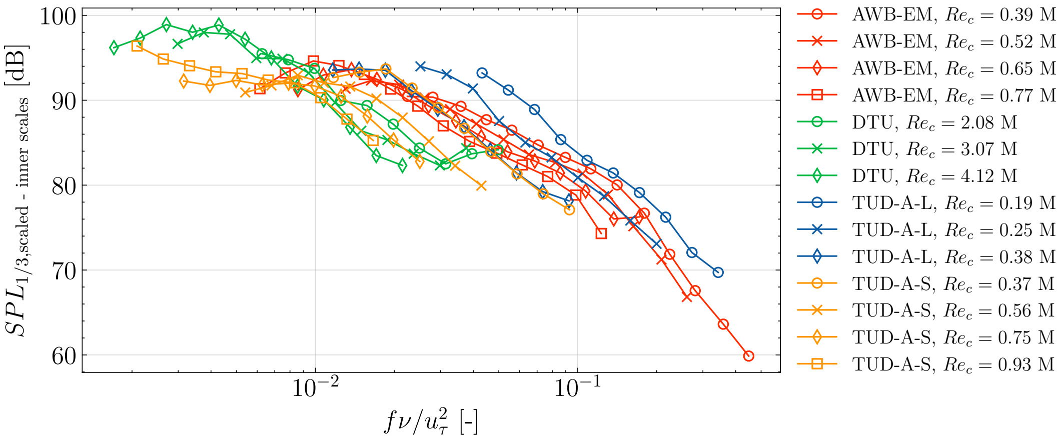

Figure 5.6: Comparison of the acoustic measurements using inner boundary layer scales for the scaling. Forced boundary layer and $\alpha_{eff} = 0$ deg.

measured and the predicted δ^* (Figure 5.4) have very limited effect on the scaled results. It justifies the use of XFOIL to extend the scaling to all the cases.

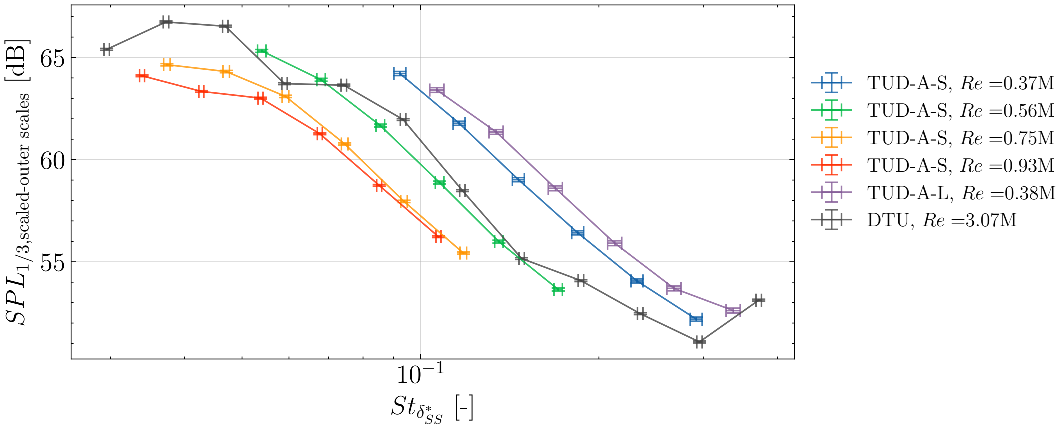

Figure 5.7: Comparison of the acoustic measurements using measured outer boundary layer scales for the scaling. Forced boundary layer and $\alpha_{eff} = 0$ deg. Error bars in both axes show uncertainty introduced by the measured δ^* and U.

5.1.3. Noise reduction effect of the serrations

After comparing the acoustic results with straight trailing edge, we can now assess the noise reduction effect of the serrations under different conditions. Section VI of Appendix B presents and explains the noise reduction effect $\Delta SPL_{1/3} = SPL_{1/3} - SPL_{1/3,ref}$ measured for each serration geometry and facility at different Re_c. The trends with U, α_{eff} and serration geometry are discussed there. The main takeaways are summarised now. Two regions of noise reduction are generally found when scaling the results with St^*_δ. Good collapse is observed between different facilities and Re_c. The agreement is actually better than before when we compared the absolute levels. This is meaningful because when we test airfoils with serrations we are usually more interested in the ΔSPL rather than the absolute levels. Finding reliable and consistent results across facility is then helpful to identify good noise reduction concepts. Regarding the different serration geometries, the iron serrations are found to provide an additional noise reduction compared to the sawtooth ones at $\alpha_{eff} = 0$ deg.

When the airfoil has non-zero loading, the resulting pressure difference in the trailing edge creates counter-rotating streamwise-oriented vortices in the serration edges. These structures create additional noise and hence diminish the effective noise reduction achieved by the serrations [17, 18]. This is seen in the $\alpha_{eff} = 0$ case when comparing the straight and the flapped serrations. The serrations with $\varphi \neq 0$ are actually cambered, and as we saw in the ΔC_l curves they are loaded even at $\alpha_{eff} = 0$. This is translated into a lower noise reduction effect compared to the $\varphi = 0$ case. The same phenomena explains the behavior with the angle of attack. The reduction in Overall Sound Pressure Level ($OSPL$) against α_{eff} is shown and discussed in Figure 25 of Appendix B. However, for practical wind turbine applications it is more useful to assess the noise reduction against the lift coefficient. This is a parameter more directly related to the blade design [92]. The $\Delta OSPL$ as a function of C_l is presented in Figure 5.8. We see that the iron serrations indeed provide the best noise reduction when the airfoil is not highly loaded. However, when it is placed at a typical operational point, relatively close to $C_{l,max}$, this advantage is lost, and the noise reduction by the different serration geometries and flap angles is similar.

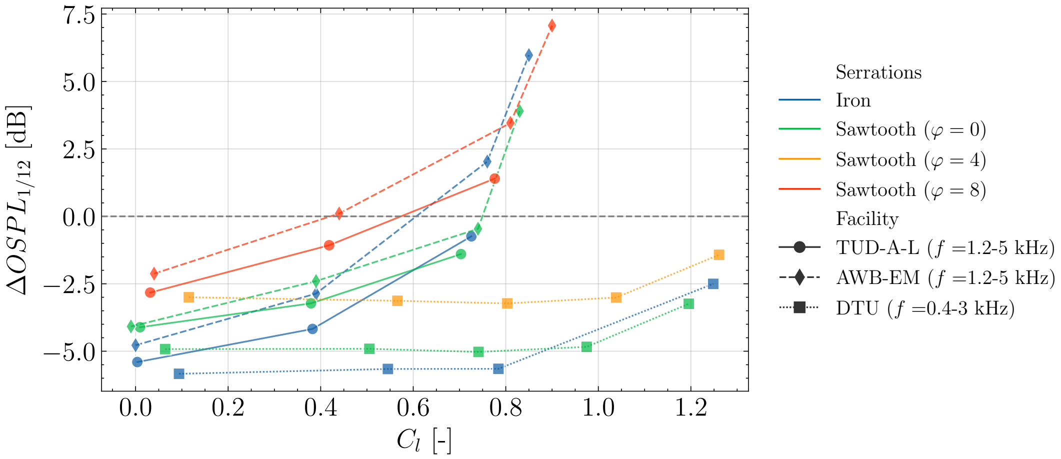

Figure 5.8: $\Delta OSPL$ as a function of C_l and serration type for different facilities. LRM data measured at $Re_c = 0.38 \times 10^6$, and HRM ata $Re_c = 3 \times 10^6$. Tripped configuration. Frequency range for the calculation of $OSPL$ is indicated in the facility legend.

Besides the reduction in trailing-edge noise, it is also interesting to note that serrations may help to eliminate the laminar boundary layer - feedback loop tones. In Figure 5.9 this effect is observed by plotting the AWB results in the baseline configurations compared to the sawtooth cases. This is consistent with the literature [20], and it is attributed to bypass transition near the trailing edge that prevents the formation of a small laminar separation bubble in the pressure side, effectively removing the amplifier of the Tollmien-Schlichting waves.

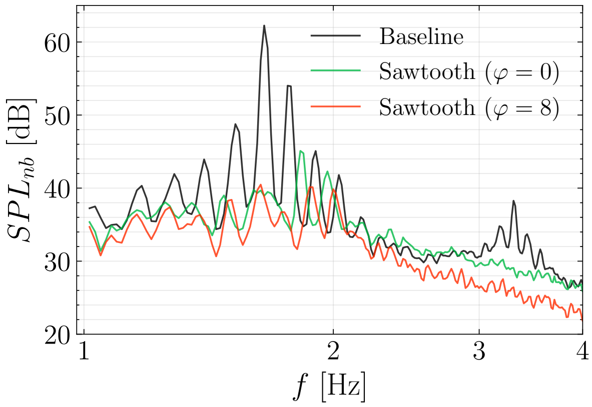

Figure 5.9: Narrow band spectra measured the AWB at $\alpha_{eff} = 8$ deg with serrations compared to the baseline case. $Re_c = 0.38 \times 10^6$. Natural boundary layer transition.

5.2. Post-processing study

5.2.1. Clean-SC and CSM diagonal removal

The beamforming technique used to post-process the results may introduce significant differences. For the DTU measurements, this was investigated in Oliver Lylloff's PhD [46]. DAMAS, Clean-SC, and DAS were used to post-process the same data. Very similar results were obtained with the three methods, but DAS seemed to overestimate the source power compared to the other two, especially at low frequencies. DAMAS and Clean-SC were better at isolating the noise from the TE. However, when another dominating source was present (e.g. pitot tube noise at a particular frequency), DAMAS failed to resolve well both sources.

A similar comparison is now presented for the A-Tunnel results. The A-Tunnel data in the preceding Section was post-processed with DAS. However, it was compared to data treated with Clean-SC. The AWB results were measured with elliptic mirror, but they were overlapped with the simultaneous microphone array data processed with Clean-SC. Then, we should investigate whether the differences observed in the scaled results were caused by the different beamforming method.

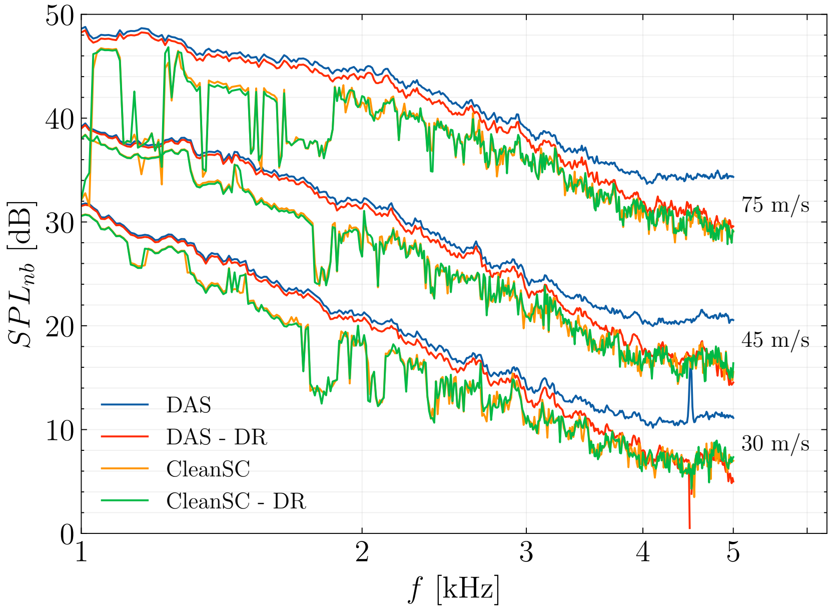

Figure 5.10: Beamforming method comparison for the A-Tunnel results. Clean-SC and DAS including or not diagonal removal.

Figure 5.10 presents a comparison between Clean-SC and DAS (with and without CSM diagonal removal) for the case at $\alpha_{eff} = 0$ deg, tripped boundary layer, and no serrations installed. Three different velocities are studied. Firstly we can check the effect of removing the diagonal of the CSM. Whereas it has little effect for Clean-SC, in the DAS results it leads to a level reduction up to 5 dB at high frequencies. However, it has no effect at low frequencies. The results with diagonal removal will be considered from now onwards. It helps to eliminate the incoherent background noise, which is mostly present in the auto-power spectral density components of the CSM, as explained in Section 2.3. This effect can be seen very clearly in the beamforming images shown in Figure 5.11. The same cases are shown with and without diagonal removal. It clearly helps to isolate the noise coming from the model. At 4000 Hz, unlike the plots at 2000 Hz, the background noise removal affects the results within the integration region, which shows why the effect on the integrated spectrum only appears at high frequencies.

Secondly we can compare the Clean-SC and DAS results. A good match is observed at high frequencies (3-5 kHz). In this region DAS does a good job in identifying the sources and therefore the use of Clean-SC is not necessary to discern accurately the origin of the noise. However, at low frequencies there is an offset between both methods. Clean-SC leads to levels 1 to 2 dB lower than the DAS case. At low frequencies, the DAS resolution is not good enough to isolate the TE noise, and additional contributions from the side-plates are introduced. The results with Clean-SC present nonphysical troughs at frequencies. These appear because no dominant sources are found within the integration region. At low frequencies it is more difficult to localise accurately. Different loop gains and number of iterations were tested to get rid of these phenomena, without success. The stopping criteria of the Clean-SC implementation in AeroAcoustics.jl is suspected as the source of this problem. Disregarding these troughs, the Clean-SC results show the same difference as in the DTU study [46]: little to no effect at high frequencies and slight level reduction at low frequencies. This does not explain the differences observed in the cross-facility comparison, but allows us to disregard this hypothesis.

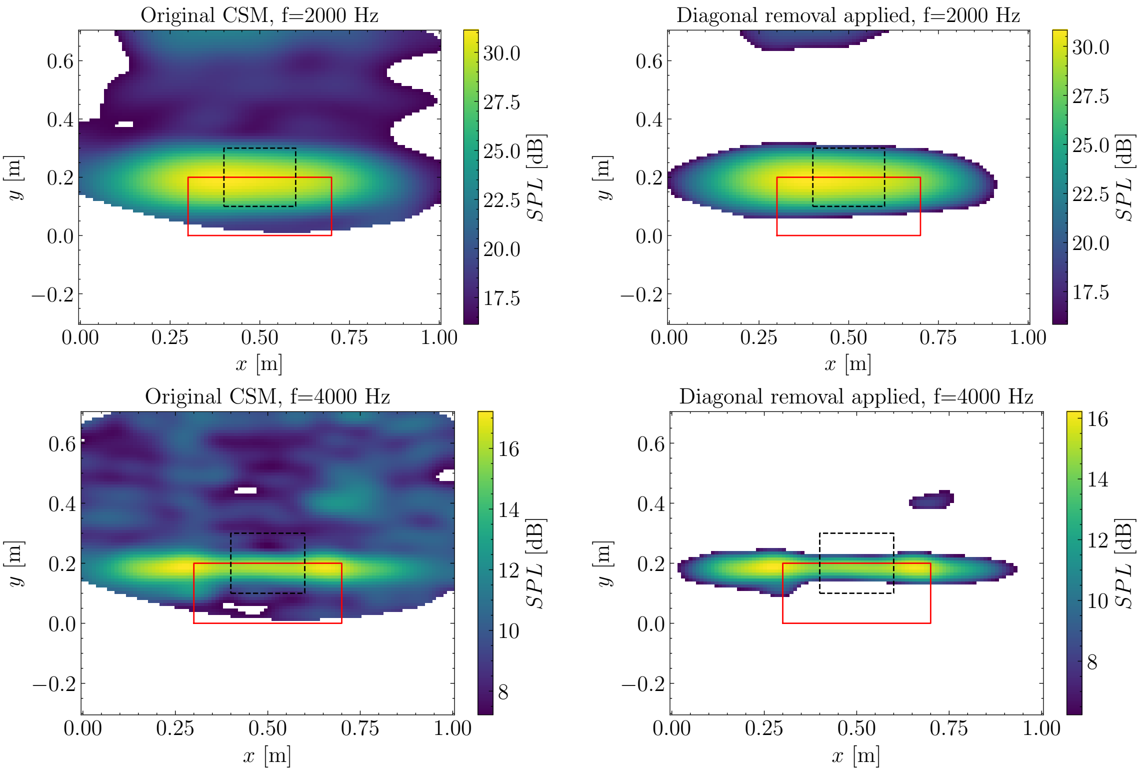

Figure 5.11: Diagonal removal effect on the beamforming images. A-Tunnel measurements at 45 m/s, no serrations, $\alpha_{eff} = 0$ deg and tripped boundary layer. DAS beamformer employed.

Additionally, the Sijtsma's approximation for the shear layer correction [50] was used in the A-Tunnel instead of the usual Amiet correction [40]. However, the measurement conditions were under the region where Sijtsma's approximation can be used, and a comparison of both methods yielded similar results. This is then disregarded as a discrepancy source too.

5.2.2. Shear layer position

Another approximation that can raise questions is the use of straight shear layer assumption. The jet of the tunnel interacts with the still air in the anechoic chamber creating a shear layer that expands and thickens as it moves downstream from the nozzle. Usually this shear layer is assumed infinitely thin with regards to the shear layer refraction correction [40]. The position of the shear layer can however be important. The correction depends on the ratio h/H, with h being the distance source-shear layer, and H being the distance source-observer (Section 2.4) [36]. The geometry of the A-Tunnel is shown in Figure 5.12a. Two black dashed lines show the assumed location of the shear layers: two straight lines (planes, in 3D) from the nozzle lips. The blue dashed lines show a possible location of the shear layer accounting for the jet expansion. A rough estimate of the possible growth could be obtained by looking at the self-similar profile of a jet [93]. The plane jet growth calculated with self-similar laws would shows a difference of 30% with respect to the straight shear layer case. To be more conservative and check the effect of an even larger error, the post-processing has been repeated doubling the distance from the model to the shear layer. This is $h_2 = 2h_1$ where $h_1 = 1.25/2c = 0.125$ m. The comparison with the original results is shown in Figure 5.12b for three velocities. The difference is negligible, and thus we could conclude that the assumption holds. However, we have still assumed that the shear layer is parallel to the array. Only the position has been changed. To be sure about the accuracy of the approximation, we would need to consider the angle of the shear layer with respect to the array.

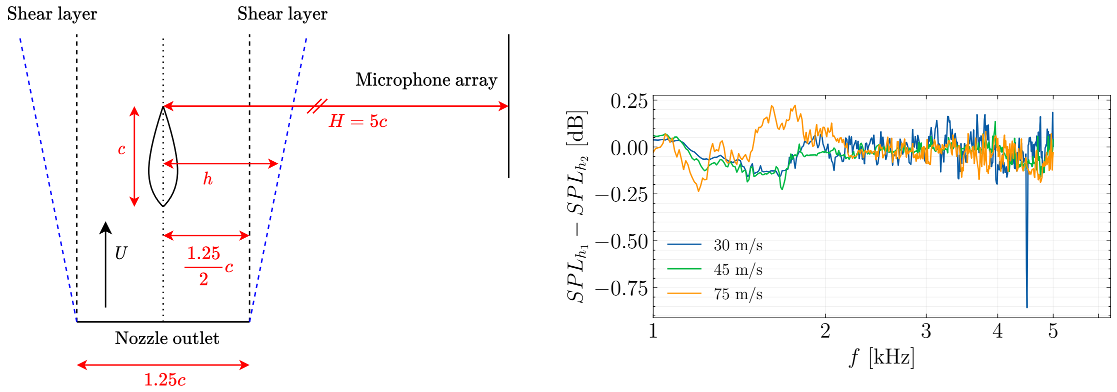

(a) Sketch of the A-Tunnel geometry (not at scale).

(b) Shear layer distance effect on the integrated spectrum. $h_1 = 1.25/2c = 0.125$ m, $h_2 = 2h_1 = 0.25$ m.

Figure 5.12: A-Tunnel geometry sketch and shear layer distance effect on the integrated spectra.

5.2.3. Coherence

The microphone coherence has been calculated for the AWB and the A-Tunnel to assess whether it may introduce a difference between their results. No coherence loss was applied to neither of the facilities, so we should check if it can affect the final spectra. The possible consequences of the signal coherence loss were presented in Section 2.4. The coherence between the signals x and y is:

$$\gamma_{xy} = \sqrt{\frac{|S_{xy}|^2}{S_{xx}S_{yy}}} \tag{5.1}$$

Where S_{xy} is the cross-power spectral density, and S_{xx} and S_{yy} are the auto-powers. These are given by Equation (2.4). The coherence loss between each microphone pair is presented for the A-Tunnel in Figure 5.13 and for the AWB in Figure 5.14. The loss is calculated with respect to the lowest velocity case (30 m/s).

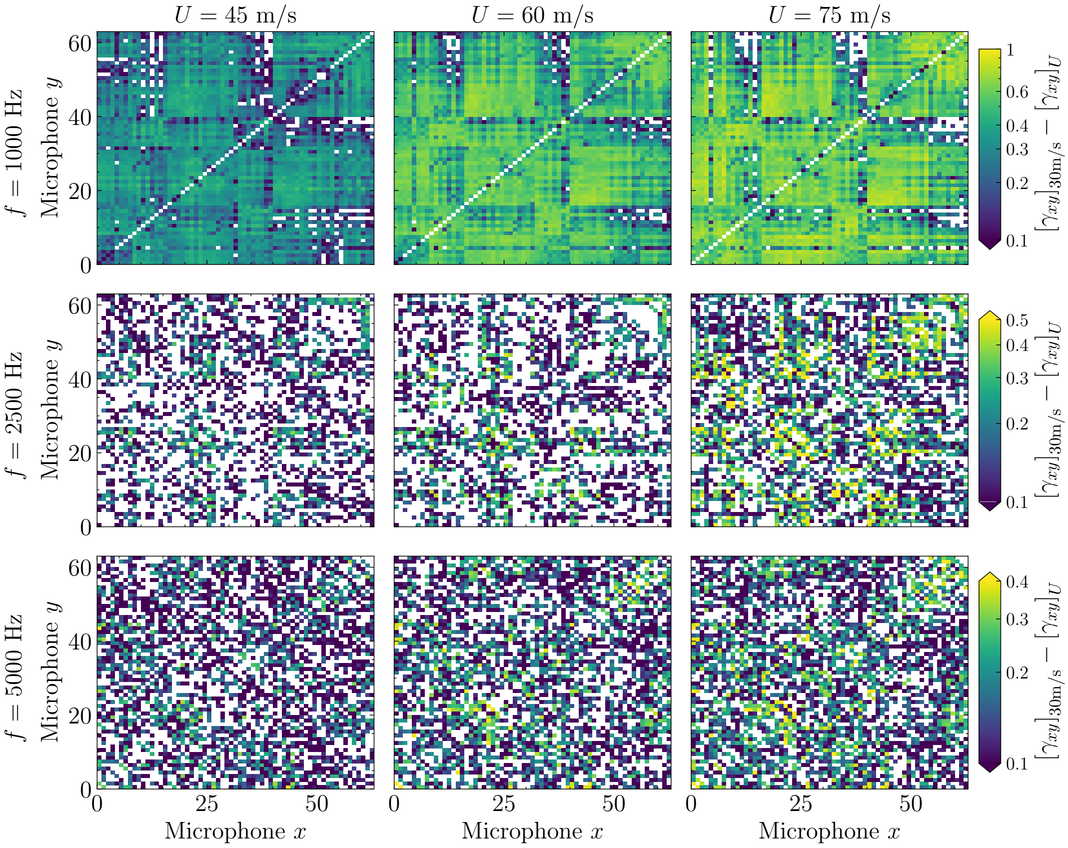

Figure 5.13: Coherence loss in the A-Tunnel. x and y refer only to the microphone index, and are not related to the physical position of the microphone in the array.

Figure 5.13 and Figure 5.14 show some differences. Note that the scale of the plots is different for each frequency, but it is the same for the two facilities. To check the absolute coherence values, Figure D.1 and Figure D.2 may be consulted. The general trends expected are observed in both facilities: the coherence decreases with the flow speed and frequency. Looking at the individual microphone positions we could also see that the coherence decreases with the microphone distance (not shown). However, the effect of the velocity is more noticeable in the A-Tunnel. Note, for instance, the case at $U = 60$ m/s, a velocity shared by both facilities. The argument posed here is the following: the coherence in the A-Tunnel seems to be more velocity-dependent than in the AWB, and hence it could be that for increasing velocity the levels are increasingly under-predicted. In the AWB the coherence loss does not change that much with velocity, and thus the possible under-prediction of the levels would affect more equally all the measurements. Neither of the facilities applied a coherence loss level correction in the final spectra. At this point, we can take a look again at Figure 20 from Appendix B, where the scaled measurements from both facilities are compared. We saw that the levels at high velocities from the A-Tunnel are lower compared to the AWB and DTU, which collapse well around the peak frequencies. A coherence loss correction would increase the levels at high velocities to a certain extent, and the collapse would be better between all the facilities. This observation provides an idea of a possible (not unique) reason for the scatter observed. To what extent this explains the data should be assessed by applying a coherence loss correction in the levels to both facilities.

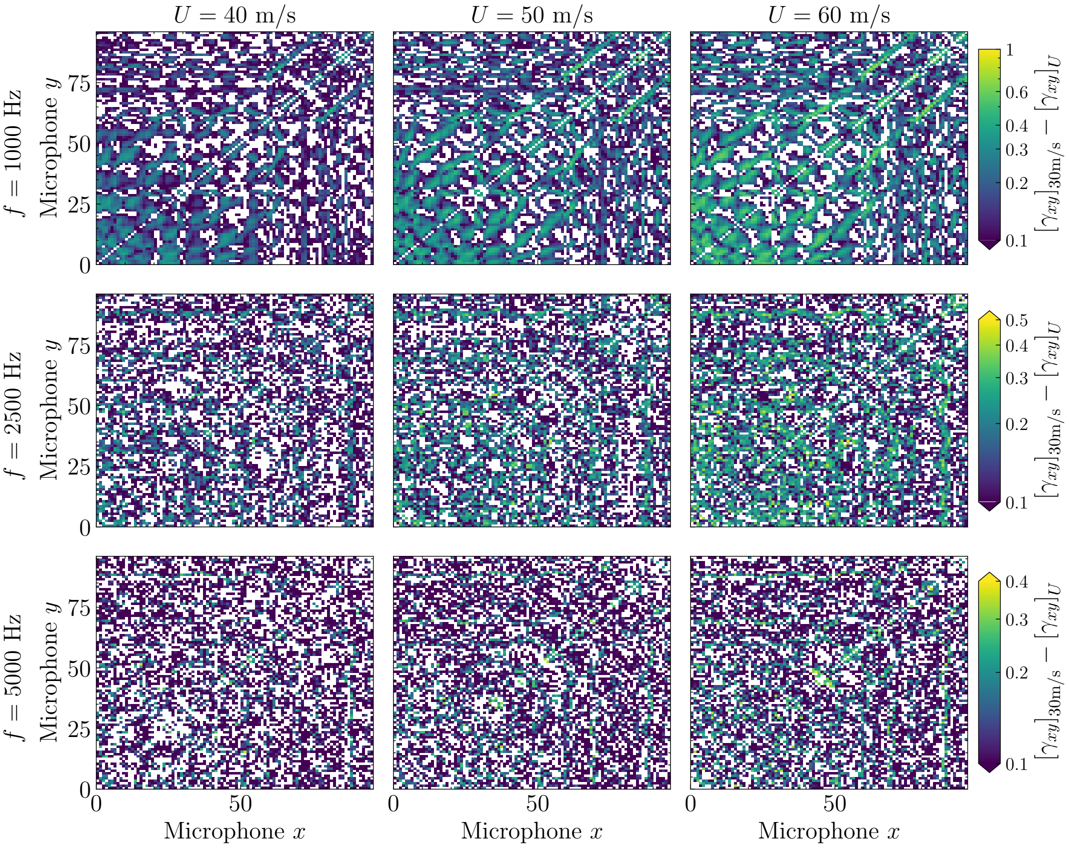

Figure 5.14: Coherence loss in the AWB. x and y refer only to the microphone index, and are not related to the physical position of the microphone in the array.

It is also interesting to hypothesize about the reason for the mismatch in the coherence loss between facilities. The nozzle width was significantly different, and so was the distance between the trailing edge and the shear layer. Assuming a straight shear layer, and taking the same distances as in Figure 5.12a, the distance h was 0.125 m in the A-Tunnel and 0.5 m in the AWB. The trailing edge-array distance H was 1 m in the A-tunnel and 0.9 m in the AWB. A possible argument is that the refraction induced by the random turbulent structures of the shear layer has more effect in the A-Tunnel because the sound waves travel a higher distance and hence introduce a higher time delay. This is the same reasoning why wind tunnels with higher H/h should have higher corrections for shear layer refraction (Figure 10.18 of [36]).

5.3. Microphone location uncertainty

This Section studies how the uncertainty of the microphone locations is propagated to the beamforming images and the integrated spectra. Section 5.3.1 starts by checking the general response and the sensitivity of the input uncertainty σ_{loc} for the DTU and the A-Tunnel. The effect of correlated/uncorrelated input uncertainty is evaluated in Section 5.3.2. The effect of the velocity is studied in Section 5.3.3. All of these results are obtained for the DAS beamformer. The consequences of using Clean-SC are examined in Section 5.3.4. In all the Sections, we will consider only the cases with tripped boundary layer, $\alpha_{eff} = 0$ deg, and straight trailing edge.

5.3.1. Baseline case and sensitivity

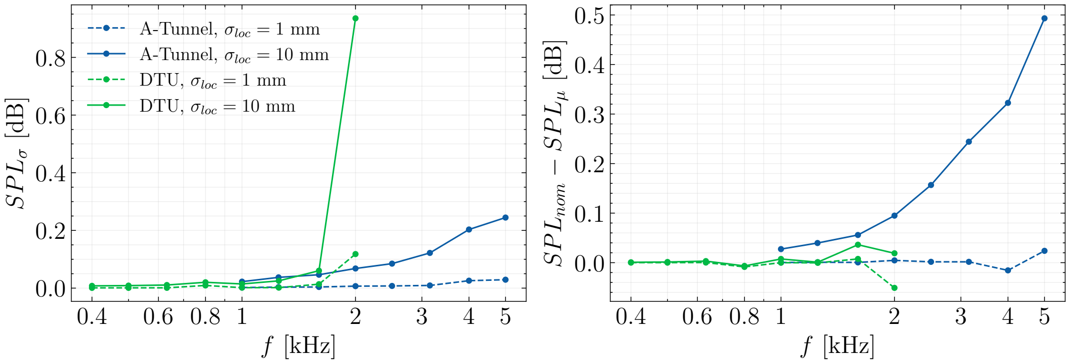

Figure 5.15: Integrated levels sensitivity to microphone location uncertainty.

Uncorrelated microphone location uncertainties of 1 and 10 mm are studied here. Figure 5.15 shows the integrated spectra after Monte-Carlo propagation, using DAS beamforming and SPI. The standard deviation of the spectra SPL_σ and the deviation with respect to the nominal values $SPL_{nom} - SPL_\mu$ is shown. Both SPL_σ and the bias increase with the frequency. This is expected: errors in the microphone location introduce a phase error that reduces the signal cross-correlations. This phase difference is proportional to the frequency. Putting it into equations helps to explain it. Let's follow the same reasoning as [77] and define the perturbed DAS estimate as:

$$\hat{P}_l = \frac{1}{N^2} \tilde{a}_p^H G \tilde{a}_p \tag{5.2}$$

Where $\tilde{a}_p$ is the perturbed steering vector, which can be written as:

$$\tilde{a}_p = \frac{1}{r_{l,0}} \left[\left(r_{l,1} + \delta r_1\right) \mathrm{e}^{-\mathrm{j}k\left(r_{l,1}+\delta r_1\right)}, \dots, \left(r_{l,N} + \delta r_N\right) \mathrm{e}^{-\mathrm{j}k\left(r_{l,N}+\delta r_N\right)} \right]^{\mathrm{T}} \tag{5.3}$$

Where δr_n is the projection of the perturbation of the n-th microphone in the source-microphone direction. It can be positive or negative since they come from i.i.d. normal distributions centered at the nominal positions. $r_{l,0}$ is the distance from the l-th source to the center of the microphone array, which was also perturbed but can be assumed unmodified here to simplify the explanation. Considering that G is based on the unperturbed locations, we can write [77]:

$$\hat{P}_l = \left| \frac{1}{N} \sum_{n=1}^{N} \left(1 + \frac{\delta r_n}{r_{l,n}}\right) \mathrm{e}^{\mathrm{j}k\delta r_n} \right|^2 \tilde{P}_l \tag{5.4}$$

Which shows the relation between the estimated nominal power $\tilde{P}_l$ and the perturbed one $\hat{P}_l$. We see that without perturbations ($\delta r_n = 0$) they are equal. With $\delta r_n \neq 0$, the factor $1 + \delta r_n / r_{l,n}$ can be either greater or lower than 1. However, the phase term $e^{jk\delta r_n}$ will always be equal or lower than one. Note that k is the wave-number $k = 2\pi f / c$. The shift in phase is proportional to the frequency, and hence the reduction with respect to the nominal values gets increasingly important with f. To show this clearly, this factor is plotted for different values of f in Figure 5.16.

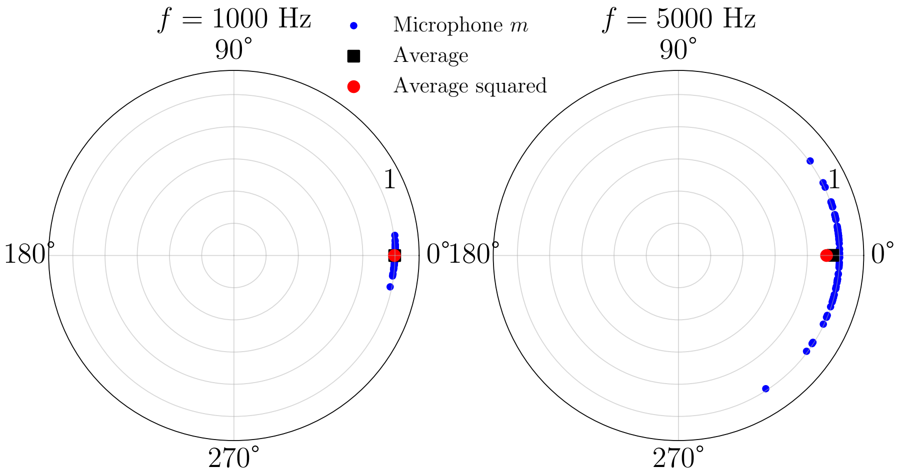

Figure 5.16: Effect of the f on the importance of the phase differences in Equation (5.4). A-Tunnel data and σ_{loc} = 10 mm and one Monte-Carlo sample.

Figure 5.16 shows the factor between $\tilde{P}_l$ and $\hat{P}_l$ at 1 and 5 kHz for the A-Tunnel results. The red marker shows directly the ratio between the nominal and the perturbed values. The effect of the frequency in the phase is very obvious. These plots are for a single Monte-Carlo sample, and the blue markers represent the value for each microphone. Additionally, this simplified ratio has also been calculated for all Monte-Carlo samples, and the mean $10\log_{10}(\tilde{P}_l/\hat{P}_l)$ matched quite well with the bias shown in Figure 5.15. Therefore, it is found that this simplified calculation can allow to get a very quick estimate of the possible bias.

The effect of the frequency has been addressed. To continue exploring the results of Figure 5.15 we should assess what is happening in the DTU results at 2 kHz. A surprisingly high value of SPL_σ is observed. Figure 5.17 shows the beamforming images from Monte-Carlo at this frequency (SPL mean and standard deviation). A dominant source is observed outside the trailing edge. It corresponds to the pitot tube. The pitot tube peak is found at $St_d = fd/U = 0.198$ where d is the pitot tube diameter (5 mm) [46]. It will be shown later that the variance is higher at locations where the levels are lower. This dominance of the pitot tube tube in the beamforming image is then driving the SPL_σ peak at 2000 Hz. This is a representative example of what could happen if the trailing-edge noise is not the dominant source, or if the SNR is too low. The DTU results at high frequencies have been omitted here due to the low SNR. Appendix C explains how the criteria was defined to remove the high frequency bands. The uncertainty analysis of these low SNR bands also revealed an increased variance of the integrated levels (not shown).

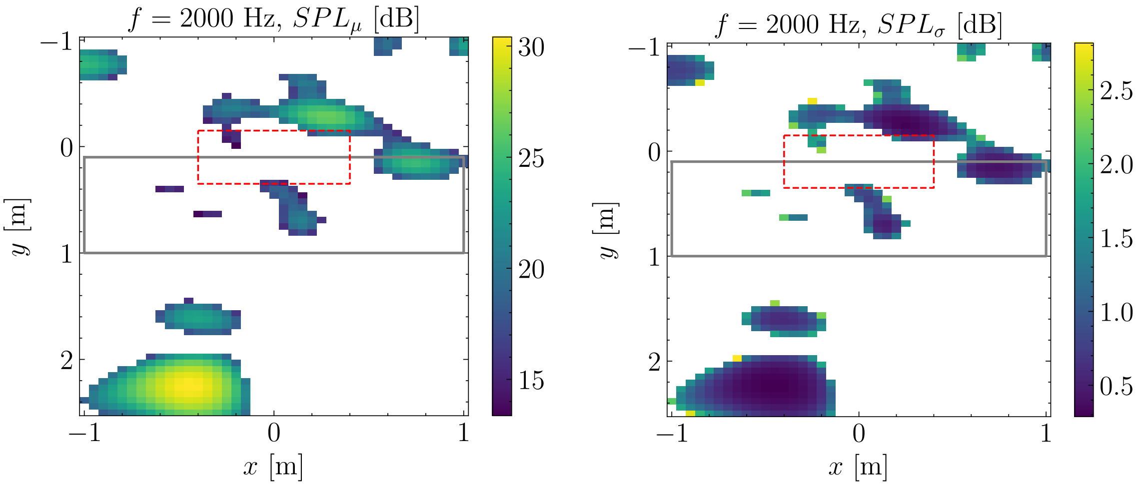

Figure 5.17: Beamforming images from Monte-Carlo. DTU at 50 m/s and 2000 Hz. Flow goes to negative y. σ_{loc} = 10 mm

Figure 5.18 shows the beamforming images from the A-Tunnel at 3150 Hz. The mean and the standard deviation of the SPL are presented. The lower variance values are found in regions where the levels are high. Appendix E shows the images for both facilities at $f = 1250$ Hz. The trend is the same, but the bias and the SPL_σ are lower. In Figure 5.19 a slice across the trailing edge of the beamforming image is plotted. In the extremes of the figure, far away from the source, the variance is greater. Two different frequencies are presented. We can see again more bias and variance for the higher frequency. This is very good for our interests, since the variance in the integration region is kept to a minimum.

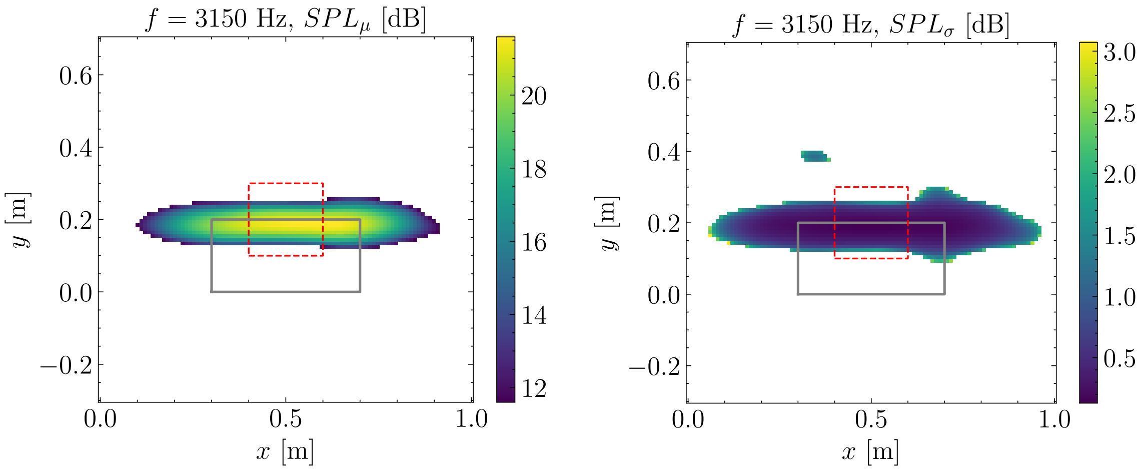

Figure 5.18: Beamforming images from Monte-Carlo. A-Tunnel at 45 m/s and 3150 Hz. Flow goes to positive y. $\sigma_{loc} = 10$ mm

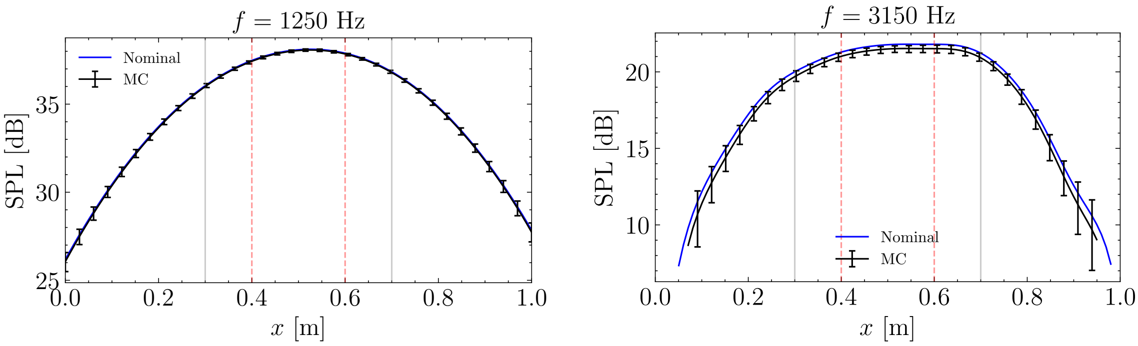

Figure 5.19: Trailing edge slice plots of the beamforming images from the Monte-Carlo results for the A-Tunnel. $\sigma_{loc} = 10$ mm

5.3.2. Correlated uncertainty

We have studied the effect of uncorrelated uncertainty in the microphone positions. This is, perturbing each microphone individually. We now evaluate the effect of perturbing the whole array together. Figure 5.20 shows the comparison of both cases at σ_{loc} = 10 mm. The correlated cases show slightly more variance at low frequencies. However, the standard deviation is still very low. The bias, however, is reduced in the correlated case. The likely reason is that moving all the microphone together creates a similar phase shift in the signals which does not reduce the estimated power levels that much.

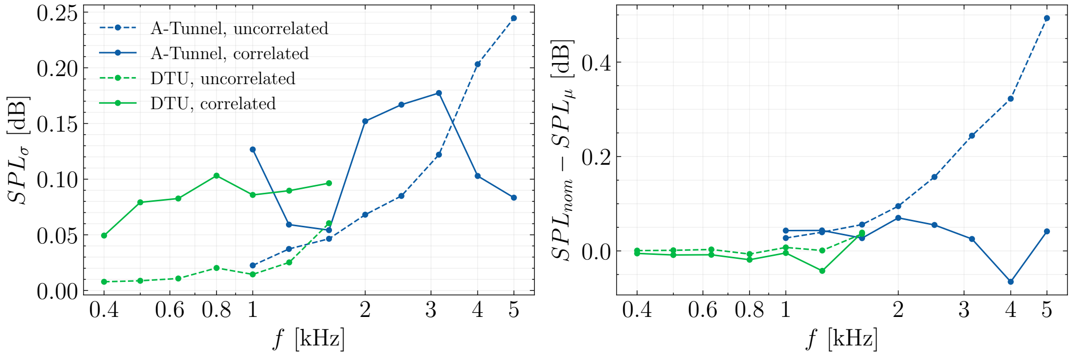

Figure 5.20: Spectra uncertainty from correlated and uncorrelated microphone location uncertainty. σ_{loc} = 10 mm.

To elaborate further on the effect of correlated errors, the whole array is perturbed now 10 mm separately in the streamwise, spanwise, and normal directions. The bias is shown in Figure 5.21. Negligible effect is again observed, and a more sensitive direction is not clearly identified. Therefore, we conclude that individual microphone errors (or array twisting/misalignment) may be more important than a bias in the array location.

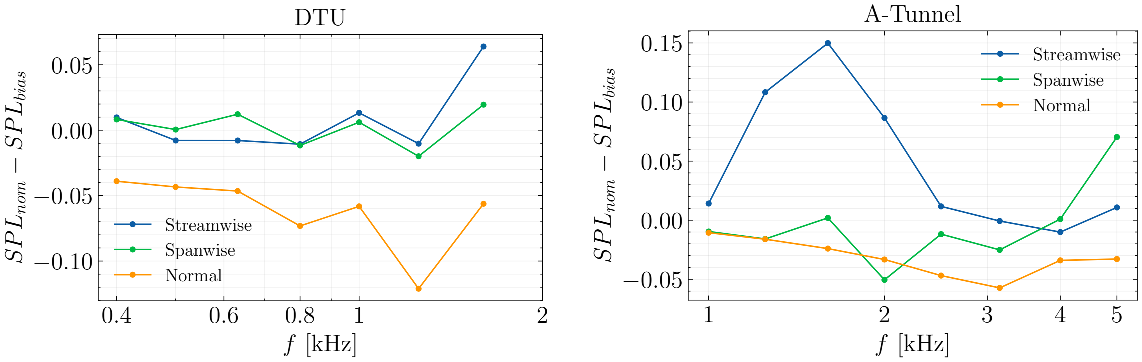

Figure 5.21: Spectra differences due to bias in the array position.

5.3.3. Velocity effect

The effect of the wind tunnel velocity is assessed now. Figure 5.22 shows the standard deviation and bias for three different velocities. Uncorrelated input uncertainty with $\sigma_{loc} = 10$ has been used. Both facilities' results show no change with the velocity in neither the variance or the bias.

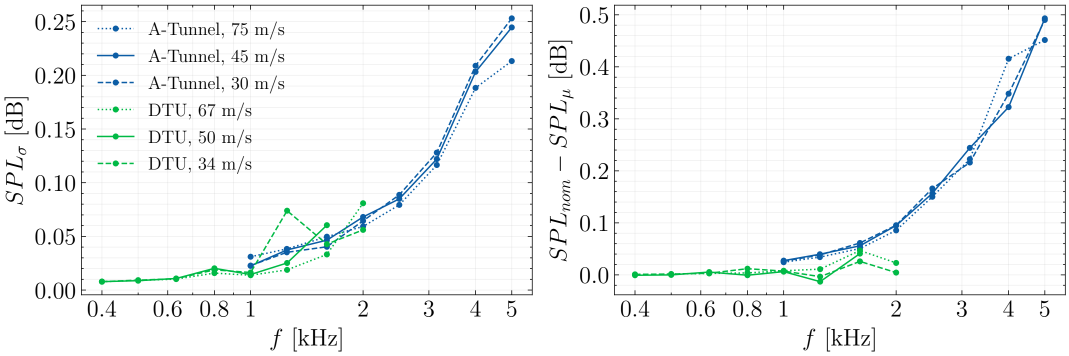

Figure 5.22: Spectra uncertainty at different wind tunnel velocities. $\sigma_{loc} = 10$ mm.

To put the results in perspective, the spectra with error bars are shown in Figure 5.23. The error bars correspond to ±1.96σ (95% confidence intervals). The nominal values are shown in dashed lines. The nominal and the mean Monte-Carlo spectra are practically indistinguishable, and the confidence intervals are barely visible, specially at low frequencies. We can already conclude that the microphone location error does not introduce significant uncertainty (<1 dB) to the integrated spectra using the DAS beamformer.

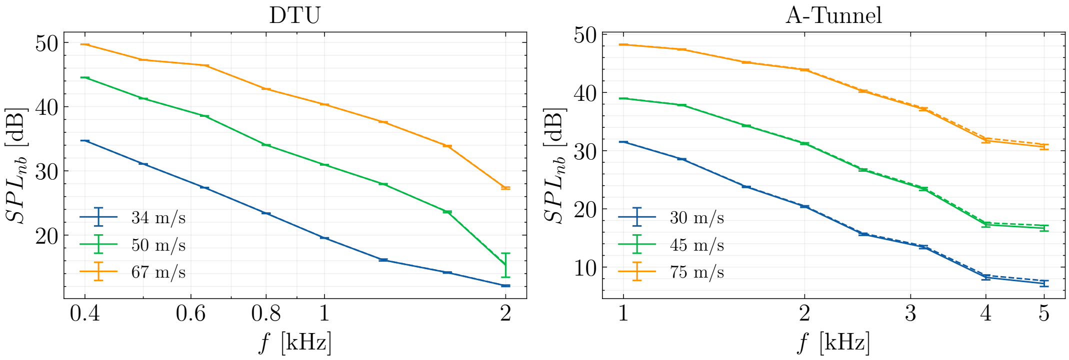

Figure 5.23: Spectra with error bars at different wind tunnel velocities. $\sigma_{loc} = 10$ mm. Error bars correspond to ±1.96σ confidence intervals.

5.3.4. Beamforming method effect

Finally, the effect of using Clean-SC instead of DAS is assessed. Figure 5.24 compares the uncertainty propagated by both methods under an input uncorrelated uncertainty of σ_{loc} = 10 mm. Clean-SC results show higher standard deviation in all the frequency range. Interestingly, the peak seen before at 2 kHz is not observed. Clean-SC results are not that sensitive to regions with more than one source.

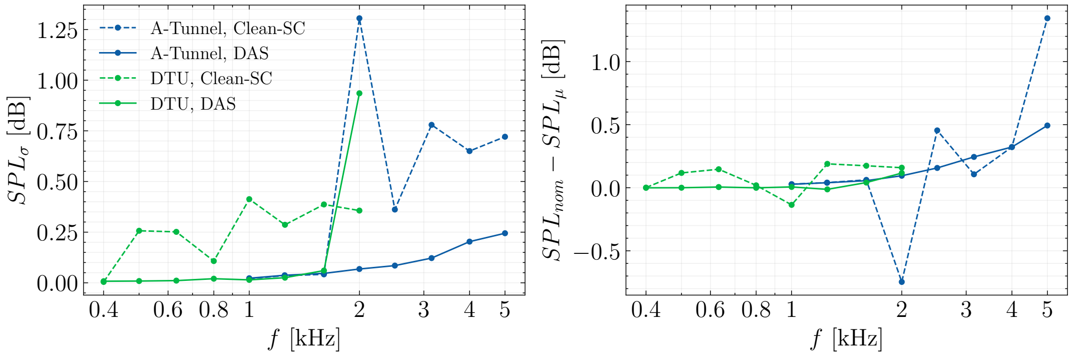

Figure 5.24: Spectra uncertainty for DAS and Clean-SC. σ_{loc} = 10 mm.

To understand the increase of SPL_σ with Clean-SC, we can look at Figure 5.25. The histogram of the integrated levels is plotted for the DTU results at 1250 Hz and for the A-Tunnel at 2000 Hz. We can see how the results are no longer normally distributed. Two different phenomena lead to the sparsity of the integrated levels. In the DTU case, the location of the dominant sources stays the same in the different samples, but the estimated levels vary (see Figures E.3 and E.4). In the A-Tunnel case, the additional variance of the results is given because the dominant source is located very close to the integration region limits. Hence, some perturbed microphone positions move the estimated location in and out of the integration region, leading to a higher variance (see Figures E.5 and E.6). In the latter case, this also explains why $SPL_\mu > SPL_{nom}$ at 2 kHz. In the nominal case, the dominant source lies just outside the integration region, but in the perturbed cases it is usually estimated inside.

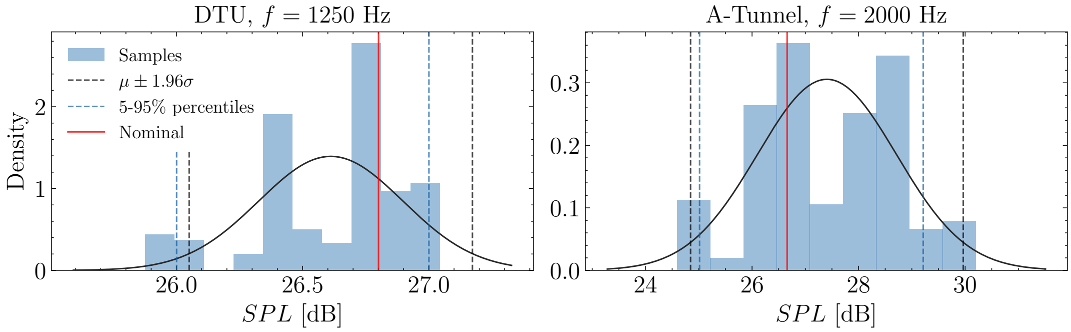

Figure 5.25: Histogram of the integrated SPL using Clean-SC.

The normal distribution is very badly conditioned to represent the Clean-SC results. In Figure 5.25 the 95% intervals of the assumed normal distribution are compared to the corresponding percentiles (dashed vertical lines). The latter is considered to be a better representation of the uncertainty for this type of sparse asymmetrical results. Although there are visible differences in the extremes of the confidence intervals, the general trends are fairly covered solely by using σ. Figure E.7 shows the normalized length of the confidence intervals using the percentiles, and very similar results as the Figure 5.24 are observed. The takeaway is that it is better to use percentiles to represent the confidence intervals rather than $\mu \pm 1.96\sigma$.

Nonetheless, the conclusion extracted before still holds: the microphone location uncertainty affects more the Clean-SC integrated spectra compared to DAS. This can be specially important if the dominant source lies close to the integration region limits, since errors in the microphone positions can move it in or out.

6

Conclusions and recommendations

The conclusions of the work conducted are outlined in this Section. A summary of the results and findings is firstly presented, and suggestions for future work are then proposed.

6.1. Summary

Benchmark definition

To improve the trailing-edge noise database and create a benchmark more applicable for wind turbine purposes, two models of the NACA 63_3-018 were tested. The models had different chord lengths (0.2 and 0.9 m) and adjustable span lengths. They have been tested in 5 different facilities: the A-Tunnel and the LTT at TU Delft, the Poul La Cour Tunnel at DTU, and the AWB and the NWB at DLR. The Re_c range of the measurement spanned from 0.18×10^6 to 4.8×10^6. Various conditions were tested, including angles of attack up to stall, tripped and clean boundary layer, and sawtooth and iron serrations at different flap angles.

Aerodynamic results

Firstly, an aerodynamic comparison was conducted. The expected trends were observed. Tripping the boundary layer decreases $C_{l,max}$ and lowers the Re_c sensitivity in the stall region. Increasing Re_c leads to a delayed separation and a greater $C_{l,max}$. The agreement between facilities was good, and some deviations in the lift coefficient slope were attributed to the different aspect ratios in the wind tunnels. Laminar separation bubbles on both sides of the airfoil were identified at low Reynolds number and natural transition. Additionally, the aerodynamic measures with Kevlar and hard walls were also compared, and good agreement was obtained. Next, the effect of the serrations on the lift coefficients was studied. Both serration geometries lead to an increase of C_l due to the additional chord length. The iron serrations showed a more pronounced ΔC_l, attributed to a larger surface area. The presence of flap angle increased even more C_l because it introduces camber to the airfoil shape. However, the serrations presented some uncertainties regarding the real flap angle. Lastly, the boundary layer displacement thickness was calculated and compared to XFOIL. The broad trends with Re_c and tripping were captured but there was still some unexplained scatter.

Acoustic results with straight trailing edge

After checking that the aerodynamics were consistent and addressing the differences, the acoustic results with straight trailing edge were studied. The effect of the tripping was investigated. With respect to the natural transition case, forcing the transition lead to a level increase up to 5 dB at low frequencies. This was attributed to an increase of δ^*. Broadband peaks at high frequencies were also identified and attributed to trailing-edge bluntness noise. Comparing different angles of attack, it was found that increasing α_{eff} led to an increase in levels at low f and very high f. The levels decreased at intermediate frequencies. This is explained by the thicker boundary layer on the suction side and the thinner one on the pressure side. At low Re_c, if the transition is not forced, laminar boundary layer instability tones appeared at non-zero α_{eff}. They were very Re_c dependent, but a good agreement was observed between facilities in the peak location and level. After checking that the qualitative trends in the different wind tunnels were equivalent, the results were scaled to the same conditions and quantitatively compared. Using free-stream properties and δ^*_{SS}, or the so-called "mixed boundary layer scales", leads to the best collapse. It better represents the noise production at low frequencies. Using measured boundary layer scales did not help to achieve a better result. There was a good agreement in the peak level and location, especially between DTU and AWB data. The A-Tunnel results showed a particularly pronounced trend with the velocity, which did not appear in the other facilities or the BPM expectations. The scaled results at $\alpha_{eff} \approx 3-4$ deg showed similar collapse as the baseline case, but at $\alpha_{eff} \approx 7-8$ deg the Re_c effects were very noticeable. From this point, the boundary layer of the LRM start to separate and the aerodynamics are already divergent, leading to different acoustic results.

Noise reduction effect of serrations

The noise reduction effect of the serrations has also been studied. The tones mentioned above were significantly attenuated with the add-ons installed (up to 10 dB in OSPL). In the tripped cases, the noise reduction $\Delta\text{SPL}_{1/3}$ scaled well with St_{δ^*} and showed a good agreement between facilities and Re_c. In general, two noise reduction regions could be identified in the spectra. The iron serrations provided up to 7.5-8 dB of maximum noise reduction at low frequencies, while for the sawtooth geometry it was around 5 dB. Increasing the angle of attack, or adding a flap angle, reduced the noise reduction effect. This was attributed to the increased loading and the appearance of counter-rotating vortices in the serration edges. The ΔOSPL against C_l has also been studied, since it is a parameter more linked to wind turbine blade design rather than α_{eff}. It was observed that the additional noise reduction of the iron serrations at $\alpha_{eff} = 0$ is not present at higher C_l (where a wind turbine would operate).

Post-processing investigation

The differences in the post-processing were investigated to study the previously mentioned mismatch in the scaled results. Since the original A-Tunnel data was obtained using the DAS beamformer, the results were reprocessed using Clean-SC, which was the choice of the other facilities. Lower integrated levels were retrieved from this method, but the same trend with the velocity was seen. The beamformer algorithm then could not explain the difference. A straight shear layer was assumed in the processing of the A-Tunnel data. Varying the shear layer distance did not affect the results. However, the effect of the jet angle was not assessed, which could supersede the distance error. Then, the coherence of the microphone signals was calculated and compared to the AWB. As expected, the coherence loss was greater with the frequency and the tunnel velocity. However, the velocity effect was more notable in the A-Tunnel. This additional coherence loss could introduce a decrease in levels at high velocities, which could partially explain the mismatch. However, a more detailed study is required to check if this is the case.

Microphone location uncertainty

Finally, an investigation on the microphone location uncertainty was carried out. The Monte-Carlo method was applied to the DAS beamformer. The DTU and A-Tunnel data were investigated. It was firstly observed that errors in the locations could lead to a bias in the estimated levels at high frequencies. This is because the phase delay that a location error can introduce is proportional to the frequency. Nonetheless, the possible bias and the variance created by this source of uncertainty were minimal (<0.5 dB for a standard deviation of 10 mm in the microphones position). Meaningful differences between facilities could not be identified. Still, a parametric study was done to check the dependencies and whether there was a specially sensitive case. It was shown that the uncorrelated uncertainty (each microphone having a different error) leads to a higher bias at high frequencies but lower variance at low frequencies than the correlated counterpart (errors in the whole array). Different wind tunnel velocities lead to the same variance and bias. Lastly, the effect of using Clean-SC was assessed. The variance was higher than in the DAS case but the standard deviation was generally still lower than 1 dB in the integrated levels. Errors in the microphone location can play an important role for Clean-SC if the dominant sources are located close to the integration region. Overall, it was found that microphone locations are not an essential source of uncertainty for trailing edge noise, where the relevant frequencies are on the low side (≤ 2 kHz). However, they could become more important if Clean-SC deconvolution is used. Other uncertainty sources should also be considered to characterise the measurements accurately. This will be proposed in the next Section.

6.2. Suggestions for further research

There are still some open questions and future work that could be done to understand the measurements better, complete the data set, and extend the knowledge of aeroacoustic measurements uncertainty. Further tasks in this direction are listed below:

1. Add measurements at high Reynolds numbers to provide a direct comparison with the DTU data. The DTU data has been cross-validated with Virginia Tech measurements in a separate study [70]. However, the comparison of the ΔSPL with serrations is not available. We saw a difference between the LRM and the HRM with the iron serrations (Figure 23 of Appendix B). It would be interesting to have more measurements at high Re_c since the cause of the noise increase at high St_{δ^*} and high Re_c is not fully understood.
2. It would be ideal to close the complete causality chain to provide a better benchmark for computational validation. We now have aerodynamic force coefficients, velocity profiles at the trailing edge, and far-field noise. Adding wall-pressure spectra to the data set would provide another intermediate step. It would be helpful for the comparisons with the numerical predictions, and it may also be interesting to compare them between facilities.
3. Some trends in the results are not clear yet. We did not solve why the A-Tunnel had a more pronounced trend with the velocity on the scaled results. We suggested that the coherence loss could play a role. It would be interesting to apply a coherence loss correction in the spectra and study to what extent it explains the scatter.
4. Linked to the preceding point, we checked the effect of the shear layer distance in the A-Tunnel but neglected the jet expansion angle. This could be investigated by devising the shear layer correction considering a tilted shear layer.
5. A parametric investigation on the microphone location uncertainty was conducted. It was interesting to study the dependencies, but it does not quantify the total uncertainty of the measurements. The present analysis should be extended including the effects of the tunnel temperature, the CSM averaging, and the microphone sensitivities.

A

Uncertainty quantification theory

This Section provides an introduction to the concepts and methods that have been used in this Thesis. The following theory has been retrieved from the books of Smith [94] and Coleman and Steele [95].

For *uncertainty* we could mean two fundamentally different quantities. *Aleatoric uncertainty* represents the stochasticity of a quantity. It represents the intrinsic variability of the process in question and therefore cannot be reduced. *Epistemic uncertainty* represents the lack of information about a variable. It can be reduced by better understanding, modelling, or measuring the quantity. For instance, higher quality equipment produces results with smaller tolerances.

Uncertainty quantification (UQ) is used to quantitatively characterise the uncertainties (variances or biases) to gain information about the accuracy and precision of a model or measurement. Any result with a good statistical representation is much more useful because it sets the degree of trust and comparability. If we are comparing two different noise measurements that are 1 dB apart, but their measurement uncertainty is ±2 dB, we know that the results can be considered to be collapsed, and any better match would be luck.

UQ deals with two main types of problems. The *forwad problem* or propagation of uncertainty deals with how the sources of uncertainty in a model or experiment are propagated to the final result. The objective is to predict the overall uncertainty of the quantity of interest. For instance, we would like to know how the C_l may vary if we have uncertainty in α. The *inverse problem* goes the other way and tries to estimate the unknown input parameters based on the uncertainty of the results or observations. For example, we could go the opposite way and try to estimate the α distribution that leads to a series of C_l measurements. The inverse problem is usually much more difficult.

Random variables and probability distributions

Random variables are the workhorse of UQ theory. They are defined as a mapping function from a probability sample space into a measurable space. Mathematically, this is stated as $X : \Omega \to E$, where X is the random variable, Ω is the sample space, and E is the measurable space. It is also useful to define a single realization of the random variable, given by $x = X(\omega)$. Associated with the random variable X there is a cumulative distribution function (CDF) $F_X : \Re \to [0,1]$:

$$F_X(x) = \mathrm{P}\{\omega \in \Omega | X(\omega) \leq x\} \tag{A.1}$$

From the CDF, the probability density function (PDF) can also be defined:

$$F_X(x) = \int_{-\infty}^{x} f_X(s)ds, \quad x \in \Re \tag{A.2}$$

Where $f_X = dF_X/dx$ is the PDF and of X and maps from $\Re$ to $[0,\infty)$. Statistical moments are another way to represent a random variable. These are quantities that give information about their centrality, variability and symmetry. The general equation for the moments is defined as follows:

$$\mathbb{E}(X^n) = \int_{\Re} x^n f_X(x) dx \tag{A.3}$$

The most used ones are the first and the second moment. They provide a measure of the PDF central location (mean) and variance, and are given as:

$$\mu = \mathbb{E}(X) = \int_{\Re} x f_X(x) dx \tag{A.4}$$

$$\sigma^2 = \text{var}(X) = \mathbb{E}[(X-\mu)^2] = \int_{\Re} (x-\mu)^2 f_X(x) dx \tag{A.5}$$

We have introduced random variables and stated different ways to represent them (samples, PDF, CDF, or moments). Let's introduce now one of the most typical distributions used to represent random variables: the normal or Gauss distribution. Its PDF is given by:

$$f_X(x) = \frac{1}{\sigma\sqrt{2\pi}} e^{-\frac{1}{2}\left(\frac{x-\mu}{\sigma}\right)^2} \tag{A.6}$$

A great advantage of this distribution is that its PDF is only dependent on μ and σ. It has also mathematical benefits. In the following Section, two important theorems which emphasize the importance of this distribution will be given.

Limit theorems

Consider the problem of calculating an estimate of the mean μ and the standard deviation σ of a population of samples x_i and associated random variables X_i. The estimate for the mean (sample mean) is defined in the following equation:

$$\bar{X}_n = \frac{1}{n} \sum_{i=1}^{n} X_i \tag{A.7}$$

And the problem is whether this sample mean represents the true mean with infinite number of samples. This is $\lim_{n\to\infty} \bar{X} = \mu$? The Law of Large Numbers (LLN) is a very useful theorem that addresses this. It is stated as follows: For X_1, X_2, ... independent and identically distributed (iid) random variables with expectations $\mathbb{E}(X_i) = \mu$ and equal and finite variance, we can write for any $\epsilon > 0$:

$$\text{P}\left(\lim_{n\to\infty} |\bar{X}_n - \mu| < \epsilon\right) = 1 \tag{A.8}$$

It means that the probability that the sample mean is equal to the expected value (within the margin ϵ) is equal to one. In other words, it says that just by averaging enough number of samples, the result should be very close to the expected value. We have seen that it is reasonable to use this estimator to get the mean. Next question is to consider whether it is accurate. The variance of the sample mean $\bar{X}_n$ is given by:

$$\begin{aligned} \text{Var}(\bar{X}_n) &= \frac{\text{Var}\,(X_1 + X_2 + \ldots + X_n)}{n^2} \\ &= \frac{\text{Var}\,(X_1) + \text{Var}\,(X_2) + \ldots + \text{Var}\,(X_n)}{n^2} \\ &= \frac{n\text{Var}(X)}{n^2} \\ &= \frac{\text{Var}(X)}{n} \end{aligned} \tag{A.9}$$

Where it has been used that $\text{Var}(aX) = a^2\text{Var}(X)$, and that the random variables are independent and with equal variance. However, there is still no information about the estimate of the sampling distribution. The Central Limit Theorem (CLT) provides an excellent theory in that sense. It is usually worded as follows:

Define X_1, X_2, ... independent and identically distributed (iid) random variables with expectations $\mathbb{E}(X_i) = \mu$ and equal and finite variance. From the LLN take the sample mean $\bar{X}_n$ with mean $\mathbb{E}(\bar{X}_n) = \mu$ and variance $\text{Var}(\bar{X}_n) = \sigma^2/n$. Define the normalized random variable Z_n:

$$Z_n = \frac{\bar{X}_n - \mu}{\sigma/\sqrt{n}} = \frac{X_1 + X_2 + ... + X_n - n\mu}{\sigma\sqrt{n}} \tag{A.10}$$

Which has mean $\mathbb{E}(Z_n) = 0$ and variance $\mathrm{Var}(Z_n) = 1$. The Central Limit Theorem says that the CDF of the random variable Z_n converges to the standard normal.

$$\lim_{n\to\infty} P(Z_n \leq x) = \Phi(x), \quad \text{for all } x \in \mathbb{R} \tag{A.11}$$

Where $\Phi(x)$ is the normal CDF with zero mean and unit variance. The great advantage of this theorem is that it hols independently on the distribution of X_i as long as n is sufficiently large.

To summarize, the combination of the LLN and the CLT allows to represent a population with samples (with respect to the mean) for a sufficiently large n. The probability of this sample mean will approach asymptotically a normal distribution.

Monte-Carlo

Monte-Carlo-based uncertainty analysis takes advantage of the preceding theorems. It is a propagation technique (forward problem) conceptually very simple. A probability distribution is assumed for each input variable. Then each variable is perturbed with a random value drawn from its PDF. These distributions may or may not be correlated. Then, each set of perturbed inputs (a sample) is propagate through the process in question to get a perturbed output. This is repeated for a large number of samples until the output distribution has converged. The convergence of this method follows Equation (A.9). The error is then reduced with the number of samples as $\propto 1/\sqrt{N}$, N being the number of samples. This convergence rate is much slower than high-order spectral or polynomial methods, which clearly outperform Monte-Carlo when the number of variables is reduced. However, these advanced methods suffer the "curse of dimensionality". Their convergence rate, unlike the Monte-Carlo case, is dependent on the number of variables. Therefore, in high-dimensional spaces Monte-Carlo is still a very simple yet powerful tool.

B

Cross-facility benchmarking paper

Benchmarking of the NACA 63_3-018 Trailing-Edge Noise in a Broad Reynolds Number Range as Part of the IEA Task 39

Guillem Vergés i Plaza[*]
Technical University of Denmark, Frederiksborgvej 399, 4000, Roskilde, Denmark
Flow Physics and Technology Department, Delft University of Technology, 2629 HS Delft, The Netherlands

Andreas Fischer[†], Oliver Lylloff[‡], Christian Bak[§], Anders S. Olsen[¶], Franck Bertagnolio[‖]
Technical University of Denmark, Frederiksborgvej 399, 4000, Roskilde, Denmark

Salil Luesutthiviboon[**], Tercio Lima Pereira[††], Daniele Ragni[‡‡], Francesco Avallone[§§]
Flow Physics and Technology Department, Delft University of Technology, 2629 HS Delft, The Netherlands

Alexandre Suryadi[¶¶], Michaela Herr[***]
German Aerospace Center (DLR), Lilienthalplatz 7, 38108 Braunschweig, Germany

An experimental aero-acoustic characterisation of the NACA 63_3-018 airfoil is presented in this study, featuring trailing-edge noise emissions with and without serrations. Measurements have been carried out for a chord-based Reynolds number range between 0.18×10^6 and 4.8×10^6. Two airfoil models with different chord lengths have been tested in five different wind tunnels. The goal is to compare the measurements in different facilities, quantify the uncertainties, and establish a validation database that can serve as a benchmark for computational studies. The tests have been performed with clean and forced-transition boundary layers for a variety of angles of attack. The effect on the spectral slope and peak levels is evaluated. Scaling laws have been applied to compare different test conditions. The quality and nature of the collapse, as well as the applicability limits of the scaling, are examined. Different serration geometries have been tested at different flap angles. The noise reduction dependence on the aerodynamic loading is discussed. This work is based on an initiative of Task 39 "Quiet Wind Turbine Technology" of the Technology Collaboration Programme (TCP) of the International Energy Agency (IEA).

Nomenclature

α_{eff} = effective angle of attack (deg)
α_{geo} = geometrical angle of attack (deg)
b = span width (m)
c = chord length (m)
C_d = drag coefficient (-)
C_l = lift coefficient (-)
C_p = pressure coefficient (-)
δ^* = displacement thickness, subscript may indicate pressure side ($_{PS}$) or suction side ($_{SS}$) (m)

---

[*] MSc Student, European Wind Energy Master - Rotor Design - Aerodynamics, E-mail: guillem.verges@gmail.com
[†] Senior Researcher, Department of Wind and Energy Systems, E–mail: asfi@dtu.dk
[‡] Postdoc, Department of Wind and Energy Systems, E–mail: ollyl@dtu.dk
[§] Professor, Department of Wind and Energy Systems, E–mail: chba@dtu.dk
[¶] Senior Development Engineer, Department of Wind and Energy Systems, E–mail: sols@dtu.dk
[‖] Senior Researcher, Department of Wind and Energy Systems, E–mail: frba@dtu.dk
[**] PhD Candidate, Section Aircraft Noise Climate Effect, E–mail: s.luesutthiviboon@tudelft.nl
[††] PhD Candidate, Section Wind Energy, E–mail: l.t.limapereira@tudelft.nl
[‡‡] Associate Professor, Section Wind Energy, E–mail: d.ragni@tudelft.nl
[§§] Assistant Professor, Section Wind Energy, E–mail: f.avallone@tudelft.nl
[¶¶] Research Engineer, Dept. of Wind Energy, Institute of Aerodynamics and Flow Technology, E-mail: alexandre.suryadi@dlr.de,
[***] Head of Wind Energy Department, Institute of Aerodynamics and Flow Technology, E-mail: michaela.herr@dlr.de

f = frequency (Hz)
t_{TE} = trailing-edge thickness (m)
M_U = wind tunnel free-stream velocity based Mach number (-)
$OSPL_{1/n}$ = overall sound pressure level calculated from 1/n octave band spectrum (dB)
PSD = far-field noise power spectral density (dB/Hz)
r = distance between the observer and the sound source (m)
Re_c = chord-based Reynolds number (-)
$SPL_{1/n}$ = 1/n octave band sound pressure level (dB)
$SPL_{1/n,scaled}$ = scaled 1/n octave band sound pressure level (dB)
$\Delta SPL_{1/n}$ = noise reduction based on 1/n octave band sound pressure level (dB)
St_ℓ = Strouhal number based on characteristic length ℓ (-)
U = wind tunnel free-stream velocity (m/s)
X, Y, Z = chordwise, vertical, and spanwise coordinates from the TE (Fig. 1) (m)

I. Introduction

Trailing-edge (TE) noise arises from the interaction of the turbulent boundary layer, and the pressure fluctuations that it generates in the surface, with the trailing edge [1, 2]. It has been identified as a primary noise source for wind turbines [3]. It is thus of industrial interest to predict and mitigate its impact, an example of this is the Task 39 of the International Energy Agency Wind Technology Collaboration Programme (IEA Wind TCP Task 39). Its goal is to accelerate the development and deployment of quiet wind turbine technology by providing supporting research database as the foundation for establishing international standards and governmental regulations. The task addresses the engineering questions of wind turbine noise generation, reduction, and propagation, and the socio-psychological questions of the wind turbine noise impact to health, well-being and consent and other non-noise factors. An interdisciplinary work group is also established to disseminate the interaction between engineering and socio-psychological sciences.

The goal of this collaborative paper is to create a high quality and comparable database of trailing-edge noise from both straight and serrated TEs. A very related effort in the same direction is the Benchmark problems for Airframe Noise Computations (BANC) workshop (category I, TE noise), a series of workshops which aim to cross-check available measurement data with different computation methods [4–6]. The experimental data-sets available so far were composed of a symmetric NACA 0012, a cambered DU96–W180, and a NACA 64-618 airfoils without serrations in a Re_c range from 1×10^6 to 1.5×10^6. This Reynolds range, however, is lower than the one that modern wind turbines work at. It is also desirable to characterise the error bars and understand the uncertainty in the measurements carried out with different models and in different facilities. Additionally, serrations have become largely used to reduce the trailing-edge noise of wind turbines [7], and experimental data is required to validate new noise models (e.g. [8]). Therefore, it is of high interest to include serrations into the data-base.

These gaps were partially tackled in the study of Ferret Gasch et al. [9] where two Siemens-Gamesa cambered airfoils were tested to a maximum Re_c of 3.7×10^6. These results were used to blindly test the accuracy of different noise prediction codes. The recommendations of such study insisted again in the need of carrying out uncertainty quantification of the measurements and improve the validation database specially at moderate to high Reynolds numbers.

The leading aero-acoustic facilities in Europe have carried out cross-facility aero-acoustic tests of a NACA 63_3-018 airfoil as the first collaborative step to establish the database as well as to quantify the uncertainty. This airfoil has been selected because its symmetry helps to accurately determine the zero angle of attack, but when placed at different α the resulting pressure distributions are similar to those commonly found in wind turbines (e.g. [10]). In order to cover the largest Re_c possible, two models have been built: a large one (subsequently called *HRM*: High Reynolds number Model), with 0.9 m chord, and a small one (*LRM*: Low Reynolds number Model) with a chord of 0.2 m. The HRM has been tested in the Poul La Cour Tunnel (PLCT) at the Denmark Technical University (DTU), and the LRM has been studied in both the A-Tunnel at TU Delft, and the Acoustic Wind Tunnel Braunschweig (AWB) in the German Aerospace Center (DLR). The aerodynamics of the HRM have also been measured in the low-speed Wind-Tunnel Braunschweig (NWB) of the German-Dutch Wind Tunnels Foundation (DNW) and in the Low-Turbulence Tunnel (LTT) of TU Delft.

This paper presents preliminary comparisons of test results from the aforementioned facilities. This paper is structured as follows. A description of the model and serration geometries is given in Section II, followed by a summary of the facilities set-up in Section III. The aerodynamic results are then analysed in Section IV, succeeded by the study of the acoustic results with straight trailing edge in Section V. Finally, the effect of the serrations is discussed in Section VI.

II. Model Description

Two NACA 63_3-018 airfoils (Fig. 1) were built for this study, namely the Low Reynolds number Model (LRM) and the High Reynolds number Model (HRM). They have a chord length of 0.2 m and 0.9 m respectively. The base span width is 0.4 m for the LRM and 1.816 m for the HRM, and modular extensions were also built to adapt the models to the specific heights of the wind tunnel test sections. The LRM span width was 0.4 m when tested in the A-Tunnel, and 0.8 m in the AWB. For the HRM, these values were 1.25 m in the LTT, 2 m in the PLCT (DTU), and 2.8 m in the NWB. The HRM was made of sheet metal skins over rib and stringer structures. The LRM was manufactured as an assembly of three solid modular aluminium structures. More details about the models may be found in [11, 12]. The trailing edge thickness is $t_{TE} = 7.5c \times 10^{-4}$ for both models.

The HRM is equipped with 192 surface pressure tabs. They are organised in 7 rows in order to characterise the flow three-dimensionality. The main row, in the middle of the model, has higher density with 96 tabs. They have an offset in the spanwise direction to minimise interferences. In the LTT, since the base span of the model could not fit completely in the test section, this mid row was not fully centered. It was located around $1c$ (0.9 m) from the bottom wall instead. The LRM has 28 pressure tabs in the middle of the span with an spanwise angle of 15 deg.

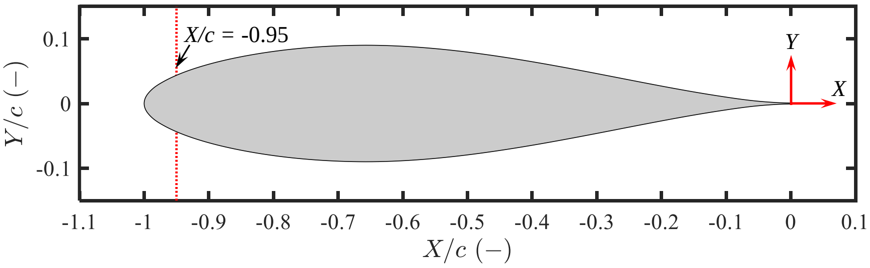

Fig. 1 NACA 63_3-018 airfoil with tripping location and axis orientations.

The measurements have been carried out with both clean and tripped boundary layer. The forced transitions helps with the comparability of the results, and supports the reproducibility of the measurements. For the tripped boundary layer case, zig-zag strips have been employed at $X = -0.95c$ on both sides of the airfoil. For the LRM a thickness of 0.5 mm, a width of 6 mm, and an angle of 70 deg. have been used. For the HRM these values are 0.4 mm, 12 mm, and 60 deg. respectively. The HRM tripping was applied with a base tape of 0.06 mm thickness (Fig. 7).

Different trailing-edge serrations have been tested. Two geometries have been selected: sawtooth and iron serrations, illustrated in Fig. 2. The geometries are taken from a numerical investigation of Avallone et al. [13], which compared the iron serrations to the conventional sawtooth ones, and found increased noise reduction in the former. This was attributed to decreased scatter in the serration roots. The serrations' wavelength is $0.05c$, and the peak amplitude is $0.1c$. Both types have been installed parallel to the chord ($\varphi = 0$ deg), and the sawtooth serrations have also been tested at $\varphi = 8$ deg for the LRM and $\varphi = 4$ deg for the HRM. Details about the installation procedure may be found in the work of Luesutthiviboon et al. [11]. There is significant uncertainty in the flap angle of the serrations. This has been measured in the serrations tested by DTU, where important deviations from the nominal values were detected. The iron and sawtooth serrations which should have been placed at $\varphi = 0$ deg were measured to be at 4.16 deg and 4.43 deg respectively. Moreover, spanwise differences up to 3.8 deg were also found. For the flapped case at nominal $\varphi = 4$ deg. the real value (spanwise averaged) was 9.39 deg.

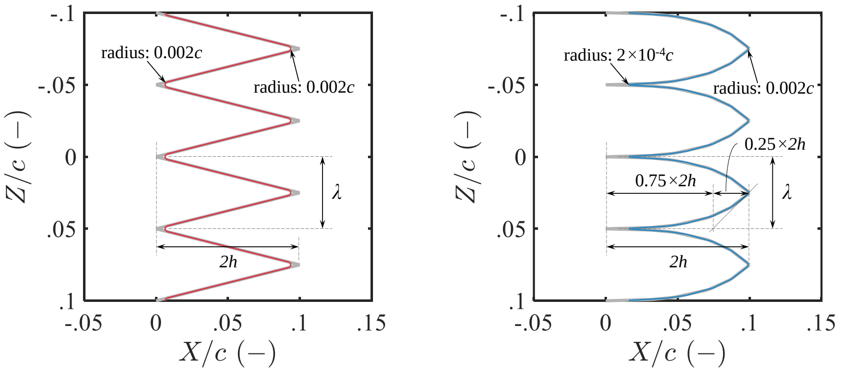

(a) Sawtooth serrations **(b) Iron serrations**

Fig. 2 Drawings of the trailing-edge serrations used on the airfoil. In gray, the geometry used in the study of Avallone et al. [13].

III. Facilities Description

A. The PLCT at DTU

The Poul La Cour Wind Tunnel is a closed loop return wind tunnel (Fig. 3). The airline is 66 m long and 27 m wide (furthest separated points of the airline tube, but neglecting the wind tunnel buildings). The air volume inside the airline is about 3875 m^3. The whole airline is built in concrete because of acoustic considerations. The fan of the wind tunnel is driven by a 2.4 MW engine and has a diameter of 4.7 m. The fan was limited to 400 RPM or an engine power output of 1.8 MW, because the tunnel loss estimate proved to be too conservative. The fan can generate an air flow of up to 630 m^3/s at 400 RPM when a test object is placed in the tunnel.

The settling chamber has a cross section of 6 x 9 m and is equipped with a honeycomb and 3 mesh grids to rectify the flow and reduce turbulence before entering the test section. The mesh grid goes from a coarse to a fine mesh size. The grid size of the finest mesh is 0.2 mm. The flow is accelerated through a nozzle with a contraction ratio of 9:1 before entering the test section. The test section has a cross section of 2×3 m and is 9 m long. The top speed is 105 m/s and the turbulence intensity is below 0.1 %.

Measurements can be carried in a traditional hard-wall configuration [14] to focus on the aerodynamics, or in the acoustic configuration that is based on the new Kevlar wall technology [15]. The noise is measured by a phased array with 84 microphones of the type B&K type 4985 1/4". It is placed in the anechoic chamber with a distance of 1.2 m from the Kevlar wall, and it is centered above the trailing edge of the aerofoil and its mid-span. The microphone data was acquired with a B&K LAN-XI type 3053 system at a sample rate of 16384 Hz. The measurements have been post-processed using the deconvolution algorithm *CLEAN based on spatial coherence*, CLEAN-SC [16]. More information about the set-up and the post-processing may be found in O. Lylloff's PhD [17].

B. The A-Tunnel at TU Delft

At Delft University of Technology, the small NACA 63_3-018 was tested in the A-Tunnel, an open-jet anechoic vertical wind tunnel. Full description of the facilities and results to be further discussed in this paper have been presented in a publication of Luesutthiviboon et al. [11]. In the A-tunnel, a semi-open test section is placed in a room treated by acoustically absorbent foam wedges. Acoustic characterization of the A-Tunnel anechoic chamber including further extensive details can be found in a publication of Merino-Martinez et al. [18]. To achieve different free-stream velocity ranges, the test section can be placed on different outlet nozzles having different contraction ratios. Two different nozzles have been used for the measurements, one with a cross-section of 400×700 mm ($2c \times 3.5c$), which will be referred as *Large* or *TUD-A-L*, and one with a cross-section of 400×250 mm ($2c \times 1.25c$), which will be called *Small* or *TUD-A-S*. The Small nozzle allowed for a higher Re_c range, but its relatively smaller jet width limited the measurements to $\alpha = 0$ deg. A photograph of the TUD-A-L case in the A-Tunnel is shown in Fig. 4a. The full measurement envelope is presented in Fig. 13.

This paper presents both aerodynamic and acoustic data from the A-Tunnel. Static pressure distributions were

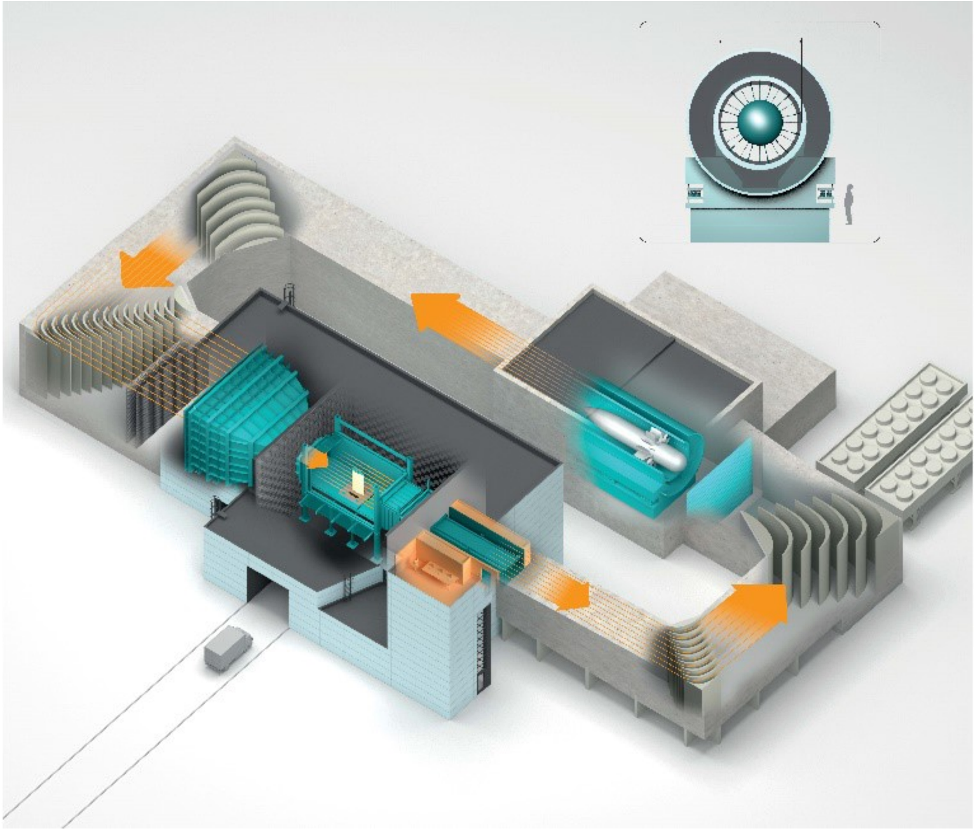

Fig. 3 The Poul La Cour Wind Tunnel.

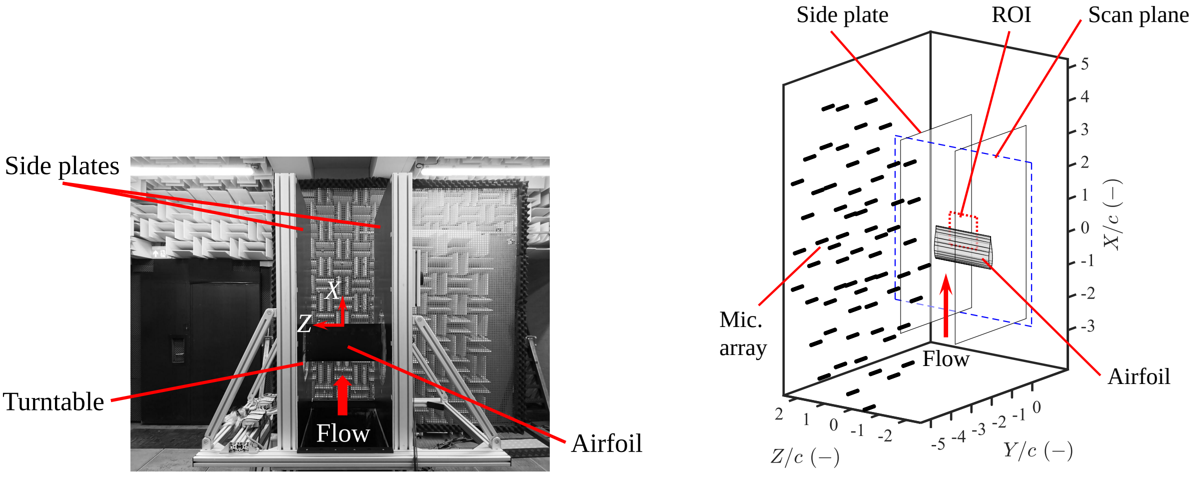

(a) **(b)**

Fig. 4 (a) The small NACA 63_3-018 airfoil in the A-Tunnel and (b) Schematic of the microphone array in the A-tunnel.

collected via Honeywell TruStability HSCDRRN025MDAA3 differential pressure transducers with a ±2.5 kPa range and ±6 Pa accuracy. Subsequently, the lift coefficients are calculated by a method described in Section IV.A.

The Hot-Wire Anemometry (HWA) Technique was employed to extract the boundary-layer velocity profiles at $X/c = -0.02$, i.e. close to the TE. Specifications of the HWA system can be found in the publication of Luesutthiviboon et al. [11].

The acoustic data was recorded using an array of 64 microphones and post-processed using conventional frequency-domain beamforming (CBF) [19]. The acoustic maps were then integrated using the Source Power Integration (SPI) technique. A schematic of the microphone array and the Region Of Integration (ROI) is shown in Fig. 4b. For more details about post-processing technique, the paper from Merino-Martinez [18] may be consulted.

C. The LTT at TU Delft

The large NACA 63_3-018 model was tested in the Low-Turbulence Tunnel (LTT) at TU Delft. The aforementioned publication of Luesutthiviboon et al. [11] also contains full details of the LTT facility, including aero-acoustic results.

The LTT is a closed-circuit wind tunnel originally designed for aerodynamic tests. The LTT has a contraction ratio of 17.8 and a turbulence intensity range between 0.015% and 0.07% for free-stream flow speeds between 20 and 70 m/s. The airfoil was installed in a specially-made test section, in which the wall panels are ‘acoustically treated’ by Kevlar-covered Melamine wedges.

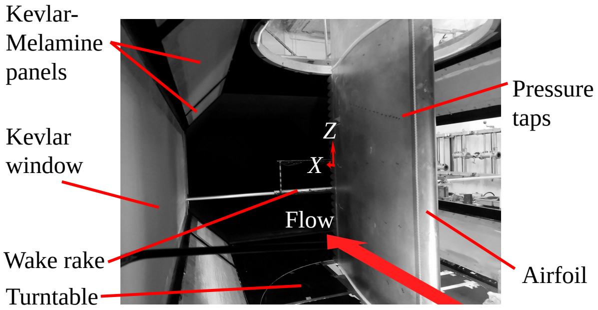

Fig. 5 The large NACA 63_3-018 airfoil in the LTT.

This paper only presents aerodynamic test results from the LTT, namely, the lift curves, and the boundary layer profiles. To read the static surface pressure data, the 101 pressure taps on the model were connected to a DTC pressure system with 6 ESP–HD scanners. The aerodynamic corrections for the LTT hard-wall test section can be found in the works of Timmer and Garner et al. [20, 21]. It has been confirmed by Luesutthiviboon et al. [11] that the pressure distribution and lift obtained in the acoustically test section do not deviate from that obtained in the hard-wall configuration. A brief comparison of both set-ups is also presented in this study.

Velocity fields at the TE region of the model were extracted by the Particle Image Velocimetry (PIV) technique. Specifications of the PIV setup can be found in the work of Luesutthiviboon et al. [11]. The edge of the boundary layer was defined where the spanwise vorticity is constant. Subsequently, the boundary layer integral parameters were extracted.

D. The AWB at DLR

The Acoustic Wind Tunnel Braunschweig (AWB) is an anechoic open-jet, closed-circuit wind tunnel operated by the German Aerospace Center (DLR - *Deutsches Zentrum für Luft- und Raumfahrt*), Braunschweig. The test section is treated with acoustic linings to reduce sound reflection in the test section. The nozzle cross-section is 0.8 m in width and 1.2 m in height, and the maximum wind speed at the nozzle is 65 m/s with a turbulence intensity of 0.3% [22]. The wind tunnel model is installed along the width of the nozzle via two side extensions of the nozzle (see Fig. 6). Two far field sound measurement systems were used extensively in the measurement campaign.

The directional microphone with a 1.4 m outer diameter elliptic reflector is placed along a motorized traversing system below and facing the model’s pressure side. At the near-focal point of the elliptical reflector is a Brüel&Kjær 4136 1/4” microphone, which records the reflected noise. The distance between the microphone to the sound source (geometrically represented by the model’s trailing edge) is approximately 1.15 m. Because the directional mirror’s insensitivity to the distance to the sound source, its height with respect to the wind tunnel center line was not adjusted [23]. Assuming line sources, the noise was measured along a straight line cutting through the mid-span of the model.

Prior to the actual measurement, a scan along the streamwise axis was performed with the directional microphone to identify the leading-edge and trailing-edge noise distribution. Furthermore, because sound is convected with the free-stream and refracted by the wind tunnel's shear layer, the measured distribution is further downstream than the position of the model. The shifted position is predominantly dependent on the freestream velocity. The result of the scan shows that each noise source has a distinct distribution, so trailing-edge noise measurement can be done within a narrow range around the shifted position of the trailing edge. From this narrow range, a maximum level was selected to represent the far field sound pressure level. The range of the baseline measurement was from -30 mm to 30 mm with 5 mm increments from the shifted trailing edge. Whereas, for the serrated trailing edge measurement from -30 mm to 60 mm with the same increments from the shifted baseline trailing edge. Noise was measured for 20 s at a rate of 65 kHz, and a high-pass filter with a cut-off frequency of 500 Hz was applied in the data acquisition. The measured time series was converted in the frequency domain using the method of averaged periodogram with 50% overlap and Hanning window. The narrowband spectral resolution was 16 Hz. The background noise, the direction microphone system response function (assuming line source distributions) were corrected according to the method of Schlinker [24]. More details on the procedure can be found in Herr [25].

The microphone array consists of 96 *LinearX* 1/2" microphones arranged within a 1 m diameter circle. It was installed above the wind tunnel model facing the suction side. Noise was measured for 30 s at a sampling rate of 100 kHz. A high-pass filter with a cut-off frequency of 500 Hz was also applied in the data acquisition of the microphone array. The measurements were processed using CLEAN-SC [16] with removal of the diagonal component of the cross-spectral power matrix and Amiet's 2D shear layer correction. The spectra were calculated using the method of averaged periodogram with 0% overlap and rectangular windows. The narrowband spectral resolution was 24.4 Hz and the level is adjusted to a reference observer at a distance of 1 m from the sound source. In order to separate the trailing-edge noise from other noise sources, the post-processing was done for a localised area around the trailing edge with a span width of 0.4 m and a chord length of 0.16 m, and the sound pressure level is considered only for sound sources identified within this area.

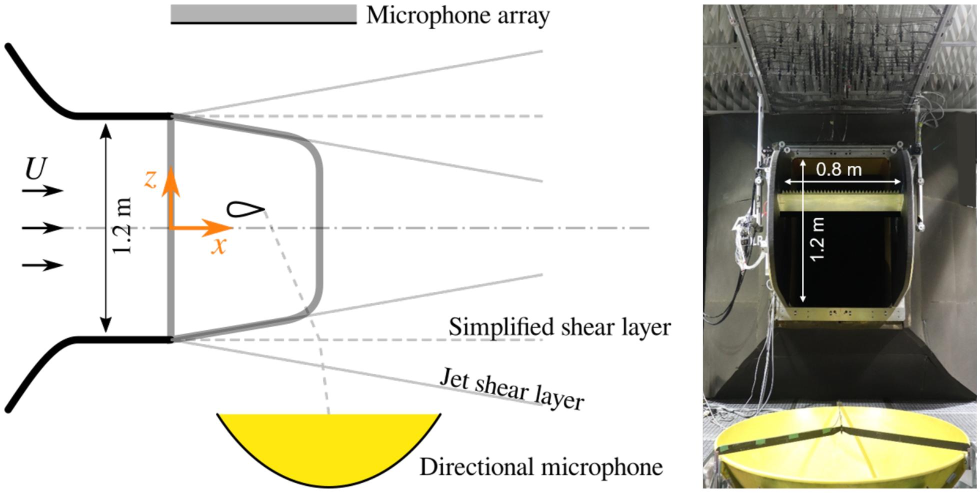

Fig. 6 AWB test set-up.

E. The NWB at Braunschweig

Aerodynamic measurements were performed in the closed test section of the Low-Speed Wind-Tunnel Braunschweig (NWB - *Niedergeschwindigkeitswindkanal Braunschweig*) of the German-Dutch Wind-Tunnels Foundation (DNW - *Deutsch-Niederländische Windkanäle*), see Fig. 7. The NWB is a closed-circuit low-speed wind tunnel that can be operated in a closed or open anechoic test section environment [26]. Its closed test section provides a cross-sectional area of 3.25 m × 2.8 m and a length of 8 m. Dedicated model extensions were built to extend the original HRM span to 2.8 m. Aerodynamic coefficients were derived from integration of the pressure distribution at midspan, cf. Section II. An additional wake rake with 135 total pressure probes (of 2.5 mm distance) and 7 static pressure probes was used on a high-resolution traversing system for drag measurements. Lift and drag polars were corrected for wall interference according to the standard procedure by Garner et al. [21], thereby neglecting compressibility effects. Arrays of 10 G.R.A.S. 48LA 1/4” surface microphones in different layouts were also applied on the HRM in the closed test section. Necessary data corrections to account for the signal averaging over the sensing area of the microphones are currently being developed and validated pior to data release. Accordingly, the current paper is limited to the presentation of first aerodynamic test data. The results from a follow-up acoustic campaign in the NWB acoustic plenum (i.e. open-jet anechoic test environment) are not yet fully post-processed and will be subject of future work in this ongoing cooperation.

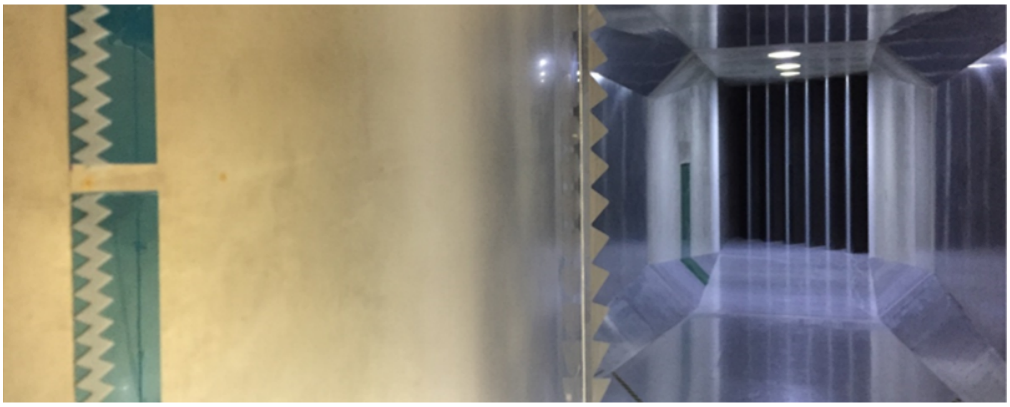

Fig. 7 NWB test set-up with tripping detail.

F. Facility summary

Table 1 provides an overview of the main characteristics of the wind tunnels used for this study. Note that the LTT and the NWB also have an aero-acoustic configuration (Kevlar panels and open-jet respectively), but aero-acoustic results from these facilities have not been used in this work.

Facility	**DTU**	**A-Tunnel** *Small/Large*	**LTT**	**AWB**	**NWB** *Closed*
Max. flow speed [m/s]	105	Small: 75 Large: 35	120	65	90
Test section [m]	3 × 2	S: 0.25 × 0.4 L: 0.7 × 0.4	1.8 × 1.25	1.2 ×0.8	3.25 × 2.8
Max. TI [%]	0.1	0.15	0.07	0.3	Long.: 0.06 Transv.: 0.15
Re_c measured ($\times 10^6$) [-]	1 - 4	S: 0.38 - 1 L: 0.18 - 0.46	1 - 3	0.38 - 0.77	1.9 - 4.8
Acoustic set-up	Kevlar walls	Open-jet	-	Open-jet	-
Aerodynamic set-up	Kevlar/Hard walls	Hard walls	Kevlar/Hard walls	Open-jet	Hard walls
Acoustic data	Mic. array, (CBF, Clean-SC)	Mic. array, (CBF)	-	Mic. array (Clean-SC) + Elliptic mirror	-
Boundary layer profiles	HWA	HWA	PIV	-	-
Airfoil model tested (span × chord [m])	HRM (2 × 0.9)	LRM (0.4 × 0.2)	HRM (1.25 × 0.9)	LRM (0.8 × 0.2)	HRM (2.8 × 0.9)
Model aspect ratio	2.22	2.00	1.39	4.00	3.11
Plot label	DTU	TUD-A-S TUD-A-L	TUD-LTT	AWB-MA AWB-EM	NWB
Plot colour	Green	Yellow Blue	Purple	Dark red Light red	Black

Table 1 Summary of the main characteristics and data retrieved from each facility.

IV. Aerodynamic Comparison

A brief aerodynamic comparison is given in this section. The lift and drag coefficients are presented in Subsection IV.A, where a comparison between tests with hard and Kevlar walls is also shown. The serrations effect on the lift curves is studied in Subsection IV.B, and finally the displacement thickness near the trailing edge is shown in Subsection IV.C.

A. Polar Curves

The lift coefficient measurements are presented in Fig. 8 for every facility, for both the clean and the tripped conditions. The C_l is obtained from the surface integral of the pressure coefficients C_p, measured by means of the surface pressure tabs described in Section II. Different wind tunnel corrections have been applied for each facility. For the A-Tunnel and the AWB measurements, which use open jet configuration, the effective angle of attack had to be corrected for distortions of the jet by the airfoil loading. A constant relation $\alpha_{eff} = K\alpha_{geo}$ was assumed, and the correction factor K was found by comparing the measured pressure distributions to XFOIL predictions [27]. The K values calculated from XFOIL were similar than the ones obtained from Brooks et al. analytical formula [28]. For the NWB, the LTT, and the DTU measurements with hard walls, the standard wind tunnel corrections according to Garner et al. have been applied [21]. DTU's Paul La Cour Tunnel measurements taken with Kevlar walls have been corrected using the methodology explained in Devenport et al. [15, 29], which is based on potential flow methods that take into account the wall presence including the flow transpiration through the Kevlar membranes. Details of this correction and a validation with Virginia Techical Unveristy can be found in the study of Fischer et al. [12]. The different nature of these corrections is represented in the polar plots, since using XFOIL for the corrections leads to the results matching a pre-defined set of polars. The measures corrected with XFOIL are shown with empty markers, whereas the other methods are plotted with filled markers.

In the LTT and the DTU campaigns, the aerodynamic coefficient have been measured with both hard walls and Kevlar walls. A comparison of such measurements is given in Fig. 10. In the rest of figures, the measurements taken with Kevlar walls have been used.

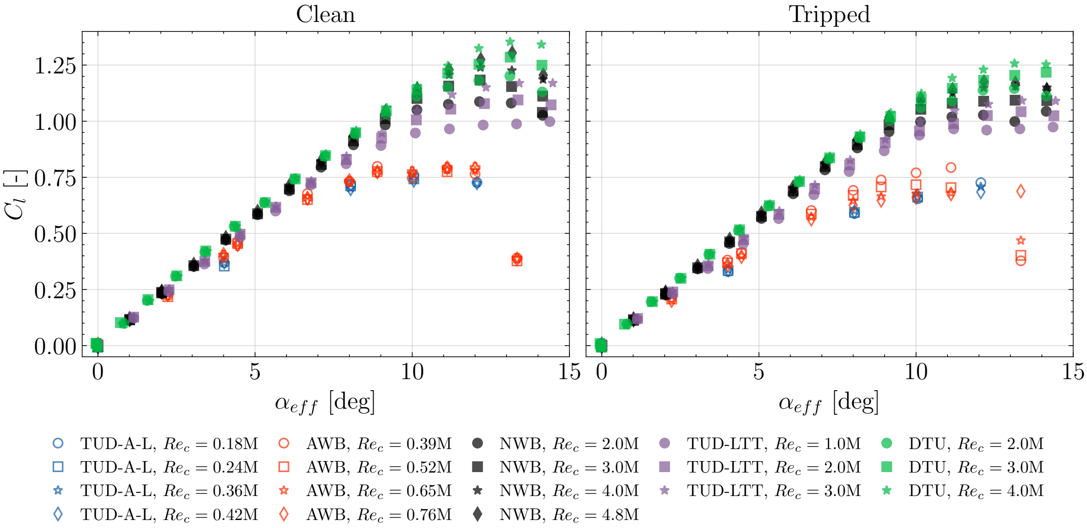

Fig. 8 Lift coefficient measured in the different facilities for a variety of Re_c numbers. Empty markers represent the measures corrected using XFOIL, and full markers indicate other correction methods.

The Reynolds number effect is clearly visible in Fig. 8. The measurements at the A-Tunnel and the AWB, at significantly lower Re_c than the other ones, show a reduced $C_{l,max}$ and an earlier onset of separation. There is a good agreement between both facilities with a slight difference in the slope in the linear region, which could be caused by the different aspect ratio in the tests (2 in the A-Tunnel, 4 in the AWB). A higher aspect ratio can lead to a increase in the lift coefficient slope [30]. The trend with Re_c in the stall region observed for the AWB measurements with tripped conditions appear to be the opposite as expected. The free transition point, as calculated with XFOIL, coincides with the position of the tripping device on the suction side. This possible interference is suspected as the source of such trend, but it has not been investigated further. A laminar separation bubble is observed for both the A-Tunnel and the AWB clean measurements, but it does not appear at higher Re_c. In the tripped case, the measured C_p are very similar and aligned with the XFOIL predictions. The C_p distributions are not shown here for conciseness. For the HRM results, a good agreement is observed specially between DTU and NWB, the former showing a slightly higher $C_{l,max}$ for the equivalent Re_c. This higher $C_{l,max}$ may be influenced by the use of Kevlar walls, as visible in Fig. 10. The LTT data has a lower slope which again could be attributed to a reduced aspect ratio and the pressure tabs not being in the middle of the test section. The different inflow turbulence of the tunnels could also play a role. Higher $C_{l,max}$ are measured in the clean cases, and the separation behaviour appears to be sensible to Re_c than in the tripped counterpart (except for the AWB as discussed above).

The drag coefficient results are shown in Fig. 9. All the data has been obtained from the momentum deficit in the wake using wake-rake measurements, as described in Section 7.2.3. of Russo [31]. As Re_c increases, C_d decreases, as seen very clearly by the difference between the models. In addition, larger drag values are observed in the tripped case compared to the clean measurements.

Fig. 10 compares the measurements in the LTT and the PLCT (DTU) for Kevlar and hard walls. The LTT data shows a very good agreement between both configurations at positive α_{eff}. However, a mismatch is observed at negative stall. The cause is an asymmetry in the test set-up with Kevlar walls. One side of the test section (facing suction side at $\alpha > 0$) was a Kevlar-Melamine panel with a solid back plate for noise absorption, whereas the opposite side was composed of a single Kevlar panel to allow for the acoustic measurements. Further details and consequences of the asymmetric permeability are explained in the study of Luesutthiviboon et al. [11]. DTU results also agree well, with the hard walls leading to a slightly lower $C_{l,max}$. The hard wall measurements were carried out with tripping at 5% in the suction side and 10% in the pressure side, unlike the Kevlar case, which was tested at symmetric 5% tripping. However,

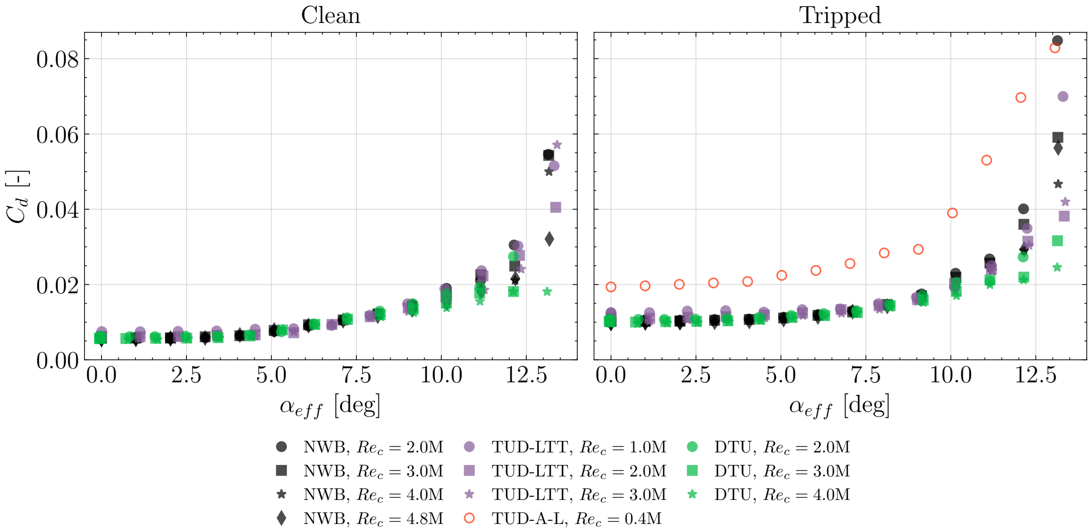

Fig. 9 Drag coefficient measured in the different facilities for a variety of Re_c numbers. Empty markers represent the measures corrected using XFOIL, and full markers indicate other correction methods.

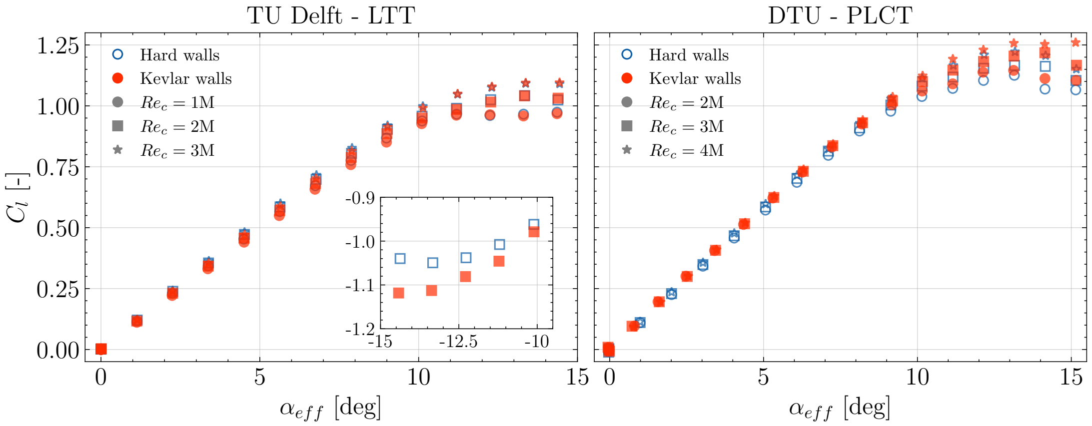

Fig. 10 Comparison of the lift coefficient curves measured in Kevlar and hard wall configurations at the Poul La Cour Tunnel (DTU) and the Low Turbulence Tunnel (LTT). The boundary layer was tripped in all the cases. Inner axis in the LTT plot shows negative stall behaviour.

it is considered that the trends appearing in the plot are the consequence of the different walls and not the tripping, since the same trends are found in the clean case.

B. Polar Curves - Serrations Effect

The serrations effect on the lift coefficient is presented in Fig. 11. The lift coefficient difference is calculated as $\Delta C_l = C_l - C_{l,ref.}$, where $C_{l,ref.}$ corresponds to the equivalent α_{eff} with straight trailing edge. Hence, positive ΔC_l values indicate increase in the lift coefficient when serrations are in place. The serrations installation in the HRM blocked the pressure tabs closest to the trailing-edge on both sides of the airfoil. Therefore, the results are not as accurate as in the baseline case, and are biased with respect to it. The general trends are still captured. Both geometries show positive ΔC_l because C_l has been calculated with the same reference chord but the serrations feature extended surface area. Higher ΔC_l is observed for iron serrations compared to the sawtooth ones, which is also attributed to a comparably larger surface area. The iron case also shows a higher sensibility with α_{eff}. Due to uncertainties in the installations the serration flap angles were higher than nominal in the DTU-PLCT tests ($\sim$ 4 deg.). It explains why the difference in ΔC_l

is larger than in the other tunnels. It is interesting to note that the same trends are also found in this case, but with an offset in ΔC_l.

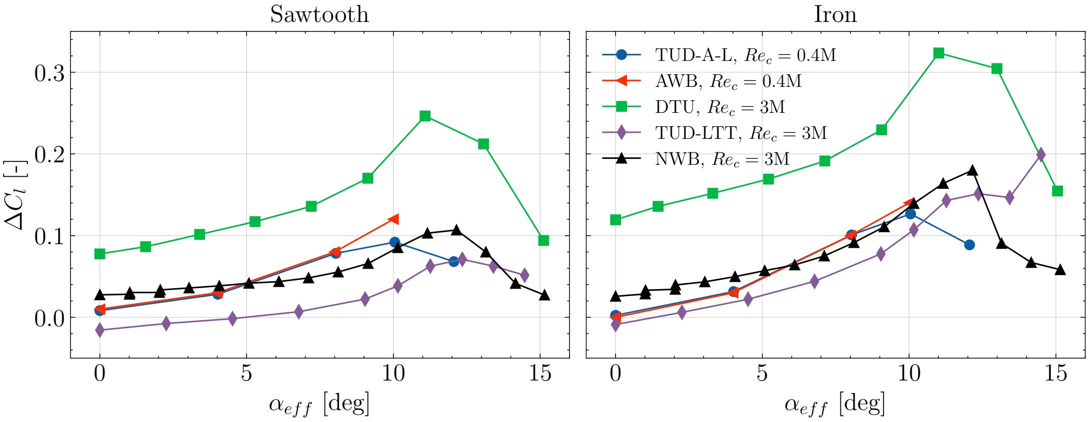

Fig. 11 Increase of lift coefficient with iron and sawtooth serrations measured at the different facilities. It was measured that DTU serrations were flapped 4 deg. instead of the nominal $\varphi = 0$ deg.

C. Displacement Thickness near the Trailing-Edge

The boundary-layer velocity profiles in the vicinity of the trailing edge were measured. HWA was used in the PLCT (DTU) and in the A-Tunnel (TU Delft), and PIV was employed in the LTT (TU Delft). The HWA measurements were performed at $X/c = -0.02$. Once the velocity profiles were obtained, the boundary-layer parameters were extracted. The location of the boundary-layer thickness and the edge velocity were determined by the region were the velocity fluctuations became constant, and fitting of the logarithmic layer was employed [32]. The work of Luesutthiviboon et al. [11] describes in detail the results obtained at TU Delft.

The boundary-layer displacement thickness (δ^*) is of special interest. It will be the parameter chosen to represent the turbulence length scale when scaling the acoustic results in Section V.D, following the classic scaling of Brooks et al. [33]. The measurements are presented in Fig. 12 for $\alpha_{eff} = 0$ deg and straight trailing edge. The lines show the XFOIL predictions obtained with 250 panels and $N_{crit} = 9$. This amplification factor has been chosen after comparing the C_p predictions with the measurements. Dashed lines represent the predictions for the LRM, and solid lines the HRM ones (to account for the different Re_c/M_U relation). Great accordance with XFOIL is observed in the HRM measures. The discrepancies are larger in the LRM, likely a result of a lower measurement resolution near the wall due to a very thin boundary layer. XFOIL captures well the general trends in terms of Re_c and tripping effect. It will be used to calculate δ^* for the scaling of the acoustic results given the lack of data for the rest of test conditions.

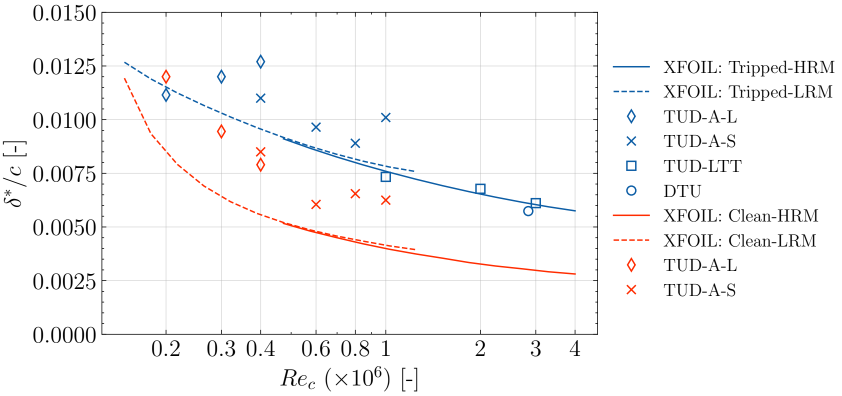

Fig. 12 Displacement thickness measured in the different facilities as a function of Re_c. Blue lines and markers correspond to the tripped boundary-layer conditions, whereas the clean cases are indicated with red.

V. Acoustic Comparison with Straight Trailing Edge

The far-field acoustic measurements with straight trailing-edge are compared in this Section. A summary of the data is firstly given in Fig. 13. The effect of the Reynolds number and the tripping is presented in Subsection V.A, the impact of the angle of attack is assessed in Subsection V.B, and the differences between facilities and measurement techniques are checked in Subsection V.C. Finally, the measurements are scaled together to the same conditions in Subsection V.D, and the collapse is studied. A reference pressure of 20 μPa is used to express the acoustic data with the Sound Pressure Level (SPL).

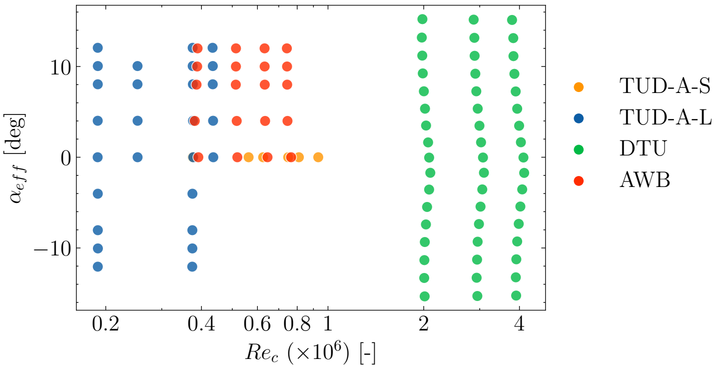

Fig. 13 Summary of the acoustic data for the baseline configuration with tripped boundary layer.

The broad Re_c range measured is shown in Fig. 13. The measurements carried out in the AWB and the A-Tunnel used the LRM, whereas the HRM was tested in the PLCT (DTU). In the lower Re_c range there are several overlapping points which allow for direct comparison between facilities. The geometrical angles of attack in the AWB and the A-Tunnel have been chosen such that their effective angle of attack are equivalent.

A. Effect of the Reynolds Number and the Tripping of the Boundary Layer

Fig. 14 presents the measured SPL in 1/3 octave bands in every facility for the straight trailing edge. Different Re_c numbers are presented together, and the tripped and clean cases are compared. All the results are normalised to a span width and an observer distance of 1m.

The forced transition effect is visible in all the facilities. The turbulent boundary layer arising from the tripping leads to a thicker δ^* than its clean counterpart, as shown in the HWA and PIV measurements presented in Fig. 12. This creates a noise increase in all the cases presented, which is found to be more important at low frequencies, and larger for increasing Re_c. The two lowest Re_c measured (0.19×10^6 and 0.25×10^6) are not following this pattern, and show larger $SPL_{1/3}$ for the clean case. The displacement thickness measurements shown in Fig. 12 indicate that δ^* may be higher for the clean case at the lowest Reynolds numbers.

DTU measurements (Fig. 14b) and AWB measurements carried out with the elliptic mirror (Fig. 14d) show a high-frequency peak. The location of the peaks scales to very similar trailing-edge thickness based Strouhal numbers $St_{t_{TE}} = ft_{TE}/U$. This suggests that the cause of the peaks is trailing-edge bluntness noise [33]. The same phenomena would be also visible in the A-Tunnel and the array measurements in the AWB if the high frequency limit was larger. In the AWB case, the peaks are more clearly visible in the clean case. It could be explained by a major distortion of the vortex shedding from the turbulent boundary layer developed in the tripped case.

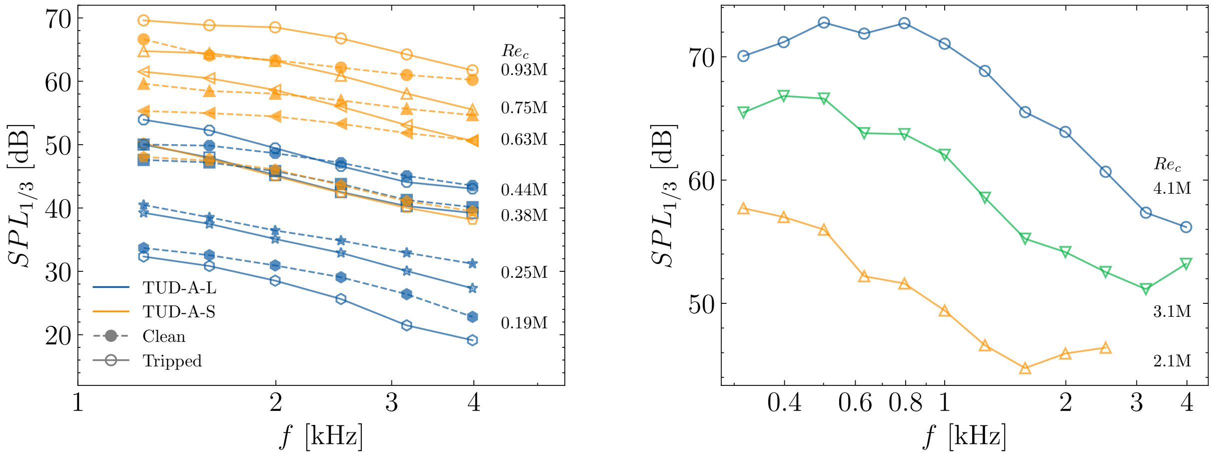

(a) TUD-A-Tunnel measurements.

(b) DTU-PLCT measurements.

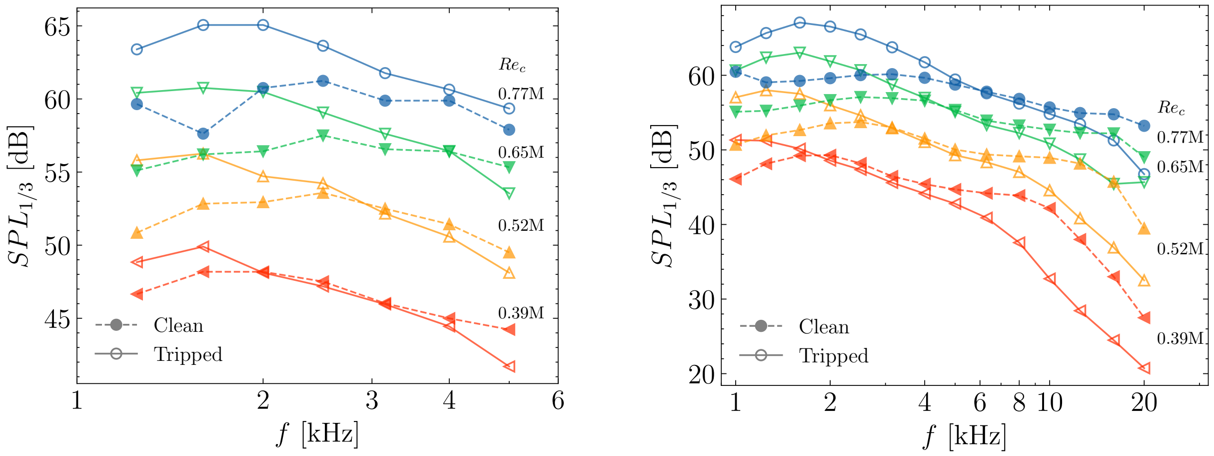

(c) DLR-AWB measurements with microphone-array.

(d) DLR-AWB measurements with elliptic-mirror.

Fig. 14 Effect of the Reynolds number and the tripping in the trailing-edge noise measurements of the different facilities. Solid lines with empty markers represent the tripped conditions, and dashed lines with full markers indicate the clean equivalent.

B. Effect of the Angle of Attack

The acoustic polars, presented in Figs. 15 and 16, give a general overview of the angle of attack effect on the trailing-edge noise. The Overall Sound Pressure Level ($OSPL$) has been calculated from the 1/12 octave band spectrum, adding the bands between 1.2 kHz and 5 kHz. This range has been chosen since it contains the common f values for the LRM. These $OSPL$ values should only be analysed comparatively between the different cases to check that the trends are the same, but they do not represent the total $OSPL$ since the peak location of the spectrum is likely located at lower frequencies, specially for non-zero α_{eff}. To allow for similarity between different conditions, the $OSPL$ has been scaled according to the classical law [33]:

$$OSPL_{scaled} = OSPL - 50\log_{10}(M_U/M_{ref}) - 10\log_{10}(\delta^*_{SS}/\delta^*_{ref}) - 10\log_{10}(b/b_{ref}) - 20\log_{10}(r_{ref}/r) \quad (1)$$

Where M_U is the Mach number based on the free-stream velocity, δ^*_{SS} is the boundary-layer thickness at the suction side, b is the span of the trailing edge, and r is the observer distance. The subscript $_{ref}$ indicates the reference quantities of the scaling, which are chosen as $M_{ref} = 0.13$, $\delta^*_{ref} = 0.008$ m, $b_{ref} = 1$ m, and $r_{ref} = 1$ m.

Fig. 15 compares the trends found in the LRM measures. A good alignment between facilities is observed. For the tripped conditions, the $OSPL$ decreases with α_{eff} and increases with Re_c. The effect of the angle of attack is attributed to the change introduced in the spectral shape: the level increases at low f and decreases at high f, and hence the frequency range selection for the $OSPL$ calculation determines the tendency. The change in the spectral shapes is further discussed in Fig. 17. The trend with Re_c could be explained similarly. The takeaway here is that it is consistent between facilities and with the qualitative expectations. The $OSPL$ at $Re_c \approx 0.4 \times 10^6$, the overlapping point for both facilities, agree within 2 dB. For the clean cases, the same trend with the angle of attack is observed except at $\alpha_{eff} = 8$ and 10 deg. In these cases, the presence of tones from laminar boundary layer instability noise lead to a $OSPL$ increase. These tones may be seen in Fig. 19, where the noise power spectral density is presented. There is also a good agreement in the Re_c at which this phenomena is observed.

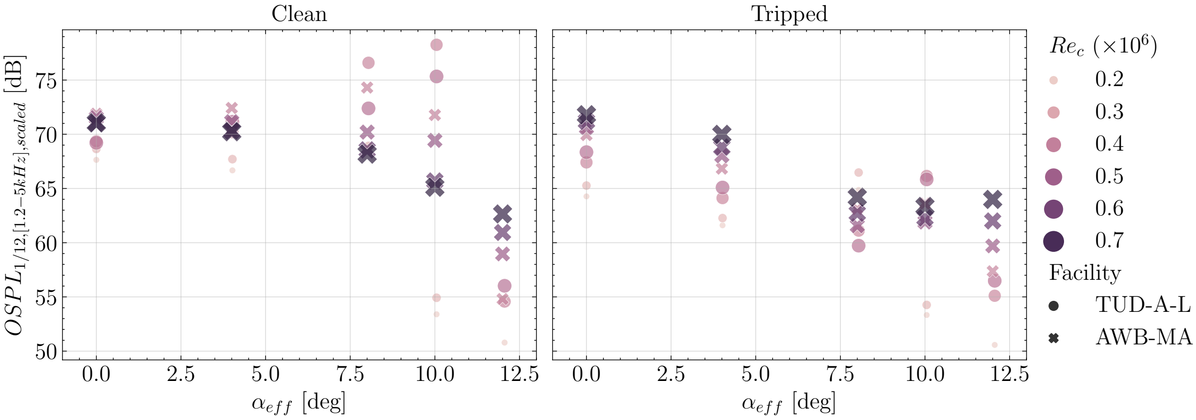

Fig. 15 Acoustic polars of the Low Reynolds number Model measured at A-Tunnel and the AWB for the baseline configuration and both tripped and clean boundary layer.

In Fig. 16 the acoustic polars measured at DTU for the tripped case are shown. The same trends with respect to the angle of attack and the Reynolds number are observed. In this case, the frequency range in the $OSPL$ calculations is 0.4 kHz to 5 kHz, since the Clean-SC post-processing allowed for a better resolution in the low frequency range. A Strouhal-based definition of the integration bounds would have allowed for direct comparison between the LRM and the HRM results. However, due to large Re_c range of the measurements, there is not enough overlapping part of the spectrum in the St space.

Fig. 17 shows the angle of attack effect on the spectra. Different α_{eff} are plotted together for the same Re_c for each facility. Both clean and tripped cases are presented. In the DTU measurements (Fig. 17b) a noise increase at lower frequencies is observed, accompanied by a noise reduction at higher frequencies. This is accredited to a thicker boundary layer developed in the suction side. In the other facilities only the noise reduction at high frequencies is observed due to the lack of low frequency data. From the AWB elliptic mirror data (Fig. 17d) the very high frequency results can also be studied. At $f > 8$–10 kHz, the levels increase again with the angle of attack. This could be attributed to higher energy content in the thinner pressure side boundary layer at these frequencies. The clean cases show the presence of tones at $\alpha_{eff} = 4$ and 8 deg, more clearly visible in the PSD plot shown in Fig. 19.

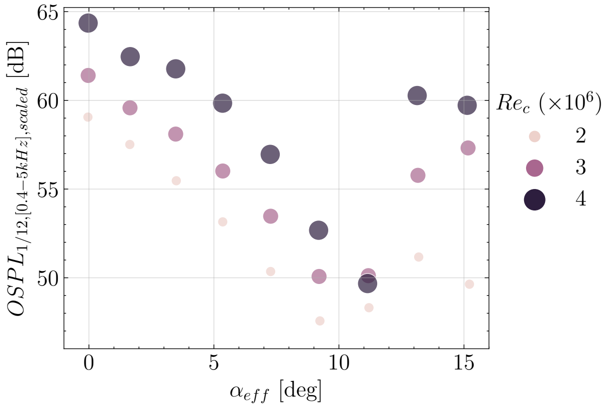

Fig. 16 Acoustic polars of the High Reynolds number Model measured at DTU-PLCT for the baseline configuration and tripped boundary layer.

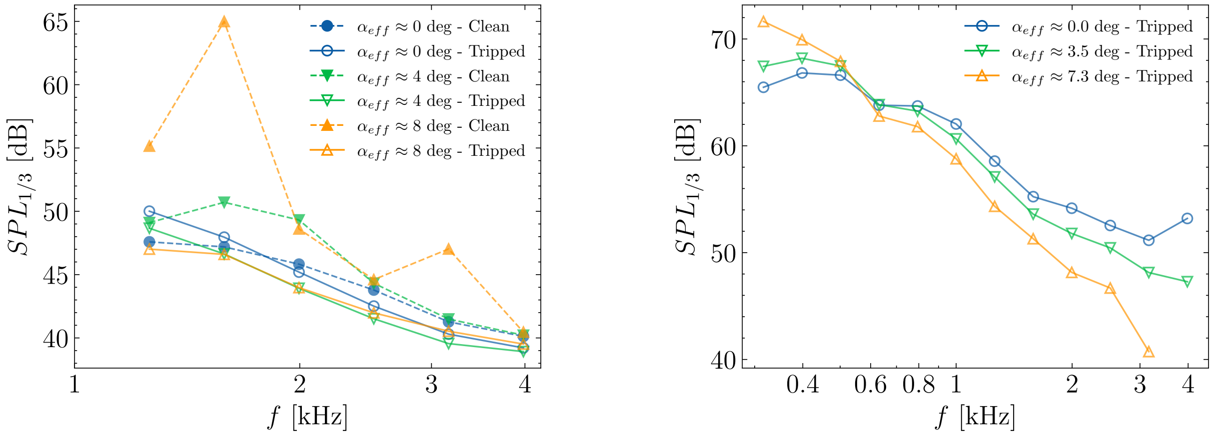

(a) TUD-A-Tunnel measurements at $Re \approx 0.38 \times 10^6$**.**

(b) DTU-PLCT measurements at $Re \approx 3 \times 10^6$**.**

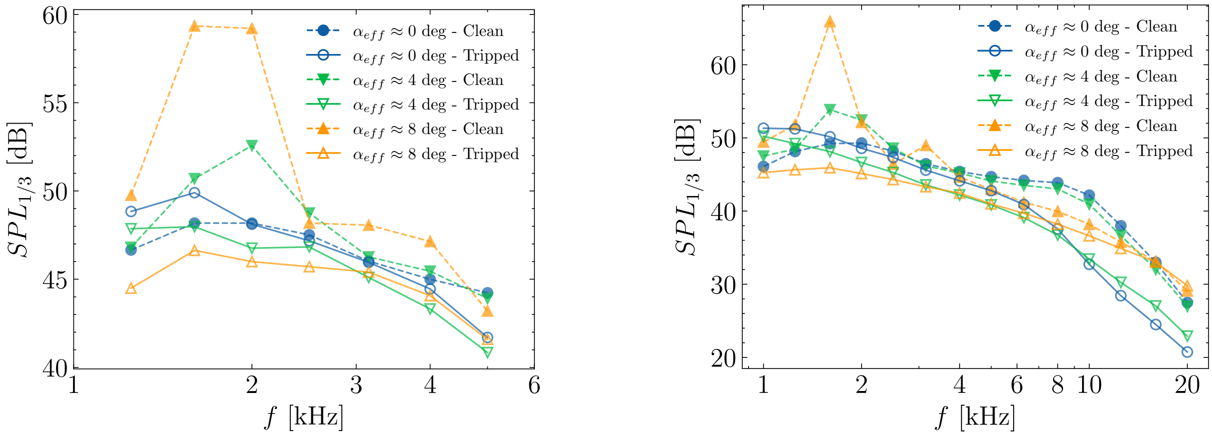

(c) DLR-AWB measurements with microphone-array at $Re \approx 0.39 \times 10^6$**.**

(d) DLR-AWB measurements with elliptic-mirror at $Re \approx 0.39 \times 10^6$**.**

Fig. 17 Effect of the angle of attack and the tripping in the trailing-edge noise measurements of the different facilities. Solid lines with empty markers represent the tripped conditions, and dashed lines with full markers indicate the clean equivalent.

C. Effect of the Facility and the Measurement Technique

The overlapping measurement point at $Re_c \approx 0.38 \times 10^6$ between the A-Tunnel and the AWB is now studied. The acoustic data is presented using the power spectral density.

In Fig. 18, the case at $\alpha_{eff} = 0$ deg shows a very good agreement between the two nozzles of the A-Tunnel. This allows both set-ups to be interpreted together in a continuous way. The two measurement techniques used in the AWB also collapse very well. Such results strengthen the consistency of the data. The peak levels of both facilities are virtually equal, but a mismatch in the spectral slope leads to deviations up to 6 dB at higher frequencies. There is still a difference in the post-processing used in each facility. It would be interesting to study the possible scatter introduced by using different beamforming algorithms, and establish a common post-processing method. Differences in the shear layer correction can also lead to a deviations in the spectral slope.

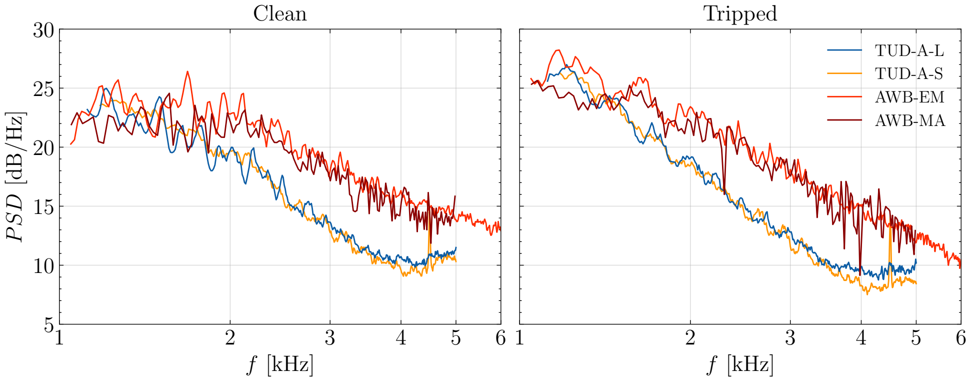

Fig. 18 Far-field noise power spectral density measured at the A-Tunnel and the AWB at 30 m/s for the baseline configuration with tripped boundary layer and $\alpha_{eff} = 0$ deg.

At $\alpha_{eff} = 8$ deg (Fig. 19), the presence of the laminar boundary-layer feedback-loop tones is clearly visible in the clean case. The small mismatch in the peaks location between the AWB and the A-Tunnel may correspond to deviations in the dynamic pressure or more likely to different development of the boundary layer attributed to the distinct aspect ratio, as observed previously in the small discrepancies in the polar curves (Fig. 8). Minor differences are also now observed between the elliptic mirror and the microphone array data from the AWB. The likely reason is the different directivities measured with each system, since the equipment are located at either side of the airfoil as depicted in Fig. 6. The elliptic mirror data will be taken for the subsequent comparisons. It does not only have a broader f range, but it is also consistent with the other facilities, which have the measurement system facing the pressure side of the airfoil when the model is pitched towards positive angles of attack.

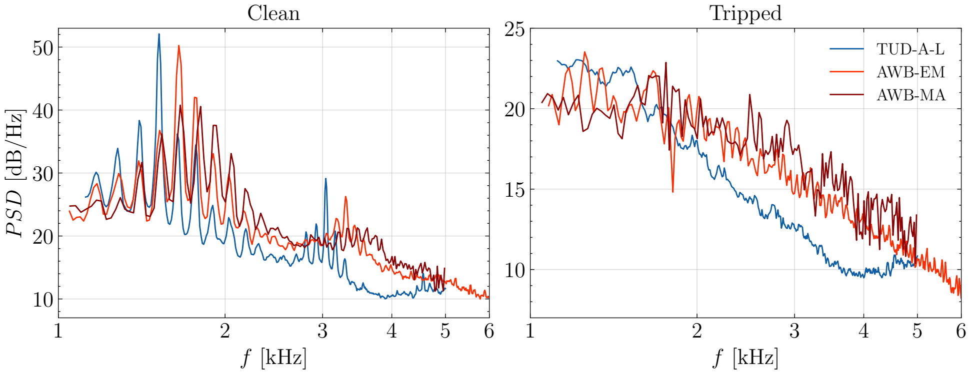

Fig. 19 Far-field noise power spectral density measured at the A-Tunnel and the AWB at 30 m/s for the baseline configuration with tripped boundary layer and $\alpha_{eff} \approx 8$ deg.

D. Scaling Study

This section studies the collapse of the scaling of the measurements performed at different Reynolds and Mach numbers. The classic scaling law has been applied [33]:

$$SPL_{scaled} = SPL - 50\log_{10}(M_U/M_{ref}) - 10\log_{10}(\delta^*_{SS}/\delta^*_{ref}) - 10\log_{10}(b/b_{ref}) - 20\log_{10}(r_{ref}/r) \quad (2)$$

Although this form of scaling is not expected to provide a perfect collapse in all the frequency range [34], it is the most widely used form, and it provides a useful first approach to compare and study the data. Only the forced transition cases are compared here, since the test conditions are more equivalent across the different facilities and the uncertainty is reduced. To have an estimate of the peak location of the measurements, the range of expected peaks $St_{\delta^*_{SS}}$ according to BPM [33] are plotted together with the measurements. Although the model was developed using a different airfoil and measurement techniques, it is depicted here as a rough reference to know where the peak frequency may lie.

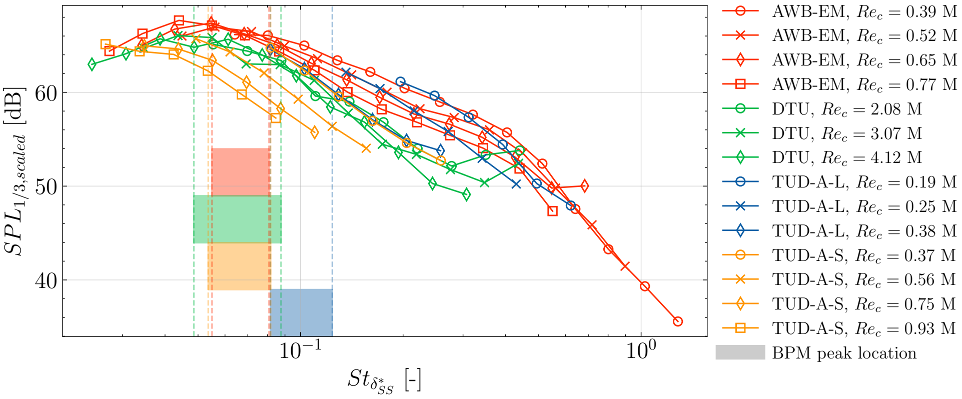

Fig. 20 Scaling of the measurements at different facilities for the tripped boundary layer case at $\alpha_{eff} = 0$ deg. The peak location predicted by the BPM model is also presented with vertical lines. Each colour covers the measurement range from the respective facility.

The scaled spectra at $\alpha_{eff} = 0$ deg. is presented in Fig. 20. According to the BPM predictions, the peak St_{δ^*} lies within the measured range. Good agreement in the peak locations and levels is observed between AWB and DTU despite deviations in the spectral slope. A trend with the Reynolds number is also observed: the curves shift to lower St_{δ^*} as Re_c increases. It is aligned with the BPM measurements, which estimated the peak St_{δ^*} as $St_{\delta^*} = 0.02M^{-0.6}$. This is particularly pronounced for the TUD results, which cover a much more extended peak Strouhal range than the corresponding BPM predictions. The mismatch between AWB and TUD, which encompass the same M_U and Re_c range, is not clear and should be investigated further. The effect of the different post-processing is suspected and should be assessed.

Fig. 21 shows the scaled spectrum at α_{eff} between 3 deg and 4 deg. The peak values agree well within 1.5 dB. As $St_{\delta^*_{SS}}$ increases, however, the collapse worsens and the scatter grows up to 10 dB. In that region, the same trend as the $\alpha_{eff} = 0$ deg is observed: within each facility, the lower the Re_c the higher the scaled SPL. This is specially visible for the two lower Re_c (0.19 and 0.25 million) measured in the A-Tunnel. The different Re_c may change the nature of the flow field and the behaviour of the boundary layer, which decreases the scaling collapse. This effect is found to be more important at the lower Re_c numbers. The large Re_c measurements performed at DTU escape this trend and show a more stable collapse.

The cases at α_{eff} between 7 deg and 8 deg are plotted in Fig. 22. The scatter between the DTU and the AWB results at low frequencies is larger in the preceding cases. Looking back at the lift curves (Fig. 8) it is observed how the loading difference is already important at this polar region. Different noise results are also expected in such a case. The better agreement between the A-Tunnel and the AWB, which polar curves are more alike, also supports this argument. The cases at $Re_c = 0.19 \times 10^6$ and 0.25×10^6 in the A-Tunnel are not shown in this plot, since the tripping effect was jeopardised by the location of the stagnation point, and laminar boundary-layer instability tones appeared.

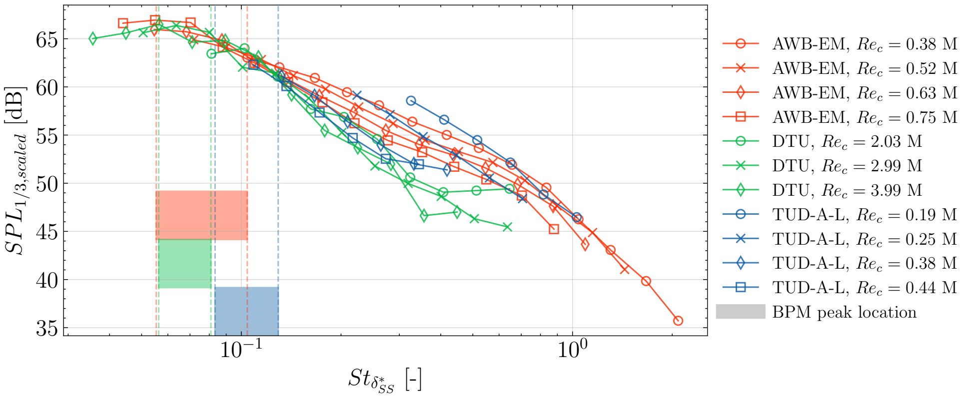

Fig. 21 Scaling of the measurements at different facilities for the tripped boundary layer case at $\alpha_{eff} \approx$ 3–4 deg. The peak location predicted by the BPM model is also presented with vertical lines. Each colour covers the measurement range from the respective facility.

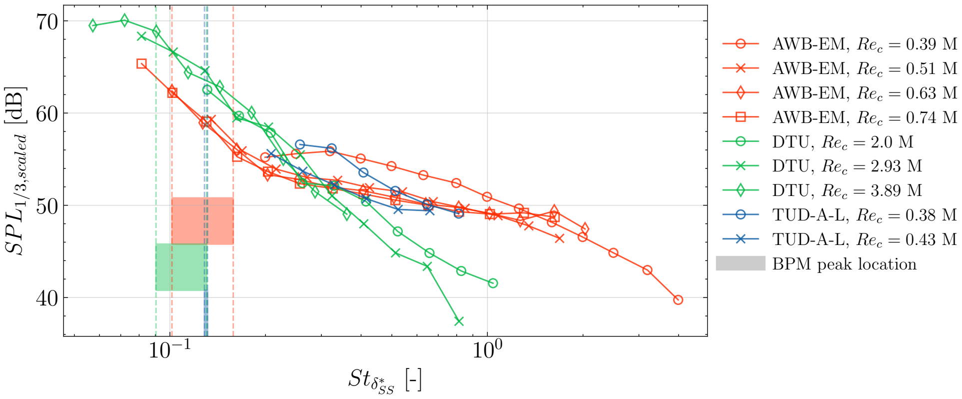

Fig. 22 Scaling of the measurements at different facilities for the tripped boundary layer case at $\alpha_{eff} \approx 7-8$ deg. The peak location predicted by the BPM model is also presented with vertical lines. Each colour covers the measurement range from the respective facility.

VI. Noise Reduction Comparison with Different Serrations

The effect of the noise reduction devices is studied in this Section. The noise reduction is calculated as $\Delta SPL_{1/3} = SPL_{1/3} - SPL_{1/3,\text{ ref.}}$, where the reference Sound Pressure Level $SPL_{1/3,\text{ ref.}}$ corresponds to the equivalent case with straight trailing edge at the same α_{eff} and Re_c. Therefore, negative $\Delta SPL_{1/3}$ indicate noise reduction. For this section, the DTU results have been post-processed with conventional frequency-domain beamforming instead of Clean-SC. The latter had convergence issues at low frequencies for the serrated cases, where the signal-to-noise ratio is lower. The CBF results show increased levels with respect to the Clean-SC equivalent [17], but this is acceptable in this section since the focus is on $\Delta SPL_{1/3}$.

$\Delta SPL_{1/3}$ is presented against $St_{\delta^*_{SS}}$ in Fig. 23 for the iron and sawtooth serrations without nominal flap angle. Only the tripped boundary layer cases are considered here. There is a fair scaling with $St_{\delta^*_{SS}}$, which supports previous results that showed that the noise reduction maximum depends on U [35, 36]. Two regions of noise reduction are identified for both serrations in the LRM results (AWB and TUD-A) The second noise reduction peak is similar to the results of P. Zhou et al. [37], which were also measured at similar Re_c number as the LRM. The HRM measurements (DTU) show two noise reduction regions in the sawtooth case, but only one in the iron case. The reason for the difference needs to be further investigated with additional measurements at high Reynolds number. At this point we cannot rule out that the noise reduction mechanisms behave differently at high Reynolds numbers. [37] found that this second peak was highly dependant on the serration flexibility and the flow alignment. The serration deformation was dependant not only on the stiffness and flow speed but also on the aerodynamic loading, which is directly related to the serration geometry. The aerodynamic forces on the flap are much higher for the HRM compared to the LRM. Hence, it is possible that the flaps were subject to small scale vibrations due to the flexibility. Small scale vibrations could counteract the noise benefits in the high frequency range. Additionally, the iron shaped serrations have a larger surface area but the same thickness as the sawtooth serrations. Hence, the ratio of the aerodynamic forces to the flap stiffness is less favourable for the iron shaped serrations than the sawtooth serrations. The uncertainty in the serration flap angle could also play a role in the mismatch. In the first noise reduction peak, the iron serrations lead to a noise decrease up to 7.5-8 dB, whereas reductions up to 5 dB are seen for the sawtooth serrations. This is aligned with the computational studies by Avallone et al. [13].

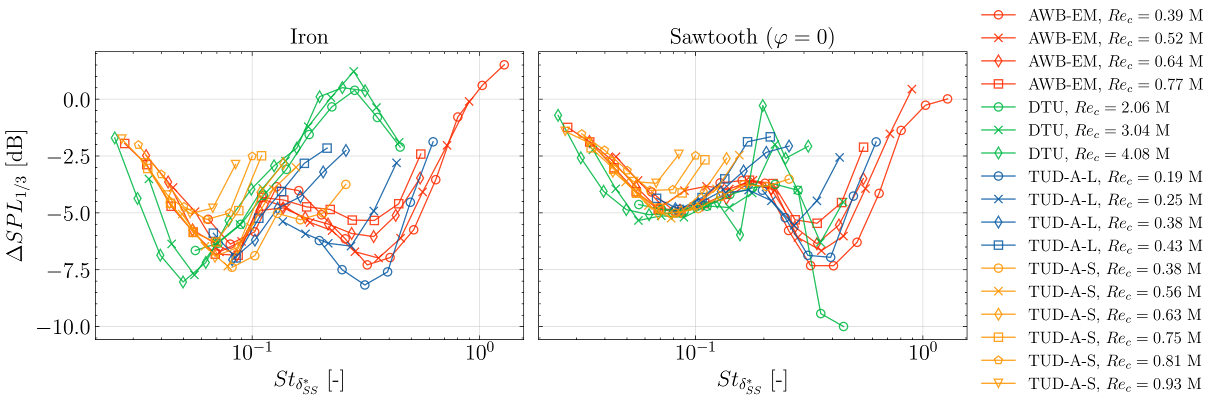

Fig. 23 Scaling of the $\Delta SPL_{1/3}$ with iron and sawtooth serrations with the displacement thickness based Strouhal number at $\alpha_{eff} = 0$ deg.

The cases with flapped serrations are shown in Fig. 24. Two noise reduction region are also identified here. The noise reduction maximum (∼ 4 dB), however, is lower than in the preceding cases. This may be explained with appearing counter-rotating streamwise-oriented vortices in the serration edges when the airfoil is loaded [38, 39], since the airfoil is actually cambered when tested with flapped serrations.

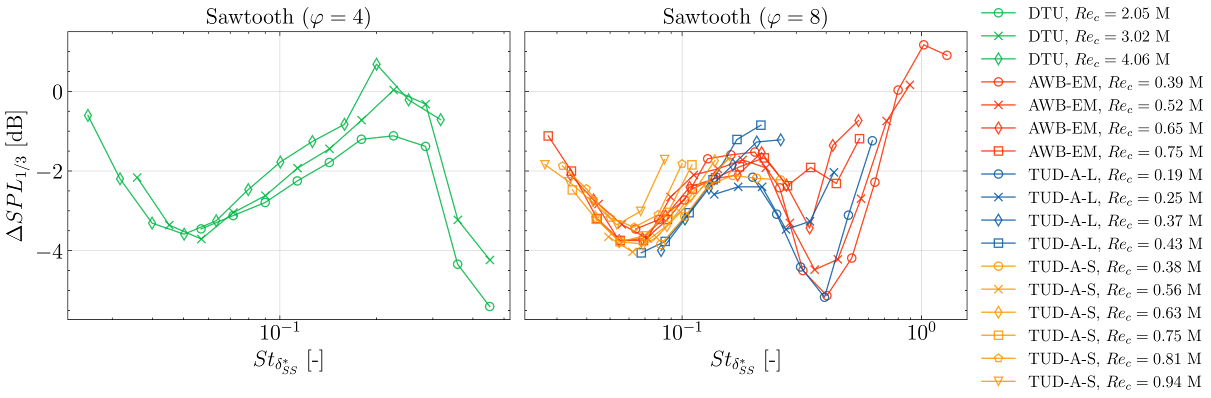

Fig. 24 Scaling of the $\Delta SPL_{1/3}$ with flapped sawtooth serrations with the displacement thickness based Strouhal number at $\alpha_{eff} = 0$ deg.

The effect of the angle of attack is summarised in Fig. 25. The $\Delta OSPL$ has been calculated for frequencies between 1200 and 5000 Hz for the LRM ($Re_c \approx 0.38 \times 10^6$), and between 400 and 3000 Hz for the HRM ($Re_c \approx 3 \times 10^6$). These values are arbitrarily chosen to have the best possible representation of the low frequencies, which drive the $OSPL$. Ideally, the same f or St range would have been chosen, but the present case is limited by the low SNR in the LRM results at low frequencies. Comparison between the models should be then analysed with care due to this difference. The noise reduction is presented for both the clean and the tripped cases. For the clean conditions, it is interesting to note the additional noise reduction measured at $\alpha_{eff} = 4$ and 8 deg. This noise decrease comes from the removal of the laminar boundary-layer instability noise. It follows the study of [40], and it is attributed to bypass transition near the trailing edge that prevents separation, and removes the amplifier of the Tollmien-Schlichting waves.

For the tripped conditions, it is observed in the spectra (omitted for conciseness) that the angle of attack initially leads to a level increase at intermediate and high frequencies. This effect propagates to lower frequencies too when α_{eff} increases further, and it affects all the spectrum when stall is reached. This may be attributed again to the increasing airfoil loading, with the same reasoning explained previously for the flapped serrations. In Fig. 25 the Re_c effect is also observed. The earlier departure of the LRM cases from the attached polar region leads to noise increases at lower α_{eff} than in the HRM results. The larger slope observed for the iron serrations shows again a higher sensibility to the aerodynamic loading due to the increased surface area, as seen previously in the lift coefficient measurements (Fig. 11).

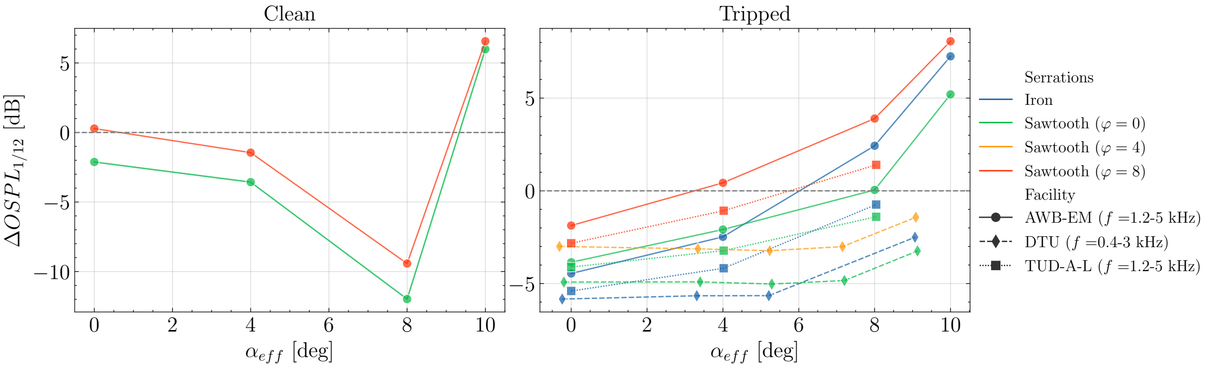

Fig. 25 Overall Sound Pressure Level as a function of the angle of attack and the serration type. LRM data (AWB-EM and TUD-A-L) measured at $Re_c \approx 0.38 \times 10^6$, and HRM data (DTU) at $Re_c \approx 3 \times 10^6$. The frequency range for the calculation of the $OSPL_{1/12}$ is indicated in the facility legend.

VII. Conclusion

The aerodynamic and aero-acoustic characterisation of the NACA 63_3-018 has been presented in this paper. Two models of this airfoil have been built for such purpose, with chord lengths of 0.2 m and 0.9 m, and they have been measured in 5 different wind tunnels: the A-Tunnel and the LTT at TU Delft, the Poul La Cour Tunnel at DTU, and the AWB and the NWB at DLR. The Re_c of the measures ranges from 0.18×10^6 to 4.8×10^6. Multiple angles of attack have been tested. The models have been studied with tripped and clean boundary layer, and sawtooth and iron serrations have also been installed and measured in both models.

The aerodynamic coefficients have been presented for the clean and tripped configurations for different Re_c. Tripping the boundary layer leads to a decrease of $C_{l,max}$ and a lower Re_c sensitivity in the stall region. Increasing Re_c leads to an increase of $C_{l,max}$ for both the clean and tripped case. This effect is very visible between models. Slight deviations in the lift slope were attributed to different aspect ratios. The effect of using Kevlar or hard walls for the testing has been also assessed. Good agreement between both configurations was observed, except for the negative stall region in the LTT measurements, which is the consequence of asymmetries in the set-up. The effect of the serrations on the lift coefficient has also been studied. A higher ΔC_l was found for the iron serrations due to a larger surface area. However, the measurements with serrations contained significant uncertainties in the flap angle. This was specially important for the DTU case, which showed deviations of 4 deg with respect to the nominal value. The velocity profile in the vicinity of the trailing edge has been also measured. The boundary layer displacement thickness (δ^*) has been calculated and compared to XFOIL predictions, which agreed well in terms of Re_c and tripping trends.

The acoustic results have been firstly discussed for the straight trailing edge configuration. The effect of the tripping on the far-field noise has been assessed. Within the same Re_c measured, it was observed that the forced boundary layer lead to a level increase up to 5 dB in the low frequency part of the spectrum. This was related to the increase of δ^*. Broadband peaks in the high frequency part were found and attributed to trailing-edge bluntness noise. Increasing the angle of attack lead to a rise in the levels in the low frequency part of the spectrum, and a decrease in the high frequency part. This was also associated to the varying thickness of the boundary layer. For the clean configuration, laminar boundary-layer instability tones appeared at non-zero α_{eff}. They were found to be Re_c dependant, and good agreement on the tone presence and location between facilities was observed. An overlapping measurement point was available at

$Re_c \approx 0.38 \times 10^6$ between the A-Tunnel and the AWB. Good agreement at frequencies around 1-2 kHz was found, but differences in the spectral slope lead to a mismatch up to 6 dB at 3-4 kHz. Although the physical model tested was the same, the post-processing of the data was different, and it could have introduced some deviations. A study of the possible scatter introduced in this step is required. The scaling of the acoustic data showed a good agreement on the peak locations and levels, specially between AWB and DTU results. Generally, the curves shifted towards lower St_{δ^*} as Re_c increases. This was particularly pronounced in the TUD measurements, which covered a more extended peak Strouhal range than the AWB equivalent and the BPM predictions. The Re_c effect was particularly visible at $\alpha \approx 7-8$. At this angle the lift coefficients were already different due to early separation at low Re_c, and thus the acoustic results were also distinct for the two airfoil models.

The noise reduction effect has been measured and studied for the different serration types. Tones present in the clean measurements were significantly attenuated with the add-ons installed, leading to reductions in the $OSPL$ up to 10 dB. The noise reduction spectrum $\Delta SPL_{1/3}$ scaled fairly well with St_{δ^*}, and good agreement was found between different facilities and Re_c. Two noise reduction peaks were generally observed. The iron serrations were found to provide up to 7.5-8 dB of maximum noise reduction, whereas for the sawtooth serration it was around 5 dB. The overall sound reduction decreased with the flap angle and the angle of attack. This is likely a consequence of the increased aerodynamic loading and the appearance of counter-rotating vortices in the serration edges. The iron serrations were more sensible to α_{eff} changes due to a larger surface that lead to higher loading, as it was observed when comparing the ΔC_l.

Funding Sources

The current work is part of Task 39 "Quiet Wind Turbine Technology", an initiative within the Technology Cooperation Programme (TCP) by the International Energy Agency (IEA). The authors would like to thank the German Federal Ministry for Economic Affairs and Climate Action (BMWK) for supporting the operation of this task.

The authors would like to thank the Danish Energy Agency for funding the participation of the Technical University of Denmark in the IEA Task 39 under the programme "Energiteknologiske Udviklings- og Demonstrationsprogram (EUDP)", Journal number 134-21022.

Acknowledgments

Special thanks are due to Jorge Pereira Gomes for his valuable support during the NWB measurement campaigns. We would like to thank the wind tunnel engineers Jimmy S. Beckerlee and Sigurd B. Ildvedsen for conducting the experiments in the Poul La Cour wind Tunnel at the Technical University of Denmark.

References

[1] Howe, M. S., "A review of the theory of trailing edge noise," *Journal of Sound and Vibration*, Vol. 61, No. 3, 1978, pp. 437–465. https://doi.org/10.1016/0022-460X(78)90391-7.

[2] Lee, S., Ayton, L., Bertagnolio, F., Moreau, S., Chong, T. P., and Joseph, P., "Turbulent boundary layer trailing-edge noise: Theory, computation, experiment, and application," *Progress in Aerospace Sciences*, Vol. 126, 2021, p. 100737. https://doi.org/10.1016/J.PAEROSCI.2021.100737.

[3] Oerlemans, S., Sijtsma, P., and Méndez López, B., "Location and quantification of noise sources on a wind turbine," *Journal of Sound and Vibration*, Vol. 299, No. 4-5, 2007, pp. 869–883. https://doi.org/10.1016/j.jsv.2006.07.032.

[4] Herr, M., Bahr, C., and Kamzurraman, M., "Workshop Category 1: Trailing-Edge Noise. Problem Statement for the AIAA/CEAS Second Workshop on Benchmark Problems for Airframe Noise Computations (BANC-II)," 2012.

[5] Herr, M., and Kamruzzaman, M., "Benchmarking of trailing-edge noise computations - Outcome of the BANC-II workshop," *19th AIAA/CEAS Aeroacoustics Conference*, American Institute of Aeronautics and Astronautics, 2013. https://doi.org/10.2514/6.2013-2123.

[6] Herr, M., Ewert, R., Rautmann, C., Kamruzzaman, M., Bekiropoulos, D., Iob, A., Arina, R., Batten, P., Chakravarthy, S., and Bertagnolio, F., "Broadband trailing-edge noise predictions— overview of BANC-III results," *21st AIAA/CEAS Aeroacoustics Conference*, American Institute of Aeronautics and Astronautics, 2015. https://doi.org/10.2514/6.2015-2847.

[7] Oerlemans, S., and Schepers, J., "Prediction of wind turbine noise and validation against experiment," *International Journal of Aeroacoustics*, Vol. 8, No. 6, 2009, pp. 555–584. https://doi.org/10.1260/147547209789141489.

[8] Fischer, A., Bertagnolio, F., Shen, W. Z., and Madsen, J., "Noise model for serrated trailing edges compared to wind tunnel measurements," *Journal of Physics: Conference Series*, Vol. 753, IOP Publishing, 2016. https://doi.org/10.1088/1742-6596/753/2/022053.

[9] Ferret Gasch, O., Oerlemans, S., Faßmann, B. W., Herr, M., Bertagnolio, F., Fischer, A., Arnold, B., and Lutz, T., "Trailing edge noise prediction of wind turbine airfoils: A benchmark exercise," *25th AIAA/CEAS Aeroacoustics Conference*, American Institute of Aeronautics and Astronautics, 2019. https://doi.org/10.2514/6.2019-2675.

[10] Timmer, W. A., and Rooij, R. P. J. O. M. V., "Summary of the Delft University Wind Turbine Dedicated Airfoils," *41st AIAA Aerospace Sciences Meeting and Exhibit*, American Institute of Aeronautics and Astronautics, 2003. https://doi.org/10.2514/6.2003-352.

[11] Luesutthiviboon, S., Lima Pereira, L. T., Ragni, D., Avallone, F., and Snellen, M., "Aeroacoustic Benchmarking of Trailing-edge Noise from a NACA 63_3–018 Airfoil with Trailing-Edge Serrations," *Under review, AIAA Journal*, 2022.

[12] Fischer, A., Bak, C., Lylloff, O., Olsen, A. S., Mikkelsen, F., Ildvedsen, S. B., Beckerlee, J. S., Kuester, M., and Intaratep, N., "Cross validation of the aerodynamic and acoustic measurements in two Kevlar-walled wind tunnels," *Acccepted for publication in: Journal of Physics: Conference Series*, IOP Publishing, 2022.

[13] Avallone, F., van der Velden, W. C., and Ragni, D., "Benefits of curved serrations on broadband trailing-edge noise reduction," *Journal of Sound and Vibration*, Vol. 400, 2017, pp. 167–177. https://doi.org/10.1016/j.jsv.2017.04.007.

[14] Allen, H. J., and Vinceti, W. G., "Wall interference in a two-dimensional-flow wind tunnel with consideration of the effect of compressibility," Tech. rep., NACA, Ames Aeronautical Laboratory, Moffett Field, California, US, 1944.

[15] Devenport, W. J., Burdisso, R. A., Borgoltz, A., Ravetta, P. A., Barone, M. F., Brown, K. A., and Morton, M. A., "The Kevlar-walled anechoic wind tunnel," *Journal of Sound and Vibration*, Vol. 332, No. 17, 2013, pp. 3971–3991. https://doi.org/10.1016/j.jsv.2013.02.043.

[16] Sijtsma, P., "CLEAN based on spatial source coherence," *International Journal of Aeroacoustics*, Vol. 6, No. 4, 2007, pp. 357–374. https://doi.org/10.1260/147547207783359459.

[17] Lylloff, O., *Aeroacoustic wind tunnel tests*, DTU Wind Energy, PhD Thesis, 2020. https://doi.org/10.11581/dtu:00000102.

[18] Merino-Martínez, R., Rubio Carpio, A., Lima Pereira, L. T., van Herk, S., Avallone, F., Ragni, D., and Kotsonis, M., "Aeroacoustic design and characterization of the 3D-printed, open-jet, anechoic wind tunnel of Delft University of Technology," *Applied Acoustics*, Vol. 170, 2020. https://doi.org/10.1016/j.apacoust.2020.107504.

[19] Johnson, D. H., and Dudgeon, D. E., *Array Signal Processing: Concepts and Techniques*, Prentice Hall, 1993.

[20] Timmer, W., "Two-Dimensional Low-Reynolds Number Wind Tunnel Results for Airfoil NACA 0018," *Wind Engineering*, Vol. 32, No. 6, 2008, pp. 525–537. https://doi.org/10.1260/030952408787548848.

[21] Garner, H. C., Rogers, E. W. E., Acum, W. E. A., and Maskell, E. C., "Subsonic Wind Tunnel Wall Corrections," Tech. rep., AGARD, Paris, 1966.

[22] Pott-Pollenske, M., and Delfs, J., "Enhanced capabilities of the Aeroacoustic Wind Tunnel Braunschweig," *14th AIAA/CEAS Aeroacoustics Conference (29th AIAA Aeroacoustics Conference)*, American Institute of Aeronautics and Astronautics, 2008. https://doi.org/10.2514/6.2008-2910.

[23] Sen, R., "Interpretation of Acoustic Source Maps Made with an Elliptic-Mirror Directional Microphone System," *Aeroacoustics Conference*, 1996.

[24] Schlinker, R., "Airfoil Trailing Edge Noise Measurements with a Directional Microphone," *4th Aeroacoustics Conference*, American Institute of Aeronautics and Astronautics, Atlanta, GA, U.S.A., 1977. https://doi.org/10.2514/6.1977-1269.

[25] Herr, M., "Trailing-Edge Noise—Reduction Concepts and Saling Laws," *Dissertation, DLR Report ISRN DLR-FB-2013-32, ISSN 1434-8454*, 2013.

[26] Bergmann, A., "The Aeroacoustic Wind Tunnel DNW-NWB," *18th AIAA/CEAS Aeroacoustics Conference*, American Institute of Aeronautics and Astronautics, Colorado Springs, Colorado, USA, 2012. https://doi.org/10.2514/6.2012-2173.

[27] Drela, M., "XFOIL: An Analysis and Design System for Low Reynolds Number Airfoils," *Low Reynolds Number Aerodynamics*, edited by T. J. Mueller, Lecture Notes in Engineering, Springer, Berlin, Heidelberg, 1989, pp. 1–12. https://doi.org/10.1007/978-3-642-84010-4.

[28] Brooks, T. F., Marcolini, M. A., and Pope, D. S., "Airfoil trailing edge flow measurements and comparison with theory, incorporating open wind tunnel corrections," *AIAA/NASA 9th Aeroacoustics Conference*, American Institute of Aeronautics and Astronautics, 1984.

[29] Brown, K. A., *Understanding and exploiting wind tunnels with porous flexible walls for aerodynamic measurement*, Virginia Tech, PhD thesis, 2016.

[30] Kiefer, J., Miller, M. A., Hultmark, M., and Hansen, M. O., "Effects of finite aspect ratio on wind turbine airfoil measurements," *Journal of Physics: Conference Series*, Vol. 753, No. 2, 2016. https://doi.org/10.1088/1742-6596/753/2/022040.

[31] Russo, G. P., *Aerodynamic measurements. From phyisical principles to turnkey instrumentation*, Woodhead Publishing, Cambridge, UK, 2011. https://doi.org/10.1533/9780857093688.

[32] Clauser, F. H., "The Turbulent Boundary Layer," *Advances in Applied Mechanics*, Vol. 4, No. C, 1956, pp. 1–51. https://doi.org/10.1016/S0065-2156(08)70370-3.

[33] Brooks, T. F., Pope, D. S., and Marcolini, M. A., "Airfoil Self-Noise and Prediction," Tech. rep., NASA, Hampton, VA, 1989.

[34] Herr, M., Appel, C., Dierke, J., and Ewert, R., "Trailing-Edge Noise Data Quality Assessment for CAA Validation," *16th AIAA/CEAS Aeroacoustics Conference*, American Institute of Aeronautics and Astronautics, 2010. https://doi.org/10.2514/6.2010-3877.

[35] Gruber, M., Joseph, P. F., and Chong, T. P., "On the mechanisms of serrated airfoil trailing edge noise reduction," *17th AIAA/CEAS Aeroacoustics Conference (32nd AIAA Aeroacoustics Conference)*, American Institute of Aeronautics and Astronautics, 2011. https://doi.org/10.2514/6.2011-2781.

[36] Moreau, D. J., and Doolan, C. J., "Noise-reduction mechanism of a flat-plate serrated trailing edge," *AIAA Journal*, Vol. 51, No. 10, 2013, pp. 2513–2522. https://doi.org/10.2514/1.J052436.

[37] Zhou, P., Liu, Q., Zhong, S., Fang, Y., and Zhang, X., "A study of the effect of serration shape and flexibility on trailing edge noise," *Physics of Fluids*, Vol. 32, No. 12, 2020. https://doi.org/10.1063/5.0032774.

[38] Avallone, F., Pröbsting, S., and Ragni, D., "Three-dimensional flow field over a trailing-edge serration and implications on broadband noise," *Physics of Fluids*, Vol. 28, No. 11, 2016. https://doi.org/10.1063/1.4966633.

[39] Arce León, C., Merino-Martínez, R., Ragni, D., Avallone, F., Scarano, F., Pröbsting, S., Snellen, M., Simons, D. G., and Madsen, J., "Effect of trailing edge serration-flow misalignment on airfoil noise emissions," *Journal of Sound and Vibration*, Vol. 405, 2017, pp. 19–33. https://doi.org/10.1016/j.jsv.2017.05.035.

[40] Chong, T. P., and Joseph, P. F., "An experimental study of airfoil instability tonal noise with trailing edge serrations," *Journal of Sound and Vibration*, Vol. 332, No. 24, 2013, pp. 6335–6358. https://doi.org/10.1016/j.jsv.2013.06.033.

C

DTU data signal-to-noise ratio

The signal-to-noise ratio of the DTU measurements is now estimated. We have to ensure that the data that we are studying comes primarily from the trailing-edge, and remove frequencies that are heavily affected by other sources. The same procedure as in [81] is used. Besides the integration region centered at the trailing edge, two integration regions are additionally defined in the airfoil corners. The corners have proven to be a dominant source at high frequencies, and we want to quantify their dominance. The integration regions are shown in Figure C.1.

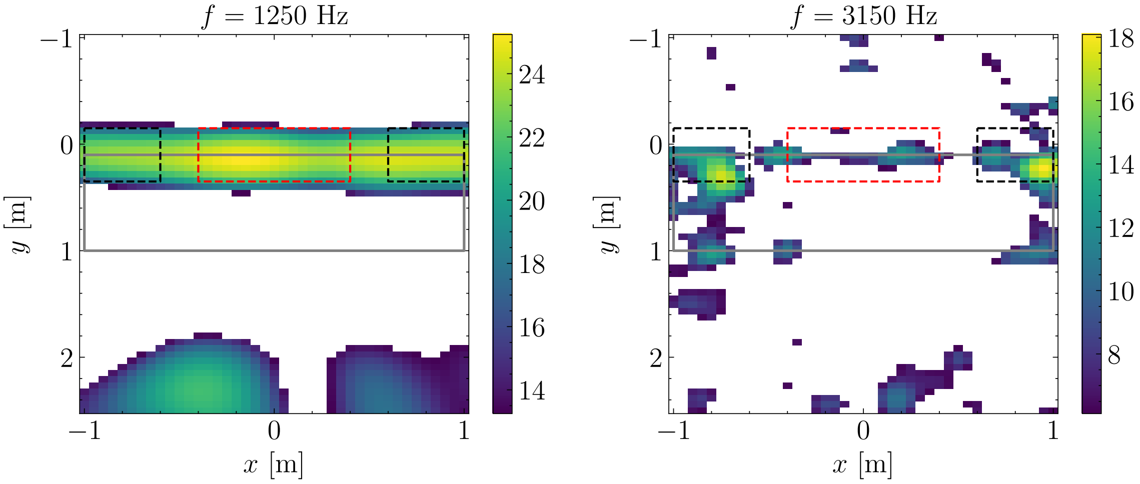

Figure C.1: DTU beamforming images with additional integration regions to determine SNR. Flow goes to positive y. Red dashed region aims to capture the trailing-edge noise contributions, and black ones the corners. Measurement at 50 m/s, dynamic range is 12 dB.

The dimension of the trailing-edge integration region is the same that the sum of the two corner regions. A criterion is set such that when the integrated level from the corners supersedes the trailing-edge one, that frequency band will not be considered for further analysis. The comparison of the integrated SPL from both regions is shown in Figure C.2. We can see that for 34 and 67 m/s, the results from the trailing-edge region are constantly 2-4 dB greater than the level from the corners. From $f = 2500$ Hz, the corners start to dominate. Nevertheless, at 50 m/s, the levels at $400 \leq f \leq 1600$ Hz are very similar in both regions. After that, the corners dominate. It is unclear why the 50 m/s case shows different results at low frequencies compared to the other velocities. The visual analysis of the beamforming images still shows very similar results between facilities. Therefore, the data at low frequencies for the 50 m/s case will also be kept. It is decided to disregard the data from and including 2500 Hz.

Note the drop in level and SNR at 2000 Hz for the 50 m/s case. It corresponds to the vortex shedding frequency of the pitot tube, and it appears as the dominant source (see Figure 5.17). Trailing-edge noise is not well quantified at this frequency, and we should also disregard this frequency. However, it will be kept for the

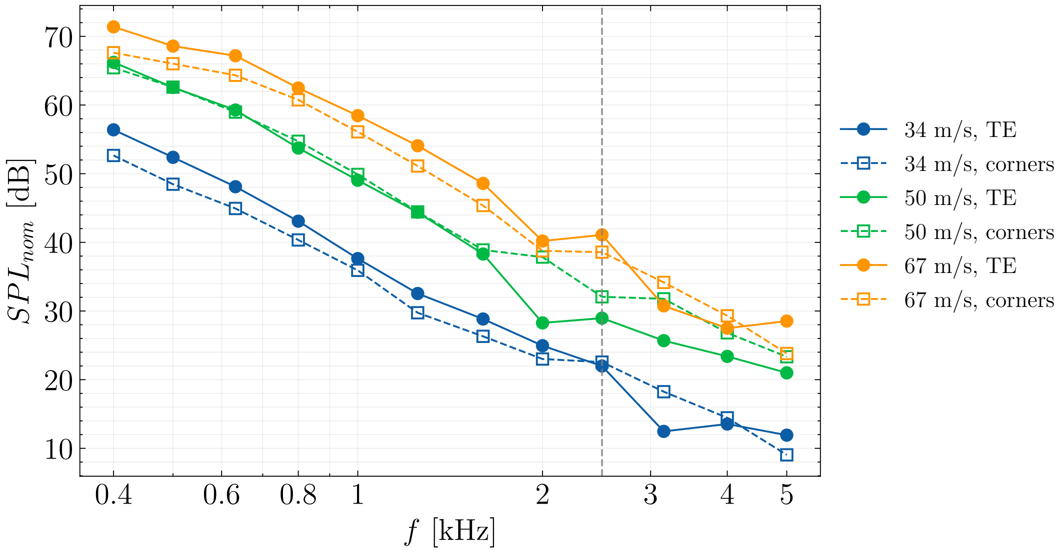

Figure C.2: Comparison of the integrated spectra around the corners and centered at the trailing edge.

uncertainty quantification Section in order to study how the uncertainty behaves where the source of interest is not well resolved.

D

Coherence: support figures

The microphone coherence of the A-Tunnel and the AWB is presented in the following figures to support the discussion of Section 5.2.3.

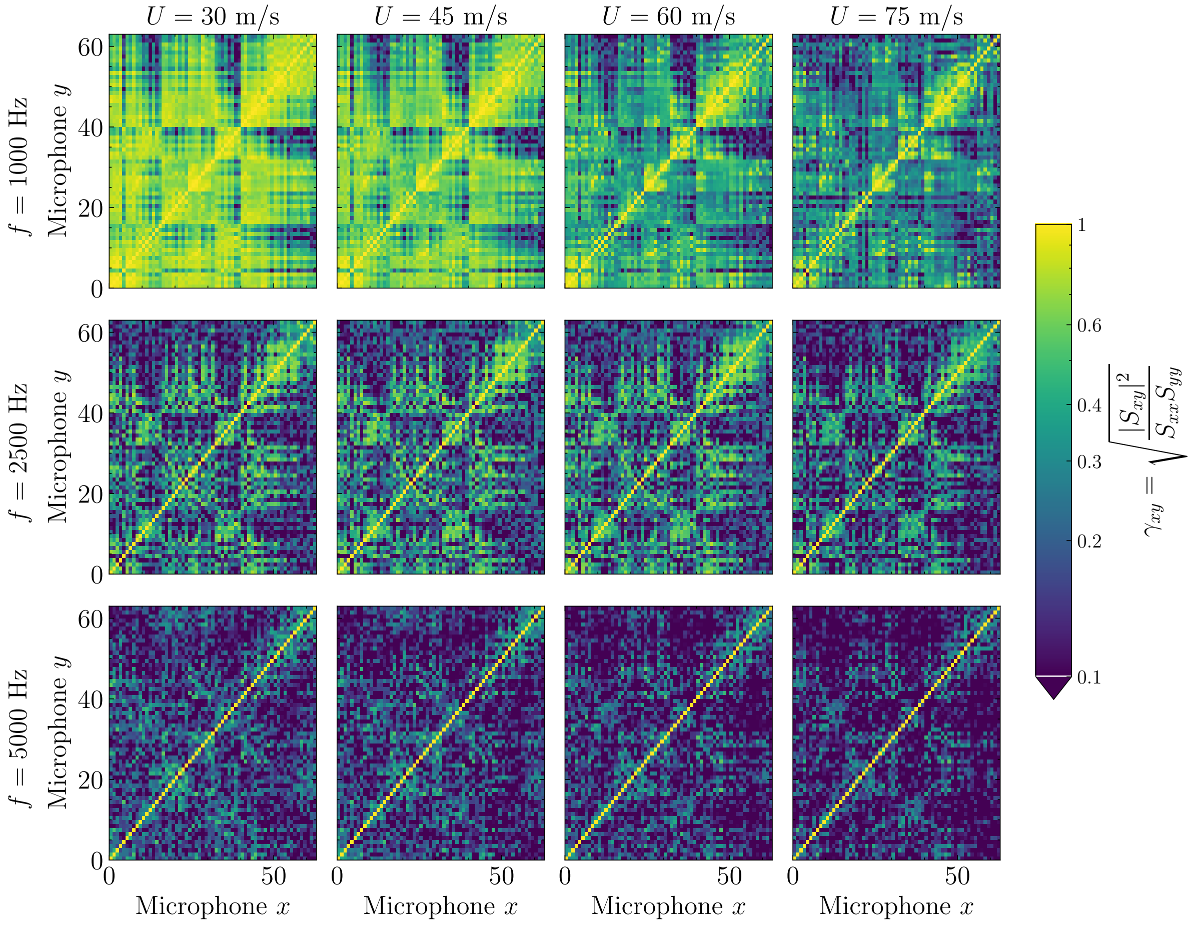

Figure D.1: A-Tunnel microphone coherence.

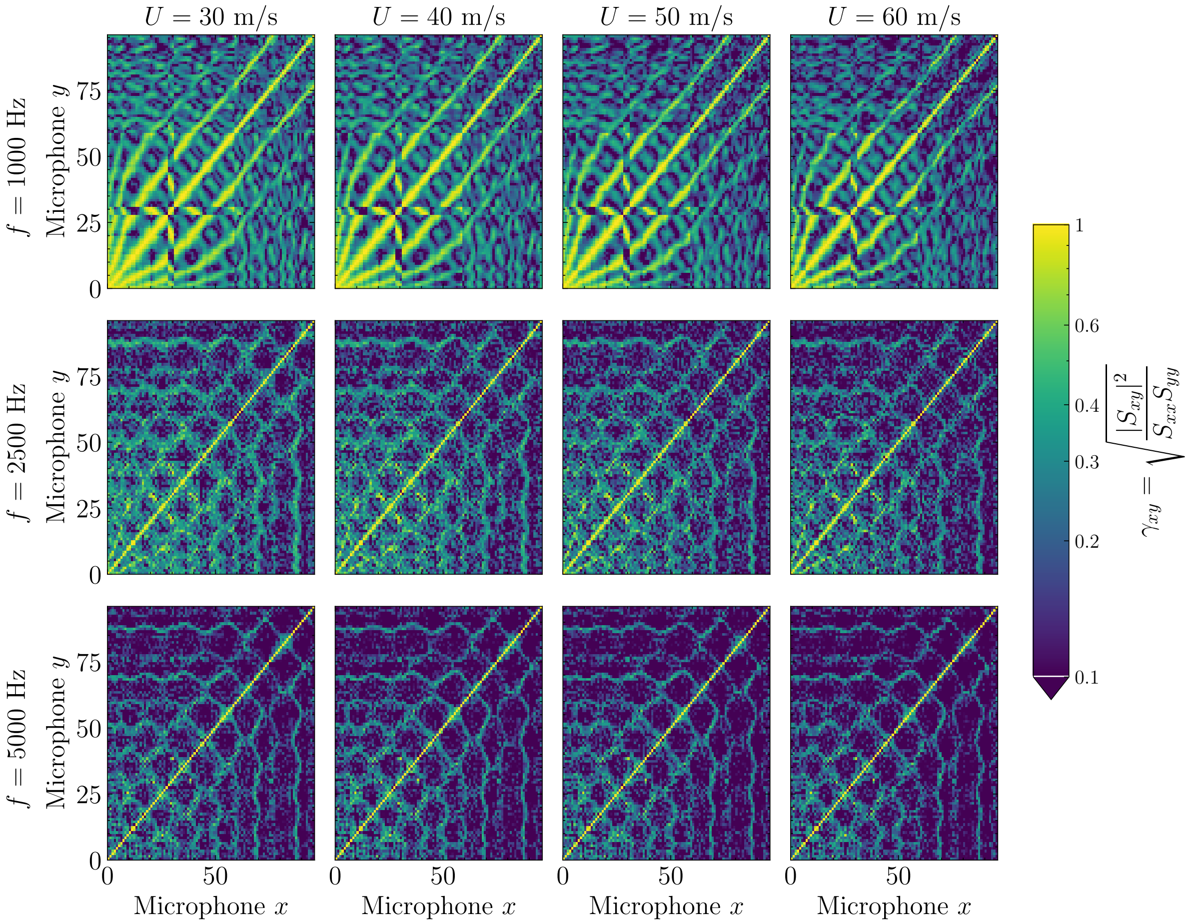

Figure D.2: AWB microphone coherence.

E

UQ: support figures

Delay-and-sum

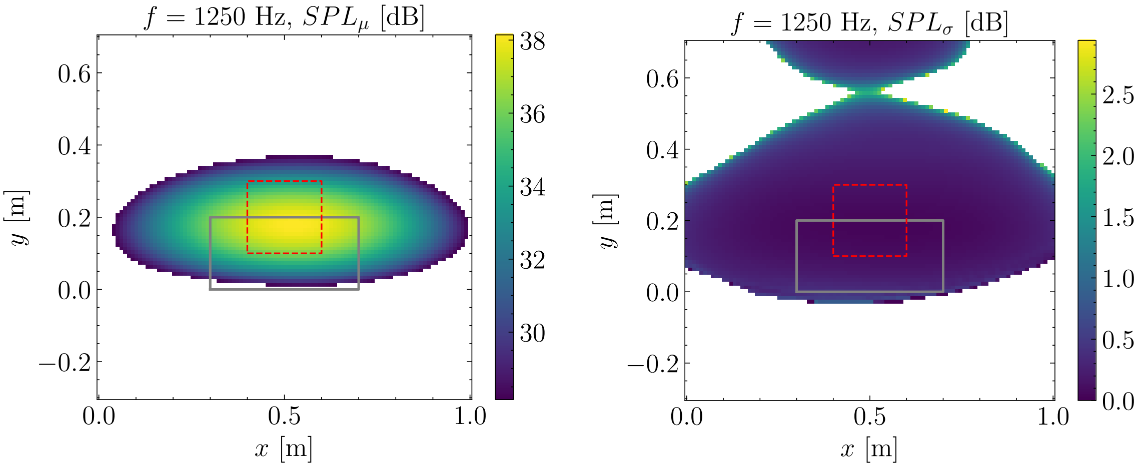

Figure E.1: Beamforming images from Monte-Carlo. A-Tunnel at 45 m/s and 1250 Hz. Flow goes to positive y. σ_{loc} = 10 mm (uncorrelated). Dynamic range is 10 dB.

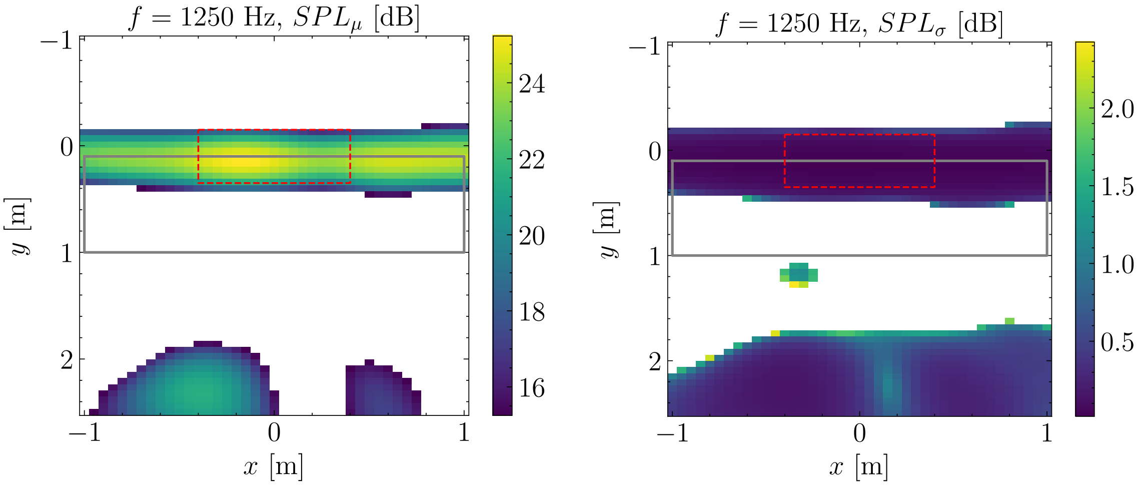

Figure E.2: Beamforming images from Monte-Carlo. DTU at 50 m/s and 1250 Hz. Flow goes to negative y. σ_{loc} = 10 mm (uncorrelated). Dynamic range is 10 dB.

Clean-SC

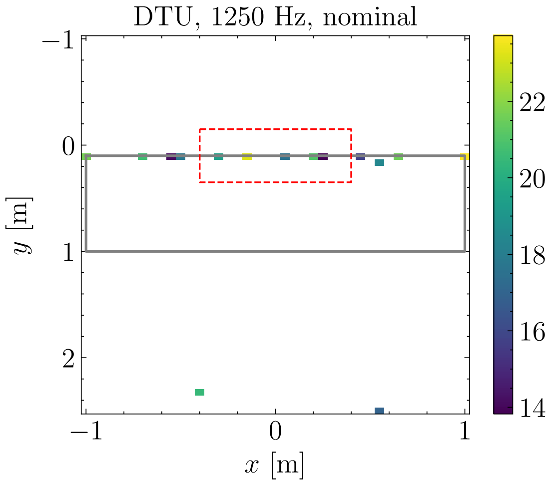

Figure E.3: Nominal beamforming image for DTU at 50 m/s and 1250 Hz. Clean-SC deconvolution. Flow goes to negative y. σ_{loc} = 10 mm. Dynamic range is 10 dB.

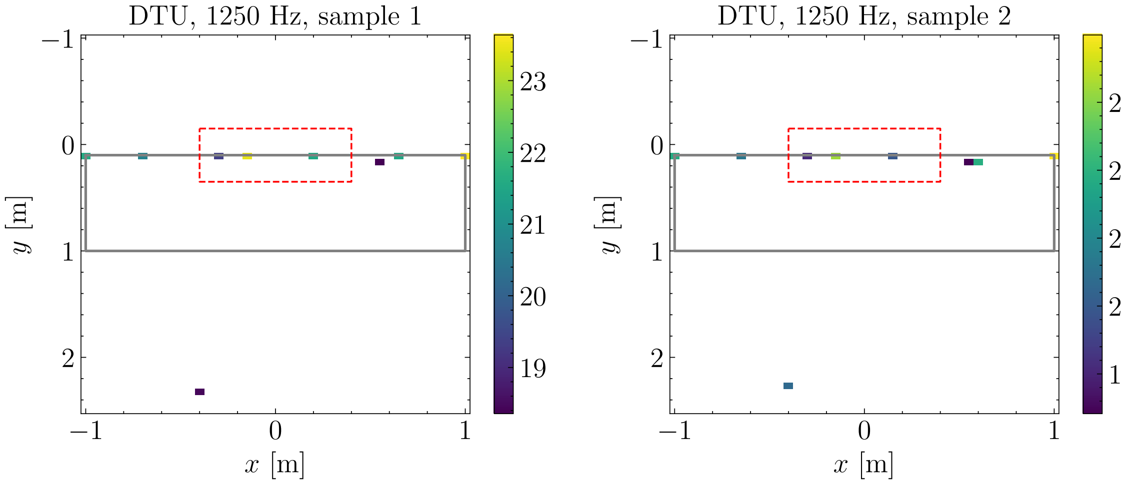

Figure E.4: Beamforming images from Monte-Carlo (samples 1 and 2). DTU at 50 m/s and 1250 Hz. Clean-SC deconvolution. Flow goes to negative y. σ_{loc} = 10 mm. Dynamic range is 10 dB.

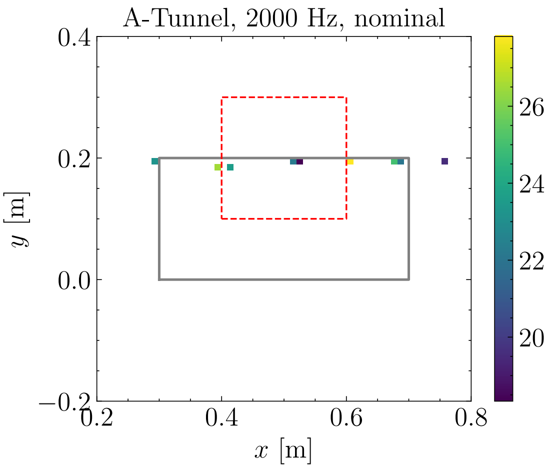

Figure E.5: Nominal beamforming image for the A-Tunnel at 45 m/s and 2000 Hz. Clean-SC deconvolution. Flow goes to positive y. σ_{loc} = 10 mm. Dynamic range is 10 dB. Image zoomed to the airfoil, not representative of the whole scan plane ($x = [0,1]$, $y = [-0.3, 0.7]$)

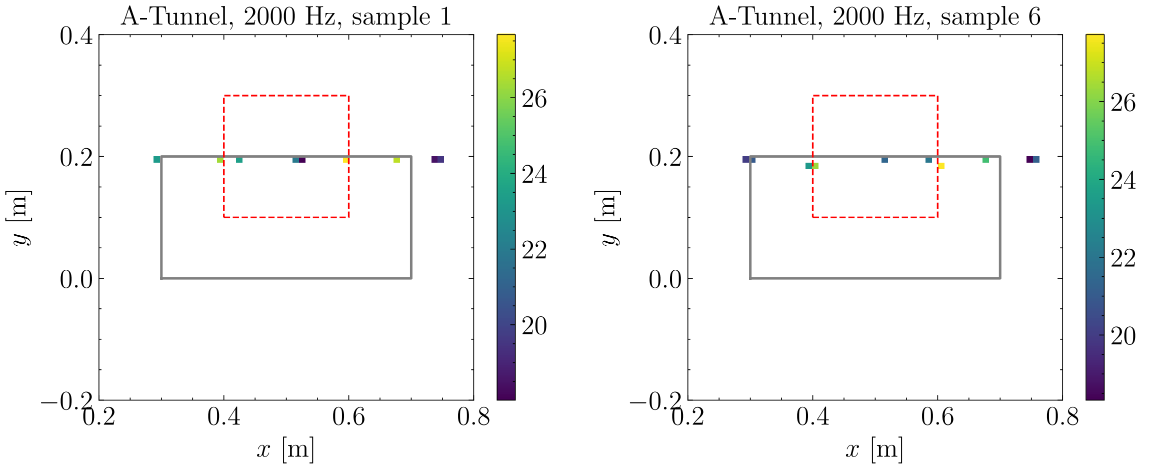

Figure E.6: Beamforming images from Monte-Carlo. A-Tunnel at 45 m/s and 2000 Hz. Clean-SC deconvolution. Flow goes to positive y. σ_{loc} = 10 mm. Dynamic range is 10 dB. Image zoomed to the airfoil, not representative of the whole scan plane ($x = [0,1]$, $y = [-0.3, 0.7]$).

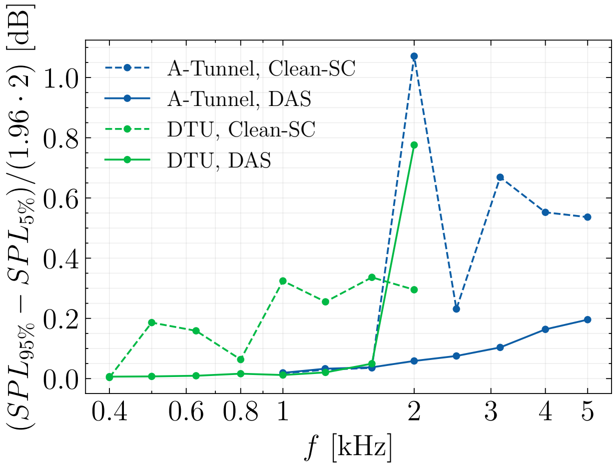

Figure E.7: Spectra standard deviation for DAS and Clean-SC using 95% percentiles.

Bibliography

[1] M. S. Howe, "A review of the theory of trailing edge noise," *Journal of Sound and Vibration*, vol. 61, no. 3, pp. 437–465, 1978, ISSN: 10958568. DOI: `10.1016/0022-460X(78)90391-7`.

[2] S. Lee, L. Ayton, F. Bertagnolio, S. Moreau, T. P. Chong, and P. Joseph, "Turbulent boundary layer trailing-edge noise: Theory, computation, experiment, and application," *Progress in Aerospace Sciences*, vol. 126, p. 100 737, 2021, ISSN: 0376-0421. DOI: `10.1016/J.PAEROSCI.2021.100737`.

[3] N. Intaratep, W. Nathan Alexander, W. J. Deveport, S. M. Grace, and A. Dropkin, "Experimental study of quadcopter acoustics and performance at static thrust conditions," *22nd AIAA/CEAS Aeroacoustics Conference, 2016*, pp. 1–14, 2016. DOI: `10.2514/6.2016-2873`.

[4] R. R. Begault, "Overview of Metrics pertinent to Human Response to UAM Noise," in *Acoustics and Urban Air Mobility Technical Working Group Meeting, Cleveland*, OH, 2019. [Online]. Available: `https://ntrs.nasa.gov/search.jsp?R=20180007464`.

[5] S. Li and S. Lee, "A machine learning-based fast prediction of rotorcraft broadband noise," in *AIAA Aviation 2020 Forum*, 2020, ISBN: 9781624105982. DOI: `10.2514/6.2020-2588`.

[6] R. Snider, T. Samuels, B. Goldman, and K. S. Brentner, "Full-scale rotorcraft broadband noise prediction and its relevance to civil noise certification criteria," in *69th American Helicopter Society International Annual Forum 2013*, vol. 2, 2013, pp. 1293–1307, ISBN: 9781627486514.

[7] S Wagner, R. Bareiss, and G. Guidati, *Wind Turbine Noise*. Berlin: Springer, 1996, ISBN: 9783642887123. DOI: `10.1260/0957456042872777`.

[8] S. Oerlemans, P. Sijtsma, and B. Méndez López, "Location and quantification of noise sources on a wind turbine," *Journal of Sound and Vibration*, vol. 299, no. 4-5, pp. 869–883, 2007, ISSN: 10958568. DOI: `10.1016/j.jsv.2006.07.032`.

[9] C. Doolan, "A review of wind turbine noise perception, annoyance and low frequency emission," *Wind Engineering*, vol. 37, no. 1, pp. 97–104, 2013, ISSN: 0309524X. DOI: `10.1260/0309-524X.37.1.97`.

[10] F. van den Berg, E. Pedersen, J. Bouma, and R. Bakker, "Visual and acoustic impact of wind turbine farms on residents," Unveristiy of Groningen, Tech. Rep. 044628, 2005.

[11] E. Koppen and K. Fowler, "International legislation for wind turbine noise," *Euronoise*, pp. 321–326, 2015.

[12] J. G. Schepers *et al.*, "Sirocco: Silent rotors by acoustic optimisation," *European Wind Energy Conference and Exhibition 2006, EWEC 2006*, vol. 1, pp. 596–606, 2006.

[13] *IEA Wind TCP Task 39*. [Online]. Available: `https://iea-wind.org/task39/` (visited on 07/17/2022).

[14] M. S. Howe, "Aerodynamic noise of a serrated trailing edge," *Journal of Fluids and Structures*, vol. 5, no. 1, pp. 33–45, 1991, ISSN: 10958622. DOI: `10.1016/0889-9746(91)80010-B`.

[15] S. Oerlemans, "Reduction of wind turbine noise using blade trailing edge devices," in *22nd AIAA/CEAS Aeroacoustics Conference*, 2016, ISBN: 9781624103865. DOI: `10.2514/6.2016-3018`.

[16] S. Oerlemans and J. Schepers, "Prediction of wind turbine noise and validation against experiment," *International Journal of Aeroacoustics*, vol. 8, no. 6, pp. 555–584, 2009. DOI: `10.1260/147547209789141489`.

[17] F. Avallone, S. Pröbsting, and D. Ragni, "Three-dimensional flow field over a trailing-edge serration and implications on broadband noise," *Physics of Fluids*, vol. 28, no. 11, 2016, ISSN: 10897666. DOI: `10.1063/1.4966633`.

[18] C. Arce León *et al.*, "Effect of trailing edge serration-flow misalignment on airfoil noise emissions," *Journal of Sound and Vibration*, vol. 405, pp. 19–33, 2017, ISSN: 10958568. DOI: `10.1016/j.jsv.2017.05.035`.

[19] D. J. Moreau and C. J. Doolan, "Noise-reduction mechanism of a flat-plate serrated trailing edge," *AIAA Journal*, vol. 51, no. 10, pp. 2513–2522, 2013, ISSN: 00011452. DOI: `10.2514/1.J052436`.

[20] T. P. Chong and P. F. Joseph, "An experimental study of airfoil instability tonal noise with trailing edge serrations," *Journal of Sound and Vibration*, vol. 332, no. 24, pp. 6335–6358, 2013, ISSN: 0022460X. DOI: 10.1016/j.jsv.2013.06.033.

[21] F. Avallone, W. C. van der Velden, and D. Ragni, "Benefits of curved serrations on broadband trailing-edge noise reduction," *Journal of Sound and Vibration*, vol. 400, pp. 167–177, 2017, ISSN: 10958568. DOI: 10.1016/j.jsv.2017.04.007.

[22] M. Gruber, P. F. Joseph, and T. P. Chong, "On the mechanisms of serrated airfoil trailing edge noise reduction," in *17th AIAA/CEAS Aeroacoustics Conference (32nd AIAA Aeroacoustics Conference)*, American Institute of Aeronautics and Astronautics, 2011, ISBN: 9781600869433. DOI: 10.2514/6.2011-2781.

[23] P. Kholodov and S. Moreau, "Optimization of serrations for broadband trailing-edge noise reduction using an analytical model," no. May, pp. 1–14, 2019. DOI: 10.2514/6.2019-2655.

[24] A. Fischer, F. Bertagnolio, W. Z. Shen, and J. Madsen, "Noise model for serrated trailing edges compared to wind tunnel measurements," in *Journal of Physics: Conference Series*, vol. 753, IOP Publishing, 2016. DOI: 10.1088/1742-6596/753/2/022053.

[25] Y. D. Mayer, B. Lyu, H. K. Jawahar, and M. Azarpeyvand, "A semi-analytical noise prediction model for airfoils with serrated trailing edges," *Renewable Energy*, vol. 143, pp. 679–691, 2019, ISSN: 18790682. DOI: 10.1016/j.renene.2019.04.132. [Online]. Available: https://doi.org/10.1016/j.renene.2019.04.132.

[26] T. F. Brooks and T. Hodgson, "Trailing edge noise prediction from measured surface pressures," *Journal of Sound and Vibration*, vol. 78, no. 1, pp. 69–117, 1981. DOI: https://doi.org/10.1016/S0022-460X(81)80158-7.

[27] M. Kamruzzaman *et al.*, "Validations and improvements of airfoil trailing-edge noise prediction models using detailed experimental data," *Wind Energy*, vol. 14, no. November 2011, pp. 45–61, 2013. DOI: 10.1002/we.

[28] A. Fischer, F. Bertagnolio, and H. A. Madsen, "Improvement of TNO type trailing edge noise models," *European Journal of Mechanics - B/Fluids*, vol. 61, pp. 255–262, 2017, ISSN: 09977546. DOI: 10.1016/j.euromechflu.2016.09.005.

[29] O. Ferret Gasch *et al.*, "Trailing edge noise prediction of wind turbine airfoils: A benchmark exercise," in *25th AIAA/CEAS Aeroacoustics Conference*, American Institute of Aeronautics and Astronautics, 2019, ISBN: 9781624105883. DOI: 10.2514/6.2019-2675.

[30] C. Bahr, J. Li, and L. Cattafesta, "Aeroacoustic Measurements in Open-jet Wind Tunnels – An Evaluation of Methods Applied to Trailing Edge Noise," in *17th AIAA/CEAS Aeroacoustics Conference*, Portland,Oregon: American Institute of Aeronautics and Astronautics, Inc., 2011.

[31] M. Herr, C. Appel, J. Dierke, and R. Ewert, "Trailing-Edge Noise Data Quality Assessment for CAA Validation," in *16th AIAA/CEAS Aeroacoustics Conference*, American Institute of Aeronautics and Astronautics, 2010. DOI: 10.2514/6.2010-3877.

[32] C. J. Doolan and D. J. Moreau, "A Review of Airfoil Trailing Edge Noise with Some Implications for Wind Turbines," *International Journal of Aeroacoustics*, vol. 14, no. 5-6, pp. 811–832, 2015, ISSN: 1475-472X. DOI: 10.1260/1475-472x.14.5-6.811.

[33] M. Herr, C. Bahr, and M. Kamzurraman, "Workshop Category 1: Trailing-Edge Noise. Problem Statement for the AIAA/CEAS Second Workshop on Benchmark Problems for Airframe Noise Computations (BANC-II)," 2012.

[34] M. Herr and M. Kamruzzaman, "Benchmarking of trailing-edge noise computations - Outcome of the BANC-II workshop," in *19th AIAA/CEAS Aeroacoustics Conference*, American Institute of Aeronautics and Astronautics, 2013, ISBN: 9781624102134. DOI: 10.2514/6.2013-2123.

[35] M. Herr *et al.*, "Broadband trailing-edge noise predictions— overview of BANC-III results," in *21st AIAA/CEAS Aeroacoustics Conference*, American Institute of Aeronautics and Astronautics, 2015, ISBN: 9781624103674. DOI: 10.2514/6.2015-2847.

[36] S. Gleeg and W. Devenport, *Aeroacoustics of Low Mach Number Flows*, 1st. Academic Press, Elsevier, 2017, p. 529, ISBN: 9780128096512.

[37] H. J. Allen and W. G. Vinceti, “Wall interference in a two-dimensional-flow wind tunnel with consideration of the effect of compressibility,” NACA, Ames Aeronautical Laboratory, Moffett Field, California, US, Tech. Rep., 1944.

[38] D. Stephens, “The Acoustic Environment of the NASA Glenn 9- by 15-Foot Low-Speed Wind Tunnel,” in *21st AIAA/CEAS Aeroacoustics Conference*. 2015. DOI: `10.2514/6.2015-2684`. [Online]. Available: `https://arc.aiaa.org/doi/abs/10.2514/6.2015-2684`.

[39] T. F. Brooks, M. A. Marcolini, and D. S. Pope, “Airfoil trailing edge flow measurements and comparison with theory, incorporating open wind tunnel corrections,” in *AIAA/NASA 9th Aeroacoustics Conference*, American Institute of Aeronautics and Astronautics, 1984.

[40] R. K. Amiet, “Refraction of sound by a shear layer,” *Journal of Sound and Vibration*, vol. 58, no. 4, pp. 467–482, 1978, ISSN: 10958568. DOI: `10.1016/0022-460X(78)90353-X`.

[41] R. P. Dougherty, “Turbulent decorrelation of aeroacoustic phased arrays: lessons from atmospheric science and astronomy,” in *9th AIAA/CEAS Aeroacoustic Conference*, Hilton Head, South Carolina, 2003.

[42] P. Sijtsma, S. Oerlemans, T. Tibbe, T. Berkefeld, and C. Spehr, “Spectral broadening by shear layers of open jet wind tunnels,” *20th AIAA/CEAS Aeroacoustics Conference*, no. June, pp. 1–34, 2014. DOI: `10.2514/6.2014-3178`.

[43] R. Merino-Martínez *et al.*, “Aeroacoustic design and characterization of the 3D-printed, open-jet, anechoic wind tunnel of Delft University of Technology,” *Applied Acoustics*, vol. 170, 2020, ISSN: 1872910X. DOI: `10.1016/j.apacoust.2020.107504`.

[44] M. Pott-Pollenske, W. V. Heesen, and A. Bergmann, “Acoustical Preexamination Work and Characterization of the Low Noise Wind Tunnel DNW-NWB,” in *18th AIAA/CEAS Aeroacoustics Conference (33rd AIAA Aeroacoustics Conference)*, 2012. DOI: `10.2514/6.2012-2175`. [Online]. Available: `https://arc.aiaa.org/doi/abs/10.2514/6.2012-2175`.

[45] W. J. Devenport *et al.*, “The Kevlar-walled anechoic wind tunnel,” *Journal of Sound and Vibration*, vol. 332, no. 17, pp. 3971–3991, 2013, ISSN: 10958568. DOI: `10.1016/j.jsv.2013.02.043`.

[46] O. Lylloff, *Aeroacoustic wind tunnel tests*. DTU Wind Energy, PhD Thesis, 2020. DOI: `10.11581/dtu:00000102`.

[47] T. J. Mueller *et al.*, *Aeroacoustic Measurements*. New: Springer Berlin Heidelberg, 2002, vol. 15, ISBN: 978-3-642-07514-8. DOI: `10.1007/978-3-662-05058-3`.

[48] F. R. Grosche, H. Stiewitt, and B. Binder, “Acoustic wind-tunnel measurements with a highly directional microphone,” *AIAA Journal*, vol. 15, no. 11, pp. 1590–1596, 1977, ISSN: 00011452. DOI: `10.2514/3.60826`.

[49] F. R. Grosche, J. H. Jones, and G. A. Wildhold, “Measurements of the distribution of sound source intensitites in turbulent jets,” in *AIAA Aeroacousics Conference*, Seattle, Washington, 1973.

[50] P. Sijtsma, “Phased Array Beamforming Applied to Wind Tunnel and Fly-Over Tests,” *SAE Technical Papers*, 2010, ISSN: 01487191. DOI: `10.4271/2010-36-0514`.

[51] R. Sen, “Interpretation of acoustic source maps made with an elliptic-mirror directional microphone system,” *2nd AIAA/CEAS Aeroacoustics Conference*, no. May, 1996. DOI: `10.2514/6.1996-1712`.

[52] M Herr, “Design Criteria for Low-Noise Trailing-Edges,” in *13th AIAA/CEAS Aeroacoustics Conference (28th AIAA Aeroacoustics Conference)*, American Institute of Aeronautics and Astronautics, 2007.

[53] A. Piersol, “Use of coherence and phase data between two receivers in evaluation of noise enviroments,” *Journal of Sound and Vibration*, vol. 56, no. 2, pp. 215–228, 1978.

[54] T. F. Brooks, D. S. Pope, and M. A. Marcolini, “Airfoil Self-Noise and Prediction,” NASA, Hampton, VA, Tech. Rep., 1989.

[55] J. Ffowcs Williams and L. Hall, “Aerodynamic sound generation by turbulent flow in the vicinity of a scattering half plane,” *Journal of Fluid Mechanics*, vol. 40, no. 04, pp. 657–670, 1970. DOI: `10.1017/S0022112070000368`.

[56] J. Billingsley and R. Kinns, “The acoustic telescope,” *Journal of Sound and Vibration*, vol. 48, no. 4, pp. 485–510, 1976, ISSN: 10958568. DOI: `10.1016/0022-460X(76)90552-6`.

[57] P. Chiariotti, M. Martarelli, and P. Castellini, “Acoustic beamforming for noise source localization – Reviews, methodology and applications,” *Mechanical Systems and Signal Processing*, vol. 120, pp. 422–448, 2019, ISSN: 10961216. DOI: `10.1016/j.ymssp.2018.09.019`. [Online]. Available: `https://doi.org/10.1016/j.ymssp.2018.09.019`.

[58] J. Högbom, “Aperture synthesis with a non-regular distribution of interferometer baselines,” *Astronomy and Astrophysics Supplement*, vol. 15, no. 500/01, pp. 417–426, 1974.

[59] R. Merino-Martínez *et al.*, “A review of acoustic imaging methods using phased microphone arrays,” in *Aircraft Noise Generation and Assessment” Special Issue by the CEAS Aeronautical Journal*, 1, vol. 10, Springer Vienna, 2019, pp. 197–230, ISBN: 0123456789. DOI: `10.1007/s13272-019-00383-4`. [Online]. Available: `http://dx.doi.org/10.1007/s13272-019-00383-4`.

[60] P. D. Welch, “The Use of Fast Fourier Transform for the Estimation of Power Spectra,” *IEEE Transactions on audio and electroacoustics*, no. 2, pp. 70–73, 1967.

[61] E. Sarradj, “Three-dimensional acoustic source mapping with different beamforming steering vector formulations,” *Advances in Acoustics and Vibration*, vol. 2012, 2012, ISSN: 16876261. DOI: `10.1155/2012/292695`.

[62] T. F. Brooks and W. M. Humphreys, “Effect of Directional Array Size on the Measurement of Airframe Noise Components,” in *5th AIAA Aeroacoustics Conference*, 1999.

[63] P. Sijtsma, “CLEAN based on spatial source coherence,” *International Journal of Aeroacoustics*, vol. 6, no. 4, pp. 357–374, 2007, ISSN: 1475-472X. DOI: `10.1260/147547207783359459`.

[64] C. Lock, “The interference of a wind tunnel on a symmetrical body,” *Aeronautical Research Committee Reports and Memoranda*, 1929.

[65] H. C. Garner, E. W. E. Rogers, W. E. A. Acum, and E. C. Maskell, “Subsonic Wind Tunnel Wall Corrections,” AGARD, Paris, Tech. Rep., 1966.

[66] W. A. Timmer, “Wind Tunnel Wall Corrections for Two-Dimensional Testing up to Large Angles of Attack,” in *Handbook of Wind Energy Aerodynamics*, 2021, ISBN: 9783030054557. DOI: `10.1007/978-3-030-05455-7-27-1`.

[67] W. Mangler, “The lift distribution of wings with end plates,” NACA Technical Memorandum 856, Washington, Tech. Rep., 1938.

[68] P. Fuglsang, I. Antoniou, N. N. Sørensen, and H. A. Madsen, *Validation of a Wind Tunnel Testing Facility for Blade Surface Pressure Measurements.* 1998, vol. 981, p. 82, ISBN: 8755023002.

[69] K. A. Brown, *Understanding and exploiting wind tunnels with porous flexible walls for aerodynamic measurement.* Virginia Tech, PhD thesis, 2016.

[70] A. Fischer *et al.*, “Cross validation of the aerodynamic and acoustic measurements in two Kevlar-walled wind tunnels,” in *Acccepted for publication in: Journal of Physics: Conference Series*, IOP Publishing, 2022.

[71] W. Devenport *et al.*, “Design and Operation of Hybrid Aeroacoustic Wind Tunnels,” *Design and Operation of Aeroacoustic Wind Tunnel Tests for Group and Air Transport*, vol. STO-EN-AVT, no. May, 2017. [Online]. Available: `papers3://publication/doi/10.14339/STO-EN-AVT-287`.

[72] A. Fischer, O. Lylloff, C. Bak, and E. Fernandez Grande, “Analytical shear layer corrections for acoustic transmission in Kevlar walled wind tunnels and their experimental validation,” in *28th AIAA/CEAS Aeroacoustics 2022 Conference*, Southampton, UK, 2022. DOI: `10.2514/6.2022-2979`.

[73] P. Sijtsma, “Executive summary Acoustic array corrections for coherence loss due to the wind tunnel shear layer,” in *Berlin Beamforming Conference (BeBeC)*, Berlin, 2008, ISBN: 978-3-00-023849-9.

[74] D. Ernst, C. Spehr, and T. Berkkefeld, “Decorrelation of acoustic wave propagation through the shear layer in open jet wind tunnel,” in *AIAA Aviation Forum*, Dallas, Texas, USA: American Institute of Aeronautics and Astronautics, 2015, ISBN: 9783937655239. DOI: `10.1081/E-EEE2-120046011`.

[75] C. J. Bahr, “Accounting for the Influence of Decorrelation in Microphone Phased Array Deconvolution Methods,” pp. 1–19, 2022. DOI: `10.2514/6.2022-2814`.

[76] P. Castellini and M. Martarelli, “Acoustic beamforming: Analysis of uncertainty and metrological performances,” *Mechanical Systems and Signal Processing*, vol. 22, no. 3, pp. 672–692, 2008, ISSN: 08883270. DOI: `10.1016/j.ymssp.2007.09.017`.

[77] T. Yardibi, C. Bahr, N. Zawodny, F. Liu, L. N. Cattafesta, and J. Li, “Uncertainty analysis of the standard delay-and-sum beamformer and array calibration,” *Journal of Sound and Vibration*, vol. 329, no. 13, pp. 2654–2682, 2010, ISSN: 0022460X. DOI: `10.1016/j.jsv.2010.01.014`.

[78] C. J. Bahr *et al.*, “A comparison of microphone phased array methods applied to the study of airframe noise in wind tunnel testing,” in *23rd AIAA/CEAS Aeroacoustics Conference*, 2017, ISBN: 9781624105043. DOI: `10.2514/6.2017-3718`.

[79] E. Sarradj *et al.*, “A microphone array method benchmarking exercise using synthesized input data,” in *23rd AIAA/CEAS Aeroacoustics Conference*, 2017, ISBN: 9781624105043. DOI: `10.2514/6.2017-3719`.

[80] C. J. Bahr *et al.*, “Shear Layer Correction Validation using a Non-Intrusive Acoustic Point Source,” in *16th AIAA/CEAS Aeroacoustics Conference*, American Institute of Aeronautics and Astronautics, 2010.

[81] S. Luesutthiviboon, L. Tercio, L. Pereira, D. Ragni, F. Avallone, and M. Snellen, “Aeroacoustic Benchmarking of Trailing-edge Noise from a NACA 63 3 – 018 Airfoil in a Broad Reynolds Number Range,” no. m,

[82] R. Merino-Martínez *et al.*, “Assessment of the accuracy of microphone array methods for aeroacoustic measurements,” *Journal of Sound and Vibration*, vol. 470, p. 115 176, 2020, ISSN: 0022-460X. DOI: `10.1016/j.jsv.2020.115176`. [Online]. Available: `https://doi.org/10.1016/j.jsv.2020.115176`.

[83] W. A. Timmer, “An overview of NACA 6-digit airfoil series characteristics with reference to airfoils for large wind turbine blades,” *47th AIAA Aerospace Sciences Meeting including the New Horizons Forum and Aerospace Exposition*, no. April, 2009. DOI: `10.2514/6.2009-268`.

[84] W. A. Timmer and R. P. J. O. M. V. Rooij, “Summary of the Delft University Wind Turbine Dedicated Airfoils,” in *41st AIAA Aerospace Sciences Meeting and Exhibit*, American Institute of Aeronautics and Astronautics, 2003. DOI: `10.2514/6.2003-352`.

[85] Hermann Schlichting, *Boundary layer theory*, 9th editio. Berlin: Springer, 2017, ISBN: 9783662529171.

[86] G. M. Corcos, “Resolution of Pressure in Turbulence,” *The Journal of the Acoustical Society of America*, vol. 35, no. 2, pp. 192–199, 1963, ISSN: 0001-4966. DOI: `10.1121/1.1918431`.

[87] G. M. Corcos, “The structure of the turbulent pressure field in boundary-layer flows,” *Journal of Fluid Mechanics*, vol. 18, no. 3, pp. 353–378, 1964, ISSN: 14697645. DOI: `10.1017/S002211206400026X`.

[88] F. H. Clauser, “The Turbulent Boundary Layer,” *Advances in Applied Mechanics*, vol. 4, no. C, pp. 1–51, 1956, ISSN: 00652156. DOI: `10.1016/S0065-2156(08)70370-3`.

[89] R. Vinuesa, A. Bobke, R. Örlü, and P. Schlatter, “On determining characteristic length scales in pressure-gradient turbulent boundary layers,” *Physics of Fluids*, vol. 28, no. 5, 2016, ISSN: 10897666. DOI: `10.1063/1.4947532`.

[90] M. Drela, “XFOIL: An Analysis and Design System for Low Reynolds Number Airfoils,” in *Low Reynolds Number Aerodynamics*, T. J. Mueller, Ed., Berlin, Heidelberg: Lecture Notes in Engineering, Springer, 1989, pp. 1–12, ISBN: 978-3-642-84010-4. DOI: `10.1007/978-3-642-84010-4`.

[91] R. W. Paterson, P. G. Vogt, M. R. Finkt, and C. L. Munch, “Vortex Noise of Isolated Airfoils,” *Journal of Aircraft*, vol. 10, pp. 296–302, 1972.

[92] C. Bak, *Aerodynamic design of wind turbine rotors.* Woodhead Publishing Limited, 2013, vol. 1, pp. 59–108, ISBN: 9780857094261. DOI: `10.1533/9780857097286.1.59`.

[93] S. B. Pope, *Turbulent Flows.* Cambridge, UK: Cambridge University Press, 2000, p. 771, ISBN: 9780521598866.

[94] R. C. Smith, *Uncertainty Quantification: Theory, Implementation, and Applications*, D. C. S. U. Estep, Ed. Raleigh, Noth Carolina: Society for Industrial and Applied Mathematics, 2014, p. 401.

[95] H. W. Coleman and W. Gleen Steele, *Experimentation, Validation, and Uncertainty Analysis for Engineers*, 4th. Hoboken, NJ, USA: Wiley, 2018, ISBN: 9781119417668.